TARGETED FULL-WAVEFORM INVERSION FOR RECOVERING THIN- AND ULTRA-THIN-LAYER PROPERTIES USING RADAR AND SEISMIC REFLECTION METHODS

by

Esther Babcock

A dissertation

submitted in partial fulfillment

of the requirements for the degree of

Doctor of Philosophy in Geophysics

Boise State University

May 2014

BOISE STATE UNIVERSITY GRADUATE COLLEGE

DEFENSE COMMITTEE AND FINAL READING APPROVALS

of the dissertation submitted by

Esther Babcock

Dissertation Title: Targeted Full-Waveform Inversion for Recovering Thin- and Ultra-Thin-Layer Properties Using Radar and Seismic Reflection Methods

Date of Final Oral Examination: 15 April 2014

The following individuals read and discussed the dissertation submitted by student Esther Babcock, and they evaluated her presentation and response to questions during the final oral examination. They found that the student passed the final oral examination.

John Bradford, Ph.D.	Chair, Supervisory Committee
John C. Freemuth, Ph.D.	Member, Supervisory Committee
Hans-Peter Marshall, Ph.D.	Member, Supervisory Committee
Alejandro N. Flores, Ph.D.	Member, Supervisory Committee
John R. Pelton, Ph.D.	Member, Supervisory Committee

The final reading approval of the thesis was granted by John Bradford, Ph.D., Chair of the Supervisory Committee. The thesis was approved for the Graduate College by John R. Pelton, Ph.D., Dean of the Graduate College.

ACKNOWLEDGEMENTS

I would like to acknowledge funding support provided by the Boise State University Department of Geosciences; the Society of Exploration Geophysicists (SEG) Foundation Scholarship; the ExxonMobil Geosciences Grant; the SIPES Foundation; and the Boise State University Student Research Initiative. Additional travel funding was provided by the SEG Travel Grants and Alaska Clean Seas. Finally, thanks to Alaska Clean Seas for access to their data.

ABSTRACT

Ground penetrating radar (GPR) and seismic reflection methods are useful geophysical tools for near-surface characterization. Analysis of radar or seismic reflection data can combine velocity analysis with common physical transformations to provide subsurface physical properties such as subsurface porosity, density, and contaminant locations. However, reliable quantitative characterization of thin subsurface layers may be impossible using standard reflection data processing techniques, e.g. velocity analysis, if the layer thickness is below the conventional resolution limits of the data. The limiting layer thickness for layer resolution may be up to ½ or even ¾ of the dominant wavelength (λ) of the signal in the medium of interest. This limitation often depends on data noise levels and source characteristics. In many environmental problems, target layers may be below this layer thickness and accurate determination of layer properties becomes problematic. In order to reliably quantify thin-layer parameters in these cases, geophysical practitioners require additional tools such as attribute analyses and inversion methodologies. Full-waveform inversions may be able to quantify layer parameters even in the case of thin ($< \frac{1}{2}\lambda$) and ultra-thin ($< \frac{1}{8}\lambda$) layers by inverting directly for thin-layer properties. Therefore, I provide a targeted full-waveform inversion algorithm to quantify thin- and ultra-thin layer parameters for multiple relevant environmental problems including oil in and under sea ice and basal conditions of glaciers. I demonstrate the efficacy of this approach on model and field data collected using radar and seismic reflection methods. These methods depend on surface records of

reflection information from subsurface interfaces and may fail if reflections are obscured or attenuated in the subsurface. Therefore, I demonstrate that a new dual-polarization system can mitigate the effects of the overburden anisotropy and conductivity attenuation on radar data collected in Arctic conditions. Combining my full-waveform inversion algorithm with improved sea ice radar data collection may enhance reliable quantification of spilled oil in the event of an accidental release in Arctic environments.

TABLE OF CONTENTS

ACKNOWLEDGEMENTS iv

ABSTRACT v

LIST OF TABLES xii

LIST OF FIGURES xiv

LIST OF ABBREVIATIONS xxi

CHAPTER ONE: INTRODUCTION 1

Overview 1

Radar Methods for Environmental Problems 2

Maxwell's Equations 3

The Wave Equation 8

Reflectivity 15

Seismic Considerations 21

Examples and Thin-Layer Problems 26

Introduction to Attribute Analysis for Thin Layers 32

Inversion Methods 37

Overview of Research 40

CHAPTER TWO: TARGETED FULL-WAVEFORM INVERSION OF GROUND-PENETRATING RADAR REFLECTION DATA FOR THIN AND ULTRA-THIN LAYERS OF NON-AQUEOUS PHASE LIQUID CONTAMINANTS PART I: ALGORITHM AND SYNTHETIC MODELING 44

Abstract 44

Introduction 45

Methodology 53

Forward Model 53

Petrophysics 54

Algorithm 56

Inversion 57

Testing 59

Models 60

Inversion Results 62

Source Inversion 62

Model 1 63

Model 2 64

Model 3 64

Parameter Sensitivity Testing 68

Conclusions 70

CHAPTER THREE: TARGETED FULL-WAVEFORM INVERSION OF GROUND-PENETRATING RADAR REFLECTION DATA FOR THIN AND ULTRA-THIN LAYERS OF NON-AQUEOUS PHASE LIQUID CONTAMINANTS PART 2: DATA TESTING 73

Abstract 73

Introduction 74

Methodology 76

Inversion 76

Testing 78

Examples 78

Example 1 79

Example 2 79

Example 3 84

Example 4 85

Inversion Results 88

Source Wavelet Inversion 88

Example 1 88

Example 2 89

Example 3 90

Example 4 91

Discussion 95

Conclusions 98

CHAPTER FOUR: QUANTIFYING THE BASAL CONDITIONS OF A MOUNTAIN GLACIER USING A TARGETED FULL-WAVEFORM INVERSION: BENCH GLACIER, ALASKA 99

Abstract 99

Introduction 100

Materials and Methods 105

Forward Model 105

Seismic Considerations 106

Inversion 107

Field Site 108

Data Collection 110

Data Processing 112

Testing 113
Source Recovery 114
Source Results 115
Synthetic Testing 116
Models 116
Parameter Sensitivity Testing: Sediment Layer Thickness 117
Synthetic Results 117
Model 1 117
Models 2, 3 and 4 118
Parameter Sensitivity Testing 119
Summary of Model Results 119
Data Testing 123
Data Results 124
Discussion 128
Conclusions 131
CHAPTER FIVE: ELECTRICAL ANISOTROPY IN SEA ICE AND A DUAL-POLARIZATION RADAR SYSTEM TO MITIGATE THE EFFECTS OF PREFERENTIAL ATTENUATION IN IMAGING SEA ICE 132
Abstract 132
Introduction 132
Sea Ice Electrical Anisotropy 135
Data Example: Testing at CRREL 139
Materials and Methods 139
Site 139

Acquisition 140

Results 140

Dual-Polarization Confirmation 142

CONCLUSIONS 149

REFERENCES 154

APPENDIX A 164

Linking Science to Public Policy for Land and Resource Management: A University Case Study 164

APPENDIX REFERENCES 207

LIST OF TABLES

Table 1.1: Relevant subsurface material properties of interest. For simplicity, I list effective conductivity ($\boldsymbol{\sigma ef}$)* and relative permittivity where $\boldsymbol{\varepsilon material\varepsilon 0 = \varepsilon r}$. Velocity is approximate. See Chapter 2 for additional discussion. 15

Table 1.2: Representative seismic material properties (Burger et al., 2006; Press, 1966). All properties depend on pressure and temperature. 26

Table 2.1 Representative electrical properties for the NAPL contaminated sites (Bradford et al., 2010; Annan, 2005; Hinz, 2012); values for water- and DNAPL-saturated sand calculated using the complex refractive index method (CRIM) for relative permittivity (ε_r) and Archie's law for σ using m=1.3 and n=1.4 (Knight and Endres, 2005). 49

Table 2.2: Model parameters: Model 1 simulates an oil layer overlying sea water; Model 2 represents a DNAPL trapped at a saturated sand/clay interface; and Model 3 describes an overland flow model with a saturated sand layer underneath a dry sand overlying bedrock. We estimated or calculated parameters as described in the text; d is also given as $\%\lambda$. Note that we generated Model 1 for 2 layer thicknesses. 62

Table 2.3: Inversion solution and standard deviation for source wavelet parameters using reflection from Layer 1/Layer 3 in an uncontaminated area for models; true η = 0 for all model source functions. 63

Table 2.4: Ultra-thin-layer parameters for a) Model 1, b) Model 2, and c) Model 3 and the inversion mean calculated from all results for ϕ_{GM}. Uncertainties for ε_r , d pairs are in Figure 2.3. 67

Table 3.1: Physical and electrical properties for laboratory and field data examples. 81

Table 3.2: Inversion solution and standard deviation for source wavelet parameters using reflection from Layer 1/Layer 3 in an uncontaminated area; in Examples 2 we simultaneously inverted for additional dense-sand thin layer parameters, and in Example 4 for thin snow layer parameters; those results are in Table 3.3. Figure 3.5 shows an example of solution uncertainties for f_0, δ_0 and f_0, η pairs. 89

Table 3.3: Ultra-thin-layer parameters for a) Example 1, b) Example 2, c) Example 3, d) Example 4a, and e) Example 4b with the inversion results corresponding to ϕ_{GM}. Uncertainties for ε_r, d pairs are shown graphically in Figures 3.1- 3.7. 94

Table 4.1: Representative material properties in the glacier system (Booth et al., 2013; Bradford et al., 2009; Fowler, 1990; Gusmeroli et al., 2010; Johansen et al., 2003; McGinnis et al., 1973; Mikesell et al., 2013; Nolan and Echelmeyer, 1999; Press, 1966; Smith, 2007). We distinguish basal ice from bulk glacier ice as ice carrying stratified or dispersed debris from the glacier bed with distinct physical, chemical, and mechanical properties (Knight, 1997). 105

Table 4.2: Model parameters: Model 1 simulates a hard bed; Model 2 simulates a thin layer of basal till; Model 3 simulates water at the bed of the glacier; Model 4 simulates a basal ice layer. Layers 1 and 3 are the same for all models. Note that d is also given as $\%\lambda$. 117

Table 4.3: Thin layer parameters for model testing and the inversion mean for Layer 2 parameters calculated from all results for ϕ_{GM}. Uncertainties reported for Q and d are estimated from α, Q and α, d pairs respectively, with the exception of Model 1 as noted in the text. 120

Table 4.4: Results for parameter sensitivity testing for 6 models with increasing d_{sed}; the coefficient of variation (cv), which is the standard deviation divided by the mean, describes the relative uncertainties. Uncertainty associated with smallest value for d_{sed} is over 25 times greater than for the thickest layer tested. These results demonstrate the robustness of the inversion but also the caution needed in interpreting very thin layer results. 123

Table 4.5: Solution range and total mean solution with estimated uncertainty and inversion bounds for 25 supergather traces. Solution range is given without high and low outliers as discussed in text; values for those outliers are in parentheses. 126

Table A.1: Selection of responses concerning incorporation of science into decision making which address the uncertainty in the decision making process.. 195

Table A.2: Number of items mentioned per person for "other sources of information that decision makers should consider," rounded to nearest whole number; note the policy faculty median and standard deviation (S). 196

Table A.3: Barriers listed by faculty in the ERB to interactions; note that respondents could list any number of items. 199

LIST OF FIGURES

Figure 1.1: Diagram showing incident, transmitted, and reflected plane waves (denoted by arrows) at a subsurface interface marked by contrast in material electric properties. 21

Figure 1.2: a) Schematic demonstrating P- and S-wave reflections and transmissions if $v_1 < v_2$; compare to Figure 1.1. b) P-wave reflection coefficients (*Q(1,1)*, equation 1.64) versus angle of incidence (θ_i) for three different models: glacier ice (v_p = 3690 m s^{-1}, ρ = 917 kg m^{-3}) overlying bedrock (v_p= 5400 m s^{-1}, ρ = 2700 kg m^{-3}) (solid line); glacier ice overlying till (v_p= 2000 m s^{-1}, ρ = 1900 kg m^{-3}) (dash-dot line); and glacier ice overlying water (v_p= 1500 m s^{-1}, ρ = 1000 kg m^{-3}) (dashed line) with R_p calculated using the full form of the Zoeppritz equations and material properties given in Table 1.2 (following Booth et al., 2013). Note that these reflection coefficients are only accurate for a reflection from 2 homogeneous, isotropic, welded half spaces, which does not accurately account for the presence of a thin layer. 30

Figure 1.3: Wavelets for reflection event from a representative 3-layer system where the second layer (L2) has thickness ranging from λ/10 to λ. Note that where L2= λ (right-most trace), two reflection events are clearly present, from the top and bottom of L2 (arrows). However, below L2=3λ/4, the upper and lower reflections become convolved with one another, making clear identification impossible. (Annan, 2005; Widess, 1973). 31

Figure 1.4: Modeled changes in reflection characteristics for a) L2=0.2λ and b)L2=0.1λ where L2 is the thin-layer thickness in a 3 layer model. Reflectivity response is from a 1D radar reflectivity model that I will describe in Chapter 2. Layer properties simulate a saturated sand (ε_r =22) / saturated clay(ε_r =35) system with a thin layer of a common environmental contaminamt (ε_r =7) present at the sand/clay interface. Relative changes in reflection phase and amplitude (note scale) are obvious in the thin-layer response of this model. For example, compare the leading edges of the two reflection events (arrows). 33

Figure 1.5: Laboratory data demonstrating changes in reflection characteristics using 1 GHz pulsed GPR data collected over a tank filled with saturated sand overlying saturated clay (for more details on data collection and processing see Chapter 3). The sand/clay boundary is approximately at 40 cm, and the sand/clay reflection event is clearly visible in both cases

(arrows); Wavelets are color coded with respect to amplitude; i.e. a red/blue/red event corresponds to a wave trough/peak/trough. The depression located at CDP 40-60 contained no thin layer in a) but a 0.005 m layer (3%λ) of a simulated contaminated in b). Note the relative change in reflection strength (28% increase) and characteristics in the presence of the thin layer. 35

Figure 1.6: Synthetic data from a 2D model with a source frequency of 450 MHz and a model space simulating the laboratory conditions in Figure 1.5. Black arrow annotates the sand/clay reflection event; red arrow points to region of increased reflection strength where the simulated thin layer is present. Although the layer thickness in part b) is twice that in Figure 1.5b, numerical analysis reveals that the reflection strength increase for the same layer thickness (not shown) from Figure 1.5a) to Figure 1.5b) is 51% while for the model case shown is 54%. The similarity between the model and data result is remarkable especially considering the thinness of the layer (only 6%λ)..... 36

Figure 1.7: The modeled reflectivity response of the 3-layer system given in Figure 1.4 using the same 1D reflectivity model (to be described in Chapter 2). I give Layer 2 (L2) thickness as %λ; L1 = L2 is the case where no thin layer is present. Note that both the zero-offset reflection coefficient and the slope of the AVA curve may change with increasing layer thickness. Quantifying this change and comparing to the AVA response in a field data set may allow interpreters to detect thin layers and estimate thin-layer properties (following Bradford and Deeds, 2006). 37

Figure 1.8: Schematic illustrating the difference between forward methods (e.g., reflection methods) and inversion..... 38

Figure 2.1: 1D reflectivity model and attribute results computed for 50 different cases of DNAPL layer thickness. a) Model with saturated sand (L1, ε_r = 29.1, brown) overlying clay (L3, ε_r = 35, white) and increasing DNAPL-saturated sand (L2, ε_r = 10.5, yellow) layer thickness from left to right; b) results from 1D reflectivity model; and extracted c) reflection strength, d) instantaneous frequency, and e) instantaneous phase. Full-waveform inversion can incorporate all of this information and best constrain the solution for thin-layer properties. 51

Figure 2.2: a) Paired f_0, δ_0 uncertainties and b) paired f_0, η uncertainties for the solutions from the source parameter inversion for Model 2; darker indicates lower values. The + is the true model value and the line encloses all paired values where the objective function is within 5% of ϕ_{GM}, which is the level of added Gaussian noise in the models. Although we only include the plots for the inversion solution for Model 2, the results from Models 1 and 3 are similar and are enumerated in Table 2.3. 63

Figure 2.3: Uncertainties calculated for ε_r, d pairs centered around the inversion solution for a) Model 1a, b) Model 1b, c) Model 2, and d) Model 3; blue colors are low. The + is the exact model value, the triangle is the inversion solution, and the line encloses all paired values where the objective function is within 5% of ϕ_{GM}. Uncertainties in solutions for σ and l are the range of values enclosed by the line for these parameters for coupled ε_r, σ pairs and ε_r, l pairs respectively (not pictured here, values in Table 2.4).65

Figure 2.4: Comparison of the difference between ϕ_{GM} (+) and ϕ_{LM} (.) from the 1000 inversion iterations for a) Model 1a and b) Model 2. For Model 2, $\phi_{GM} \cong 25\% \phi_{LMnearest}$, while for Model 1a, $\phi_{GM} \cong 96\% \phi_{LMnearest}$. A larger difference between the two may indicate a more reliable solution..... 66

Figure 2.5: Sensitivity testing for a) σ using Model 3 and b) d using Model 2, where · is the inversion solution, and the dashed line marks 1:1 correlation. Note scales. Error bars are those solutions within 5% of ϕ_{GM}. The inversion does not appear to be sensitivity to σ, which corroborates our observations throughout model testing. On the other hand, the inversion retrieves layer thicknesses accurately (within 5% of the true model value) down to a layer thickness of 0.4%λ. 70

Figure 3.1: Example 1 showing a) Diagram of setup for data collection; b) Data (solid line) from the air/salt water reflection and the inversion results (dashed line) from the source wavelet inversion; c) Data (solid) from the air/oil/water reflection and inversion results (dashed). Vertical dotted lines indicate the data window used for the targeted inversion algorithm. d) plot showing coupled uncertainties between ε_{oil} and d_{oil}; + is solution corresponding to ϕ_{GM}, triangle is measured values, and the line encloses all paired values where the objective function is within 10% of ϕ_{GM}. Darker shading indicates lower values of the objective function. 80

Figure 3.2: Laboratory setup for saturated-sand/DNAPL-saturated sand/clay system, where a) shows Layer 3, the sodium bentonite clay, with the depression to contain the injected DNAPL, and b) shows an example of antenna positioning for multi-offset data collection after filling the remaining tank space in the tank with saturated sand. c) The processed, time-migrated stacked data with top mute applied; topographic depression is located approximately between CDP 40 and 60 (box). Solid arrow points to first arrival of the sand/dense sand/clay reflection event; the reflection arrives earlier in time at the center of the tank (CDP 50), corroborating our result for a thicker dense sand layer over the topographic depression. Dashed arrow points to the first arrival of the sand/dense sand/DNAPL sand/clay reflection event over the center of the depression. 83

Figure 3.3: a) Data from Wurthsmith field site; contaminated region is marked by increased attenuation below the water table. Leftmost arrow is

approximate position of traces for source parameters inversion; rightmost arrow is approximate position of traces for thin-layer inversion. b) Data (solid line) from the uncontaminated water table reflection and the inversion results (dashed line) from the source wavelet inversion; c) Data (solid) from the LNAPL region and inversion results (dashed). Vertical dotted l;ines indicated target window. d) Coupled uncertainties between ε_{napl} and d_{napl}; + is solution corresponding to ϕ_{GM}, triangle is measured values, and the line encloses all paired values where the objective function is within 10% of ϕ_{GM}. Darker shading indicates lower values of the objective function..... 85

Figure 3.4: a) Helicopter flight path over the uncontaminated (control) cell and the oily cell for Example 3; b) example data collected along flight path over clean test cell demonstrating variable snow thickness, and c) oily cell (Bradford et al., 2010)..... 87

Figure 3.5: Paired f_0, δ_0 (a) and f_0, η (b) and uncertainties for the solutions from the source parameter inversion for Example 1. The + marks the inversion solution and the line encloses all paired values where the objective function is within 10% of ϕ_{GM}. Darker shades are smaller values of the objective function. Results for other tests are in Table 3.2..... 89

Figure 3.6: a) Trace (solid line) located at CDP 20 with inversion solution for source parameters (dashed line); vertical dotted lines indicate target window used in inversion algorithm; arrow points to the same location as the leftmost arrow in Figure 3.2c. Note the high amount of noise present in the data. b) Plot showing coupled uncertainties for ε_{sand2}, d_{sand2} from the source inversion; + is solution corresponding to ϕ_{GM} and the line encloses all paired values where the objective function is within 10% of ϕ_{GM}; darker shading indicates lower values of the objective function. The true values for ε_{sand2}, d_{sand2} are unknown. c) Solution (solid) vs data (dashed) for DNAPL parameters using trace at CDP 50; the arrow corresponds to the rightmost arrow in Figure 3.2c. The presence of multiple reflection events causes uncertainty in defining the target window. d) Plot showing coupled uncertainties between ε_{napl} and d_{napl}; triangle indicates measured values (other notation the same as part b)..... 91

Figure 3.7: Data (solid) and inversion results (dashed) for Example 3. Labels indicate reflection events and vertical dotted lines show the data window used for the targeted inversion algorithm. a) uncontaminated snow over ice with $d_{snow} \cong 0.11$ m (46%λ); b) uncontaminated snow over ice with $d_{snow} \cong 0.07$ m (25%λ) ; c) Plot showing coupled uncertainties between ε_{snow} and d_{snow} for b); + is solution corresponding to ϕ_{GM}, triangle marks the estimated values, and the line encloses all paired values where the objective function is within 10% of ϕ_{GM}. d) data (solid) and inversion results (dashed) for an ultra-thin oil layer (0.02 m, 9%λ) underneath an

thin snow layer (0.04 m, 16%λ). e) Plot showing coupled uncertainties between ε_{oil} and d_{oil}; notation same as part c). 93

Figure 3.8: Inversion results (dashed) plotted vs data (solid) to demonstrate the effect of changes in user-defined reflection window on solution accuracy; dashed lines show the data window used for the targeted inversion algorithm. a) Solution corresponding to data windowed between 29.0 and 31.5 ns; b) Solution when using a longer reflection window (28.5 - 31.5 ns). The solution shown in b) returns anomalously high values for ε_{oil} (>6)..... 97

Figure 4.1: a) Bench Glacier, Alaska showing location of 3D seismic survey (white box) and surface seismic monitoring station locations (+) where Mikesell et al. (2012) report surface ice velocities and *Q* values; 20 m contour lines show bed elevation. Black line intersecting 3D survey area is location of 2D seismic profile shown in Figure 4.2c. b) 3D survey map with grey-scale fold density (lighter shade indicates higher fold) showing trace locations for inversion within the box in area of highest fold; x and y directions marked on plot correspond to those in Figures 4.5 and 4.6 with x_0,y_0 at lower left corner of inversion box. * indicates source locations and arrows point to white boxes enclosing receiver locations. 111

Figure 4.2: Data from Bench Glacier, Alaska: a) and b) show 2 representative supergathers with binned offsets as discussed in text. For viewing purposes these data have automatic gain applied with a 50 ms sliding window. c) Time-migrated 2D seismic profile across the survey area (solid line in Figure 4.2a and b). Note change in reflection characteristics across the length of the bed: arrows on left point to the peaks of two reflection events that converge across the glacier to the point marked by third arrow. At ice velocity, the maximum peak-to-peak distance closest to our survey is 8 m, or about 55%λ. Black line underscores region of seismic profile corresponding to inversion traces. 112

Figure 4.3: a) Seismic record for stacked traces binned between 55 and 75 m offset; straight solid line underscores direct arrivals and arrow points to Rayleigh waves; b) extracted source wavelet spectrum. 116

Figure 4.4: Results for parameter sensitivity testing with Model 2: a) shows the 6 models with increasing layer thickness from left to right. Dashed line is model with 5% added Gaussian noise, and thin solid line indicates inversion solution. All traces are normalized by the maximum source amplitude. b) Inversion solution for d_{sed} versus true model *d* and estimated solution uncertainties. Uncertainties for lower layer thicknesses are 25 times greater than the uncertainty associated with thickest layer which is not evident in plot (see Table 4.4). 122

Figure 4.5: 5 representative supergather traces (solid line) and the inversion solution (dashed line) taken from approximately y = 4 m and x positions across the lower portion of the inversion box shown in Figure 4.1b. Horizontal solid lines define the target window for each trace and all traces are normalized by the maximum source amplitude. Target window choice depends on user discretion and is an essential consideration in the inversion process. 125

Figure 4.6: Solutions for 25 supergathers for a) layer d (m); b) α (m s^{-1}); c) ρ (kg m^3); and d) overburden Q (Q_{ice}); note scales for each plot, where x,y positions are relative to inversion box shown in Figure 4.2 starting at lower left corner. Mean estimated uncertainties are not shown but reported in Table 4.5. Each box represents the inversion solution for the appropriate variable from one stacked supergather as described in text..... 127

Figure 4.7: Demonstration of paired parameter solution uncertainty plots for 1 reference inversion solution for a) α (m s^{-1}) vs ρ (kg m^3); b) α vs Q_{ice}; and c) α vs d (m). Darker colors correspond to lower uncertainties and scale is relative to each parameter pair. White line encloses solutions from the parameter pair with RMS $\leq$ 5%, and triangle marks the inversion solution. In general other uncertainty plots show similar characteristics. Here α, Q_{ice} pairs (c) demonstrates the possibilities of multiple local minima with the concurrent difficulties such a situation poses for ill-constrained FWI problems..... 127

Figure 5.1: Sea ice crystals in columnar ice having a) oriented brine pockets with varying shape and size within randomly-oriented columnar ice crystal matrix and b) possible orientation of the columnar ice matrix in response to dominant currents (following Kovacs et al., 1987). 135

Figure 5.2: Demonstration of the modeled and real effects of sea ice anisotropy on radar data using 500 MHz central frequency, n=0.07, and parallel (solid) or perpendicular (dashed) polarizations: a) effective conductivity versus temperature; $\boldsymbol{\sigma si}$ ∥ is more than 2 times $\boldsymbol{\sigma si}$ ⊥ at all ice temperatures above -17 °C. b) calculated attenuation exponent α for each polarization; for sea ice at -2° C, $\boldsymbol{\alpha si}$ ∥is more than 2 times greater than $\boldsymbol{\alpha si}$ ⊥. c) 1D reflectivity model of ice bottom reflection with ice thickness 0.85 m (reflection at 12 ns). The left plot uses Archie's law exponent m=1.75 for antenna polarization perpendicular to primary crystal orientation; plot on right uses m=1.5 for parallel polarization; in this case reflection strength from ice/oil/water interface is reduced by a factor of 85. d) 1 GHz pulsed radar data collected at CRREL in both polarizations. The almost-complete disappearance of the ice/oil interface and the ice-water interface in the cross-tank direction (rectangle) is likely a result of attenuation due to conductivity anisotropy..... 141

Figure 5.3: Dual-polarization system: 500 MHz antenna-receiver pairs oriented parallel and perpendicular to survey direction, as shown by orientation of odometer wheel travel. 143

Figure 5.4: Data collected over sea ice at Prudhoe Bay, Alaska using the dual-polarization system: a) in line with survey direction, b) perpendicular to survey direction, and c) vector sum of a) and b). The combined information from both polarizations provides the most complete image of the sea ice/ water interface. d) Solid arrows denote relative direction and relative strength of anisotropy with respect to the survey direction (dashed arrow) and relative to the unit circle. Two equally valid solutions exist (±180°). 146

Figure 5.5: Radar data collect over a saline ice sheet at CRREL at 0.1 m increments a) in line with survey direction, b) perpendicular to survey direction, and c) vector sum of a) and b); d) shows relative reflection strength across corresponding to a (dashed line), b (solid line), and c (bold line) with very high amplitudes corresponding to oil locations under the ice at about 4-5 m (traces 40-50) and 9-11 m (trace 90-110). 147

Figure A.1: The Environmental Research Building at Boise State University, Boise, Idaho 188

LIST OF ABBREVIATIONS

A	Ampere
C	Coulomb
H	Henry
F	Farad
kg	kilogram
m	meter
s	second
S	Siemen
T	Tesla
V	volt

CHAPTER ONE: INTRODUCTION

Overview

Seismic and radar reflection methods are a common and useful tool for near-surface geophysical investigation (e.g. Bradford et al., 2009; Dow et al., 2013; Kim et al., 2010; Zeng et al. , 2000). Surface-based use of either method requires introducing wave energy into the subsurface and recording the return signal at the surface. One major difference between the two methods is signal frequency. For example, seismic frequencies may range from 1 to 100 Hz while the radar range is generally between 10 MHz and 10 GHz. In addition, seismic waves and radar waves are sensitive to different subsurface properties: density (ρ, kg m^3), velocity (α, m s^{-1}), and seismic attenuation (Q) in the case of seismic methods but permittivity (ε, F m^{-1}) and conductivity (σ, S m^{-1}) in the case of radar waves (Aki and Richards, 2002). However, the basic underlying equations for analyzing wave travel and reflectivity response are similar for both techniques. The similarities between the two methods allow for effective application of multiple seismic data processing techniques to radar data (Bradford, 2007; Bradford and Wu, 2007).

My research focuses on using radar and seismic reflection data to quantify thin layers that may be present in the near-subsurface. I am especially interested in environmental problems such as contaminated site characterization and snow and ice research. Thus, I begin by discussing radar-based subsurface investigations and the

underlying wave equations for electromagnetic wave propagation. I subsequently summarize the appropriate analogs with respect to seismic reflection methods. Since "thin" subsurface layers often arise in environmental problems, I discuss the problems that arise with either method due to the presence of thin layers in the subsurface. Two relevant methods for overcoming those difficulties include amplitude variation with offset (AVO) analysis and full-waveform inversions (FWIs). My research has produced a targeted FWI algorithm that can use radar or seismic reflection data to quantify thin layers of near-surface material, including environmental contaminants. The subsequent chapters delineate my modeling and inversion methods, including testing on model and field or laboratory data collected both with radar and seismic reflection methods.

Radar Methods for Environmental Problems

Ground penetrating radar (GPR) is a near-surface geophysical tool well-suited for detecting subsurface contamination (Brewster and Annan, 1994; Bradford and Deeds, 2006; Bradford et al., 2010; Luciano et al., 2010; Orlando, 2002). Reflection GPR methods traditionally incorporate velocity analysis combined with common petrophysical transformations to indirectly estimate subsurface electrical and physical properties at a contaminated site (Annan, 2005). Zones of anomalous electrical properties may indicate the presence of contamination (Bradford and Deeds, 2006). Contaminants of interest relevant to my research are non-aqueous phase liquids (NAPLs). These contaminants are often harmful to human health (Brusseau et al., 2011).

GPR methods can provide a non-invasive, cost-effective, rapid methodology for site characterization. 2D or 3D radar reflection surveys can delineate zones of contamination with greater site coverage than borehole monitoring (Bradford and Deeds,

2006). Accurately delineating zones of subsurface contamination allows prioritization of remediation efforts. Of course, rigorous use of all geophysical data including radar and seismic data requires confirmation with boreholes or other lower resolution point-sampling methods (Hinz, 2012). These methods can provide detailed vertical characterization but only at specific point locations. Said another way, point measurements lack horizontal resolution. Thus when correctly verified with point measurements, GPR data may provide improved spatial characterization. When integrated with control data and careful interpretation, GPR reflection surveys may offer site managers a robust tool for contaminant detection, monitoring, and remediation (Bradford and Babcock, 2013; Babcock and Bradford, 2013).

However, the robustness of GPR-aided contaminant detection and quantification may be compromised when contaminants migrate from their initial source location and disperse across a contaminated site. This dispersion may result in a thin contaminant layer. "Thin" is relative to the dominant wavelength (λ) of the signal in the material of interest. Although researchers have addressed thin-layer problems since the mid-1900s (Widess, 1973), accurately quantifying thin-layer parameters continues to be problematic for both seismic and radar exploration. Basic understanding of radar methods and subsequent detection and quantification of thin subsurface layers begins with the relevant electromagnetic (EM) theory as applicable to reflection GPR methods and the thin-bed problem.

Maxwell's Equations

Due to the breadth of his contributions to the study of electricity and magnetism, James Clerk Maxwell is known as the father of electromagnetics. Two of his outstanding

contributions to the field came via his extraordinary observation that light is electromagnetic (EM) radiation and through the addition of an important term to Ampere's law (Goldman, 1983). Maxwell's equations provide the basis for deriving the equation for electromagnetic (EM) wave propagation in subsurface materials (Griffiths, 1999). As a historical byline, it was Oliver Heaviside, rather than James Clerk Maxwell, who developed modern vector notation and composed Maxwell's equations in the modern formulation with which the reader is familiar (Goldman, 1983).

In any case, "Maxwell's" equations consist of Faraday's law, Ampere's law, Gauss's law, and the monopole law. Either differential or integral forms of the equations are equally valid. Maxwell's equations provide empirical descriptions of the behavior of electric and magnetic fields and their coupled nature. Here I present the differential form of Maxwell's equations in earth materials and include several relevant simplifying assumptions (Fleisch, 2008). Combining these equations in the presence of certain simplifying assumptions leads to the EM wave equation. The wave equation is the basis for understanding the physics of radar propagation and subsequent attempts to extracting meaningful physical information using data processing techniques and petrophysical relationships (Griffiths, 1999).

The curl of a vector field describes the circulation of that field around a point, while the divergence of a vector field is the amount of flux passing through an infinitesimally small surface enclosing some charge, per unit volume (Fleisch, 2008). One can conceptually think of that charge as acting a source (positive divergence) or sink (negative divergence) of the field. Faraday's law expresses the curl of the electric field, $\boldsymbol{E}$, as the time derivative of the magnetic field, $\boldsymbol{B}$:

$$\nabla \times \boldsymbol{E}(\boldsymbol{x},t) = -\frac{\partial \boldsymbol{B}(\boldsymbol{x},t)}{\partial t}. \quad (1.1)$$

The electric field is a vector force field describing the electrical force per unit charge acting on a charged particle. Therefore $\boldsymbol{E}$ has units V m^{-1}. Conversely $\boldsymbol{B}$ is also a vector field but describes the magnetic force per unit charge per unit velocity acting on a particle moving perpendicularly to the magnetic field direction. Units of $\boldsymbol{B}$ are Tesla (T).

Next I introduce two definitions that I will use in Ampere's law and Gauss's law. The first relates the electric field to electric displacement, $\boldsymbol{D}$ and the electric polarization, $\boldsymbol{P}$:

$$\boldsymbol{D}(\boldsymbol{x},t) \equiv \varepsilon_0 \boldsymbol{E}(\boldsymbol{x},t) + \boldsymbol{P}. \quad (1.2)$$

Electric polarization is the electric dipole moment per unit volume. The electric displacement and the electric polarization have units of C m^{-2}.

The second equation defines the magnetic field strength $\boldsymbol{H}$ in terms of $\boldsymbol{B}$ and the magnetic polarization, $\boldsymbol{M}$:

$$\boldsymbol{H}(\boldsymbol{x},t) \equiv \frac{1}{\mu_0}\boldsymbol{B}(\boldsymbol{x},t) - \boldsymbol{M}. \quad (1.3)$$

The magnetic field strength $\boldsymbol{H}$ has unit of A m^{-1}, as of course does $\boldsymbol{M}$. In free space, the magnetic permeability and the permittivity are constant: $\mu_0 \equiv 4\pi \times 10^{-7}$ H/m and $\varepsilon_0 \cong 8.58 \times 10^{-12}$ F/m. Permittivity is a measure of a material's ability to store charge in the presence of an applied electric field.

I use equations 1.2 and 1.3 in my statements of Ampere's law (equation 1.4) and Gauss's law (equation 1.5):

$$\nabla \times \boldsymbol{H}(\boldsymbol{x},t) = \boldsymbol{J}(\boldsymbol{x},t) + \frac{\partial \boldsymbol{D}(\boldsymbol{x},t)}{\partial t}. \quad (1.4)$$

$$\nabla \bullet \boldsymbol{D}(\boldsymbol{x}, t) = \rho. \quad (1.5)$$

where $\boldsymbol{J}$ is electric current density. Thus, Gauss's law states that the divergence of $\boldsymbol{D}$ is equal to the enclosed free charge density ρ.

Finally, the monopole law defines the divergence of $\boldsymbol{B}$ to be zero everywhere:

$$\nabla \bullet \boldsymbol{B}(\boldsymbol{x}, t) = 0 \quad (1.6)$$

Since the divergence is zero in all space, sources or sinks of $\boldsymbol{B}$ can never exist. Therefore, free magnetic charges cannot exist, and magnetic charges always exist in positive/negative pairs. To date, no one has ever observed a free magnetic charge.

In order to combine and transform Maxwell's equations to the wave equation for radar travel in earth materials, I first assume that $\boldsymbol{M}$ is zero. In that case, the magnetic permeability in the material of interest is always equal to μ_0. This approximation is valid in most near-surface material of interest to many GPR practitioners, such as sandy soils and aquifers. However, some rocks and ores, e.g. iron and steel, may have magnetic permeability one or two orders of magnitude higher than μ_0. In those cases, I could not make the approximation that $\mu = \mu_0$.

In a linear, homogeneous, and isotropic material $\boldsymbol{J}$ is proportional to $\boldsymbol{E}$:

$$\boldsymbol{J}(\boldsymbol{x}, t) = \sigma \boldsymbol{E}(\boldsymbol{x}, t). \quad (1.7)$$

Equation 1.7 is Ohm's law. Ohm's law expresses electric current density, $\boldsymbol{J}$, as a function of the electric field and the conductivity σ, of the material carrying that current. In contrast with ε, conductivity is a measure of a material's ability to transmit charge. It has units of S m^{-1}.

To simplify the expression for electric displacement in a linear dielectric, I start with equation 1.2 and recognize that $\boldsymbol{P}$ is proportional to $\boldsymbol{E}$ in such a material:

$$\boldsymbol{P}(\boldsymbol{x},t) = \varepsilon_0 \chi_e \boldsymbol{E}(\boldsymbol{x},t) \tag{1.8}$$

$$\boldsymbol{D}(\boldsymbol{x},t) = \varepsilon_0 \boldsymbol{E}(\boldsymbol{x},t) + \varepsilon_0 \chi_e \boldsymbol{E}(\boldsymbol{x},t) \tag{1.9}$$

and

$$\boldsymbol{D}(\boldsymbol{x},t) = \varepsilon_0 (1 + \chi_e) \boldsymbol{E}(\boldsymbol{x},t). \tag{1.10}$$

Then defining $\varepsilon = \varepsilon_0 (1 + \chi_e)$, I can write $\boldsymbol{D}$ in terms of $\boldsymbol{E}$:

$$\boldsymbol{D}(\boldsymbol{x},t) = \varepsilon \boldsymbol{E}(\boldsymbol{x},t) \tag{1.11}$$

where ε is the material's permittivity. Taking $\varepsilon_r = 1 + \chi_e$, it follows from examining equation 1.10 that ε is proportional to the permittivity of free space (Table 1.1):

$$\varepsilon = \varepsilon_r \varepsilon_0 \tag{1.12}$$

where ε_r is the relative permittivity.

Then, Ampere's and Faraday's law easily simplify as follows:

$$\nabla \times \boldsymbol{B}(\boldsymbol{x},t) = \mu_0 [\sigma \boldsymbol{E}(\boldsymbol{x},t) + \varepsilon \tfrac{\partial \boldsymbol{E}(\boldsymbol{x},t)}{\partial t}] \quad . \tag{1.13}$$

and

$$\nabla \times \boldsymbol{E}(\boldsymbol{x},t) = -\tfrac{\partial \boldsymbol{B}(\boldsymbol{x},t)}{\partial t}. \tag{1.14}$$

Since σ is multiplied with the vector field $\boldsymbol{E}$ to produce the vector field $\boldsymbol{J}$, σ is a tensor in anisotropic materials. Similarly, ε is also a tensor in anisotropic materials. However, if one assumes a homogeneous, isotropic earth material, ε and σ reduce to scalar quantities. Most earth materials are neither homogenous nor isotropic in nature.

Nevertheless, these simplifying assumptions promote comprehension of the derivation of the EM wave equation and its physical meaning. The assumptions often provide a good approximation of the bulk properties and behavior of many subsurface materials. Nonetheless, one must remain alert for situations where these assumptions fail and be prepared to apply a more rigorous treatment of the Maxwell's equations. One example I address in Chapter 5 is the anisotropic nature of the conductivity structure of sea ice.

The Wave Equation

That being said, with those simplifying assumptions and the previous assumption that $\mu = \mu_0$ for our materials of interest, I take the curl of both sides of Faraday's law (equation 1.11) and substitute Ampere's law for the curl of $\boldsymbol{B}$ with the following result:

$$\nabla \times \nabla \times \boldsymbol{E}(\boldsymbol{x}, t) = \nabla \times \left(-\frac{\partial \boldsymbol{B}(\boldsymbol{x},t)}{\partial t}\right) \tag{1.15}$$

A vector identity provides the mathematical key to break apart the left-hand side of the preceding equation (Fleisch, 2008):

$$\nabla \times \left(\nabla \times \boldsymbol{E}(\boldsymbol{x}, t)\right) = \nabla\left(\nabla \bullet \boldsymbol{E}(\boldsymbol{x}, t)\right) - \nabla^2 \boldsymbol{E}(\boldsymbol{x}, t). \tag{1.16}$$

I can combine Gauss's law given in equation 1.5 with equation 1.11 to analyze the term $\nabla \bullet \boldsymbol{E}(\boldsymbol{x}, t)$. If there is zero enclosed charge in a region, then $\nabla \bullet \boldsymbol{E}(\boldsymbol{x}, t) = 0$ in that region. By making this statement, I am assuming that there are no free charges present in the subsurface materials. Subsurface conditions may sometimes violate this assumption. Nonetheless, I proceed assuming $\nabla \bullet \boldsymbol{E}(\boldsymbol{x}, t) = 0$ in the case of zero enclosed charge and equation 1.15 reduces to the following form:

$$-\nabla^2 \boldsymbol{E}(\boldsymbol{x}, t) = \nabla \times \left(-\frac{\partial \boldsymbol{B}(\boldsymbol{x},t)}{\partial t}\right). \tag{1.17}$$

I assume that the spatial and temporal derivatives of $\boldsymbol{B}$ are independent and can thus manipulate equation 1.17 to the following form:

$$-\nabla^2 \boldsymbol{E}(\boldsymbol{x},t) = -\frac{\partial(\nabla\times\boldsymbol{B}(\boldsymbol{x},t))}{\partial \mathrm{t}}. \tag{1.18}$$

Substituting equation 1.13 into equation 1.18 provides the following result:

$$\nabla^2 \boldsymbol{E}(\boldsymbol{x},t) = \frac{\partial(\mu_0[\sigma \boldsymbol{E}(\boldsymbol{x},t)+\varepsilon\frac{\partial \boldsymbol{E}(\boldsymbol{x},t)}{\partial t}])}{\partial \mathrm{t}}. \tag{1.19}$$

Breaking apart the right hand side of equation 1.19 and grouping all terms on the left provides the familiar form of the wave equation (Griffiths, 1999):

$$\nabla^2 \boldsymbol{E}(\boldsymbol{x},t) - \mu_0\sigma\frac{\partial \boldsymbol{E}(\boldsymbol{x},t)}{\partial \mathrm{t}} - \mu_0\varepsilon\frac{\partial^2 \boldsymbol{E}(\boldsymbol{x},t)}{\partial \mathrm{t}^2} = 0. \tag{1.20}$$

Remember that with the previous assumptions I can treat μ_0, σ, and ε as constant and move them outside the time derivative. On the other hand, if a 2D medium is anisotropic, ε and σ become second-order tensors:

$$\widetilde{\varepsilon} = \begin{bmatrix} \varepsilon_{11} & \varepsilon_{21} \\ \varepsilon_{12} & \varepsilon_{22} \end{bmatrix} \tag{1.21}$$

and

$$\widetilde{\sigma} = \begin{bmatrix} \sigma_{11} & \sigma_{21} \\ \sigma_{12} & \sigma_{22} \end{bmatrix}. \tag{1.22}$$

If coupling between tensor components is negligible, σ_{21}, σ_{12}, ε_{21}, and ε_{12} are zero. I substitute the modified tensors into the wave equation:

$$\nabla^2 \boldsymbol{E}(\boldsymbol{x},t) - \mu_0\begin{bmatrix} \sigma_{11} & 0 \\ 0 & \sigma_{22} \end{bmatrix}\frac{\partial \boldsymbol{E}(\boldsymbol{x},t)}{\partial \mathrm{t}} - \mu_0\begin{bmatrix} \varepsilon_{11} & 0 \\ 0 & \varepsilon_{22} \end{bmatrix}\frac{\partial^2 \boldsymbol{E}(\boldsymbol{x},t)}{\partial \mathrm{t}^2} = 0. \tag{1.23}$$

By choosing an appropriate coordinate system, given my previous assumptions I can treat the problem as two separate cases with respect to the orientation of the anisotropy and the relative direction of propagation of $\boldsymbol{E}$, here denoted as $E_1$and E_2:

$$\nabla^2 E_1(\boldsymbol{x},t) - \mu_0\sigma_{11}\frac{\partial E_1(\boldsymbol{x},t)}{\partial \mathrm{t}} - \mu_0\varepsilon_{11}\frac{\partial^2 E_1(\boldsymbol{x},t)}{\partial \mathrm{t}^2} = 0 \tag{1.24}$$

and

$$\nabla^2 E_2(\boldsymbol{x},t) - \mu_0\sigma_{22}\frac{\partial E_2(\boldsymbol{x},t)}{\partial \mathrm{t}} - \mu_0\varepsilon_{22}\frac{\partial^2 E_2(\boldsymbol{x},t)}{\partial \mathrm{t}^2} = 0. \tag{1.25}$$

In Chapter 5, I start with a variation of these two equations and proceed to describe the anisotropic nature of EM wave propagation in sea ice.

Now I revisit equation 1.20 in the case of a homogeneous, isotropic, linear dielectric. Note that it has 3 terms. The first describes the second-order spatial derivative of $\boldsymbol{E}$. The second term is a diffusion term. The fact that this term is proportional to σ demonstrates that conductivity acts to attenuate the travel of a radar wave in the subsurface (Hohmann, 1988). The final term is a second-order time derivative. It is the wave propagation term. Since the propagation term is proportional to ε, velocity is inversely proportional to the square root of a material's ε:

$$v = \sqrt{\frac{1}{\mu_0\varepsilon}}. \tag{1.26}$$

Thus, if one can estimate the velocity of the radar wave, one can subsequently estimate a material's ε. Knowing ε, common petrophysical transformations provide means to transform its estimated value to physical material properties such as density (ρ) and porosity (ϕ) (Annan, 2005; Knight and Endres, 2005). I review several of these transformations in Chapter 2.

One can easily solve the wave equation. One common method is separation of variables. The result is the total plane-wave solution:

$$\boldsymbol{E}(\boldsymbol{x},t) = E_0 e^{i(\tilde{k}\boldsymbol{x}-\omega t)} \tag{1.27}$$

where the subscript *0* indicates the constant initial field defining the appropriate coordinate system I can define a wave traveling in the arbitrary x-direction using equation 1.27:

$$\boldsymbol{E}(x,t) = E_0 e^{i(\tilde{k}x-\omega t)}\hat{\jmath} \tag{1.28}$$

where $\hat{\jmath}$ is a unit vector in the y-direction.

One can also use Maxwell's equations to find the wave equations for *B* by starting with the curl of Ampere's law. I can also take the curl of equation 1.28 and apply Faraday's law as follows:

$$\nabla \times \boldsymbol{E}(x,t) = \nabla \times E_0 e^{i(\tilde{k}x-\omega t)}\,\hat{\jmath} \tag{1.29}$$

$$-\frac{\partial \boldsymbol{B}(x,t)}{\partial t} = -\frac{\partial B_0}{\partial t} e^{i(\tilde{k}x-\omega t)}\hat{k} \tag{1.30}$$

As Griffiths (1999) shows, the result is a wave equation for $\boldsymbol{B}$ traveling with $\boldsymbol{E}$ but oriented perpendicularly with respect to $\boldsymbol{E}$:

$$\boldsymbol{B}(x,t) = \frac{1}{v} E_0 e^{i(\tilde{k}x-\omega t)}\hat{k} \tag{1.31}$$

where $\hat{k}$ is a unit vector in the z-direction. Thus, the amplitude of $\boldsymbol{B}$ is proportional to that of $\boldsymbol{E}$ divided by the EM wave velocity:

$$B_0 = \frac{1}{v} E_0. \tag{1.32}$$

I will revisit equation 1.28 and 1.31 in the reflectivity section.

Going back to equation 1.27, I take the appropriate derivatives of $\boldsymbol{E}$ and substitute them back into the wave equation:

$$\frac{\partial^2 \boldsymbol{E}(\boldsymbol{x},t)}{\partial \mathrm{x}^2} = -E_0 \tilde{k}^2 e^{i(\tilde{k}\boldsymbol{x}-\omega t)} \tag{1.33}$$

$$\frac{\partial \boldsymbol{E}(\boldsymbol{x},t)}{\partial \mathrm{t}} = -E_0 i\omega e^{i(\tilde{k}\boldsymbol{x}-\omega t)} \tag{1.34}$$

$$\frac{\partial^2 \boldsymbol{E}(\boldsymbol{x},t)}{\partial \mathrm{t}^2} = -E_0 \omega^2 e^{i(\tilde{k}\boldsymbol{x}-\omega t)} \tag{1.35}$$

$$-E_0 \tilde{k}^2 e^{i(\tilde{k}\boldsymbol{x}-\omega t)} = -E_0 i\omega\mu_0\sigma e^{i(\tilde{k}\boldsymbol{x}-\omega t)} - E_0 \omega^2 \mu_0 \varepsilon e^{i(\tilde{k}\boldsymbol{x}-\omega t)}. \tag{1.36}$$

Regrouping yields the following form:

$$-E_0 \tilde{k}^2 e^{i(\tilde{k}\boldsymbol{x}-\omega t)} = -E_0 (i\omega\mu_0\sigma + \omega^2\mu_0\varepsilon) e^{i(\tilde{k}\boldsymbol{x}-\omega t)} = 0 \tag{1.37}$$

which reveals that the complex-valued wavenumber $\tilde{k}$ describes the propagation of the wave and is a function a σ and ε:

$$\tilde{k}^2 = i\omega\mu_0\sigma + \omega^2\mu_0\varepsilon. \tag{1.38}$$

The wavenumber demonstrates that the propagation of the wave, including attenuation and velocity, depends on the material properties. Table 1.1 gives some relevant subsurface electric properties and the corresponding EM wave velocities in the material following equation 1.26.

Next, I solve for $\tilde{k}$ and substitute the result into equation 1.27. First I take the square root of equation 1.38:

$$\tilde{k} = \sqrt{i\omega\mu_0\sigma + \omega^2\mu_0\varepsilon}. \tag{1.39}$$

Since $\omega\mu_0\sigma$ must be positive, the principal square root of the complex-valued wavenumber takes the following form (Bradford, 2007; Griffiths, 1999):

$$\tilde{k} = \beta + \alpha_t i. \tag{1.40}$$

where

$$\beta = \sqrt{\frac{\omega^2\mu_0\varepsilon + \sqrt{\omega^4\mu_0^2\varepsilon^2 - \omega^2\mu_0^2\sigma^2}}{2}}. \tag{1.41}$$

and

$$\alpha_t = \sqrt{\frac{-\omega^2\mu_0\varepsilon + \sqrt{\omega^4\mu_0^2\varepsilon^2 - \omega^2\mu_0^2\sigma^2}}{2}}. \tag{1.42}$$

I use α_t instead of just α to distinguish from the symbol I will later use for seismic wave velocity. In a more useful form, it is evident that β and α_t depend on frequency (Bradford, 2007):

$$\beta = \omega\sqrt{\frac{\mu\varepsilon}{2}\left(\sqrt{1 + \left(\frac{\sigma}{\varepsilon\omega}\right)^2} + 1\right)}. \tag{1.43}$$

$$\alpha_t = \omega\sqrt{\frac{\mu\varepsilon}{2}\left(\sqrt{1 + \left(\frac{\sigma}{\varepsilon\omega}\right)^2} - 1\right)} \tag{1.44}$$

Finally, I substitute $\tilde{k} = \beta + \alpha_t i$ into equation 1.27 and simplify:

$$\boldsymbol{E}(\boldsymbol{x}, t) = E_0 e^{i((\beta + \alpha_t i)\boldsymbol{x} - \omega t)} \tag{1.45}$$

$$\boldsymbol{E}(\boldsymbol{x}, t) = E_0 e^{i(\beta\boldsymbol{x} - \omega t) + i^2\alpha_t x} \tag{1.46}$$

$$\boldsymbol{E}(\boldsymbol{x}, t) = E_0 e^{i(\beta\boldsymbol{x} - \omega t) - \alpha_t x} \tag{1.47}$$

The propagation term is $e^{i(\beta x-\omega t)}$ while the diffusion term is $e^{-\alpha_t x}$. Thus diffusion depends on propagation distance and the magnitude of α_t. The skin depth is inversely proportional to α_t:

$$d = \frac{1}{\alpha_t} \tag{1.48}$$

where d is the skin depth in m since α_t has units of m^{-1}. Equation 1.48 and 1.47 show that the skin depth is the propagation distance such that the original amplitude of the traveling wave is reduced by 1/e. Thus, increasing the value of α_t results in more rapid attenuation of the traveling wave if all other factors are equal. For example, skin depths in metals at GPR frequencies may be on the order of micrometers. On the other hand, reasonable values for α_t in earth materials give corresponding skin depths on the order of meters (Annan, 2005). Finally, the propagation term depends on β and I rewrite equation 1.26 as follows:

$$v = \frac{\omega}{\beta}. \tag{1.49}$$

and one can easily see that velocity depends on frequency as well as the real-valued part of $\tilde{k}$.

Disregarding transient behavior following Griffiths (1999), the divergence of $\boldsymbol{E}$ is zero in earth materials. The divergence of $\boldsymbol{B}$ is zero everywhere via the monopole law (equation 1.6). For the plane-wave monochromatic solution, it is obvious that $\frac{\partial \boldsymbol{E}(\boldsymbol{x},t)}{\partial \mathrm{y}} = 0$ and $\frac{\partial \boldsymbol{E}(\boldsymbol{x},t)}{\partial \mathrm{z}} = 0$, and thus for $\nabla \bullet \boldsymbol{E}$ to be zero, $\frac{\partial \boldsymbol{E}(\boldsymbol{x},t)}{\partial \mathrm{x}} = 0$ and $(E_0)_x$ must be zero. Similarly, $(B_0)_x = 0$. Thus EM waves are transverse, meaning the direction of

polarization is perpendicular to the direction of propagation (Griffiths, 1999). Next, I investigate reflection of such EM waves from subsurface interfaces.

Table 1.1: Relevant subsurface material properties of interest. For simplicity, I list effective conductivity (σ_{ef})* and relative permittivity where $\frac{\varepsilon_{material}}{\varepsilon_0} = \varepsilon_r$. Velocity is approximate. See Chapter 2 for additional discussion.

Material	ε_r	σ_{ef} **(S/m)**	v **(m ns^{-1})**
Air	1	0	0.30
Quartz	4.7	10^{-15}	0.14
Kaolinite	5-10	10^{-8}	0.11
Montmorillonite	5-10	10^{-7}	0.11
Fresh water	80	$10^{-2} – 10^{-3}$	0.03
Salt water	88	1 - 3	0.03
Dry Sand	3-5	10^{-5}	0.15
Saturated Sand	20-30	10^{-2}	0.06
Saturated Clay	5-40	1	0.06
Granite	4-6	10^{-5}	0.13
Ice	3-4	10^{-5}	0.169
Sea Ice	3-8	10^{-1}	0.15

***I take effective conductivity to be the DC conductivity (Annan, 2005).**

Reflectivity

As ***E*** propagates into the subsurface, if it encounters contrasts in material electrical properties (σ and ε) at a subsurface boundary part of the wave energy is reflected back from that boundary. Reflection methods involve measuring and

interpreting that reflected energy. After defining the appropriate coordinate system, I write the incident wave traveling towards the interface in the arbitrary x-direction using equation 1.28:

$$\boldsymbol{E_i}(\boldsymbol{x}, t) = E_i e^{i(k_1 x - \omega t)}\hat{\jmath}. \tag{1.50}$$

Of course, the reflected wave travels in the opposite direction:

$$\boldsymbol{E_r}(\boldsymbol{x}, t) = E_r e^{i(-k_1 x - \omega t)}\hat{\jmath}. \tag{1.51}$$

Subscripts *i* and *r* denotes the incident and reflected waves respectively while subscripts *1* and *2* refer to layers. Thus, k_1 is the wavenumber in the first layer while k_2 would denote the wavenumber in the subsequent layer.

The magnetic field $\boldsymbol{B}$ behaves in the same fashion. Equation 1.31 shows that the magnitude of the magnetic field is proportional to the magnitude of $\boldsymbol{E}$ and that $\boldsymbol{B}$ is oriented at right angles to $\boldsymbol{E}$ (Griffiths, 1999):

$$\boldsymbol{B_i}(\boldsymbol{x}, t) = \frac{1}{v_1} E_i e^{i(k_1 x - \omega t)}\hat{k} \tag{1.52}$$

It follows that the reflected magnetic field has a similar form to equation 1.51:

$$\boldsymbol{B_r}(\boldsymbol{x}, t) = -\frac{1}{v_1} E_r e^{i(-k_1 x - \omega t)}\hat{k}. \tag{1.53}$$

At an interface between two linear materials, the EM wave traveling across the interface must satisfy four boundary conditions (Griffiths, 1999).

Boundary Conditions:

1) The components of $\boldsymbol{E}$ parallel to the interface must be continuous:

$$E_{1\parallel} = E_{2\parallel}. \tag{1.54}$$

2) The ratio of perpendicular components of ***E*** is inversely proportional to the ratio of change in permittivity for the case of zero free change on the boundary:

$$\frac{E_{1\perp}}{E_{2\perp}} = \frac{\varepsilon_2}{\varepsilon_1}. \tag{1.55}$$

3) Since ***B*** is aligned at right angles to ***E***, the perpendicular components of ***B*** must be continuous across the interface. The ratio of the parallel components of ***B*** across the interface is proportional to the ratio of change in μ:

$$B_{1\perp} = B_{2\perp}. \tag{1.56}$$

and

$$\frac{B_{1\parallel}(x,t)}{B_{2\parallel}(x,t)} = \frac{\mu_1}{\mu_2}. \tag{1.57}$$

Combining the boundary conditions with equations 1.50 to 1.53 provides a mean to calculate the amount of the introduced energy that is reflected back. The reflection coefficient *R* is that ratio of reflected to incident energy:

$$R = \frac{E_r}{E_i}. \tag{1.58}$$

In order to derive *R* in a more useful form for an incident EM wave polarized parallel to the plane of interface, I start by substituting equations 1.51 and 1.52 into equation 1.56. Note that B_1 is equal to the sum of the incident and reflected energy while B_2 represents transmitted energy:

$$\frac{(B_{i\parallel}(x,t)+B_{r\parallel}(x,t))}{B_{2\parallel}(x,t)} = \frac{\mu_1}{\mu_2}. \tag{1.59}$$

$$\frac{\frac{1}{v_1}E_i e^{i(k_1 x-\omega t)} - \frac{1}{v_1}E_r e^{i(-k_1 x-\omega t)}}{\frac{1}{v_2}E_t e^{i(k_2 x-\omega t)}} = \frac{\mu_1}{\mu_2}. \tag{1.60}$$

For the purposes of the following discussion, I further assume that conductivity is negligible in the material ($\sigma \ll \varepsilon\omega$). This condition is the "low-loss" criteria for radar wave travel (Annan, 2005). Since $\boldsymbol{B}$ is oriented orthogonally to $\boldsymbol{E}$, I evaluate equation 1.60 at x = 0 and simplify:

$$\frac{\frac{1}{v_1}(E_i - E_r)}{\frac{1}{v_2}E_t} = \frac{\mu_1}{\mu_2} \tag{1.61}$$

For this simplification to be valid at all time and space, I could also evaluate equation 1.60 by only considering the amplitudes of the traveling waves. I proceed by simplifying equation 1.61 as follows:

$$\frac{v_2 E_i - v_2 E_r}{v_1 E_t} = \frac{\mu_1}{\mu_2} \tag{1.62}$$

$$\mu_2 v_2 E_i - \mu_2 v_2 E_r = \mu_1 v_1 E_t \tag{1.63}$$

$$\mu_2 v_2 E_i - \mu_2 v_2 E_r = \mu_1 v_1 (E_i + E_r) \tag{1.64}$$

$$\mu_2 v_2 E_i - \mu_2 v_2 E_r = \mu_1 v_1 E_i + \mu_1 v_1 E_r. \tag{1.65}$$

$$\mu_2 v_2 E_i - \mu_1 v_1 E_i = \mu_1 v_1 E_r + \mu_2 v_2 E_r. \tag{1.66}$$

Dividing through by E_i produces a reformulation of the reflection coefficient:

$$\mu_2 v_2 - \mu_1 v_1 = (\mu_1 v_1 + \mu_2 v_2)\frac{E_r}{E_i} \tag{1.67}$$

$$\frac{\mu_2 v_2 - \mu_1 v_1}{\mu_1 v_1 + \mu_2 v_2} = \frac{E_r}{E_i} = R. \tag{1.68}$$

Equation 1.68 is the formula for calculating the reflection coefficient of the EM wave as it encounters a subsurface layer at normal incidence. Since I assume that the

magnetic susceptibilities of the materials are negligible for my relevant materials of interest, $\mu_1 = \mu_2 = \mu_0$:

$$\frac{v_2 - v_1}{v_2 + v_1} = R. \tag{1.69}$$

Substituting equation 1.26 into equation 1.69 yields the reflection coefficient in terms of ε:

$$\frac{\sqrt{\frac{1}{\mu_0 \varepsilon_2}} - \sqrt{\frac{1}{\mu_0 \varepsilon_1}}}{\sqrt{\frac{1}{\mu_0 \varepsilon_2}} + \sqrt{\frac{1}{\mu_0 \varepsilon_1}}} = R \tag{1.70}$$

$$\frac{\sqrt{\varepsilon_1} - \sqrt{\varepsilon_2}}{\sqrt{\varepsilon_2} + \sqrt{\varepsilon_1}} = R. \tag{1.71}$$

To be more rigorous, I could neglect the assumption that $\sigma \ll \varepsilon\omega$ and instead use the full-form of the complex-valued wavenumber (equation 1.38) to compute R with the following result assuming $\mu_1 = \mu_2 = \mu_0$:

$$\frac{\tilde{k}_1 - \tilde{k}_2}{\tilde{k}_2 + \tilde{k}_1} = R. \tag{1.72}$$

Examining equations 1.72 and 1.39 thereby reveals that radar reflectivity response does in fact depend on σ as well as ε.

In the case of an incidence wave at oblique incidence to the layer boundary, the incidence angle and the orientation of the EM wave polarization with respect to the boundary affect the reflectivity response (Griffiths, 1999). When using broadside acquisition, GPR practitioners refer to the EM wave orientation as transverse electric, or TE, mode. For a 2D medium symmetric about the plane of acquisition, the TE reflection coefficient R_{TE} is given as follows:

$$\frac{\tilde{k}_1 \cos\theta_1 - \tilde{k}_2 \cos\theta_2}{\tilde{k}_1 \cos\theta_1 + \tilde{k}_2 \cos\theta_2} = R_{TE} \tag{1.73}$$

where θ_i is the incidence angle as shown in Figure 1.1. Snell's law allows me to compute the ray parameter in terms of velocities and $\theta_1$and θ_2:

$$p = \frac{\sin\theta_1}{V_1} = \frac{\sin\theta_2}{V_2}. \tag{1.74}$$

Griffiths (1999) provides a derivation of the reflection coefficient for the case where the incident wave is polarized parallel to the plane of reflection. The plane of reflection is the plane perpendicular to the reflecting interface. Such polarization is the transverse magnetic, or TM mode, and has the following reflection coefficient denoted R_{TM} (Annan, 2005):

$$\frac{\tilde{k}_1 \cos\theta_2 - \tilde{k}_2 \cos\theta_1}{\tilde{k}_2 \cos\theta_1 + \tilde{k}_1 \cos\theta_2} = R_{TM} \tag{1.75}$$

Note that in the case of zero incidence angle ($\theta_2 = \theta_1 = 0$), the two reflection coefficient are equal. The angle dependence of the preceding reflection coefficients forms the basis for analyzing the angle-dependent reflectivity response of the subsurface.

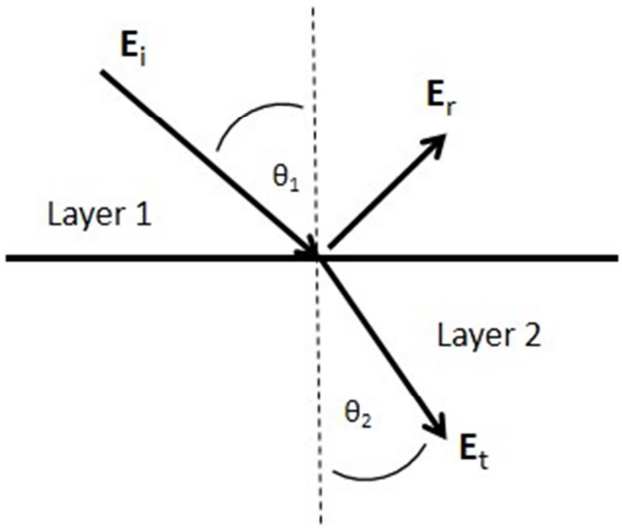

Figure 1.1: Diagram showing incident, transmitted, and reflected plane waves (denoted by arrows) at a subsurface interface marked by contrast in material electric properties.

Seismic Considerations

Seismic energy also propagates as a wave in the subsurface. As a result, there are many similarities between radar reflection and seismic reflection. To derive the wave equations for seismic motion in the subsurface, one starts with the general equation of motion in spatial and time coordinates $\boldsymbol{x}$ and t (Pelton, 2005):

$$\rho(\boldsymbol{x},t)\frac{Dv_i(\boldsymbol{x},t)}{Dt} = \rho(\boldsymbol{x},t)b_i(\boldsymbol{x},t) + \frac{\partial}{\partial \boldsymbol{x}_j}T_{ij}(\boldsymbol{x},t) \tag{1.76}$$

where ρ is density. The left-most term describes the rate of change of the momentum of the body of interest while the right side of the equation is describes the body force (b_i) per unit mass and the surface force ($\frac{\partial}{\partial \boldsymbol{x}_j}T_{ij}(\boldsymbol{x},t)$) acting on the system.

Next, assuming a linearly elastic, homogeneous, and isotropic material allows me to neglect the spatial dependence of material properties as follows (Pelton, 2005):

$$T_{ij}(\boldsymbol{x},t) = \eta\psi(\boldsymbol{x},t)\delta_{ij} + 2\mu_s e_{ij}(\boldsymbol{x},t). \quad (1.77)$$

Here $\psi(\boldsymbol{x},t)$is dilatation; $\delta_{ij}$is the Kronecker delta function; $e_{ij}(\boldsymbol{x},t)$is the strain component; η is the Lamé modulus; and μ_s is the shear modulus (Aki and Richards, 1980; Pelton, 2005). A material's $\mu_s$describes its stiffness or resistance to shear. The Lamé modulus is proportional to the sum of the bulk modulus κ and μ_s:

$$\eta = \kappa - \frac{2}{3}\mu_s. \quad (1.78)$$

The bulk modulus describes a material's resistance to compression. Dilatation is the divergence of the displacement field **u**:

$$\psi(\boldsymbol{x},t) = \nabla \cdot \mathbf{u}(\boldsymbol{x},t) \quad (1.79)$$

and I can write the strain component in terms of displacement gradients:

$$e_{ij}(\boldsymbol{x},t) = \frac{1}{2}\left[\frac{\partial u_j(\boldsymbol{x},t)}{\partial x_i} + \frac{\partial u_i(\boldsymbol{x},t)}{\partial x_j}\right]. \quad (1.80)$$

The next step in deriving the seismic wave equations is to substitute equation 1.77 into equation 1.76. I consider the simplest case. First, I neglect the convective term in the material derivative $\frac{Dv_i(\boldsymbol{x},t)}{Dt}$ as follows:

$$\frac{Dv_i(\boldsymbol{x},t)}{Dt} = \frac{\partial v_i(\boldsymbol{x},t)}{\partial \mathrm{t}} + \boldsymbol{v}(\boldsymbol{x},t) \cdot \nabla v_i(\boldsymbol{x},t) \quad (1.81)$$

$$\frac{Dv_i(\boldsymbol{x},t)}{Dt} = \frac{\partial v_i(\boldsymbol{x},t)}{\partial \mathrm{t}} \quad (1.82)$$

and

$$v_i(\boldsymbol{x},t) = \frac{\partial u_i(\boldsymbol{x},t)}{\partial t}. \quad (1.83)$$

Substituting equation 1.83 into 1.81 provides the following result for the material derivative:

$$\frac{Dv_i(\boldsymbol{x},t)}{Dt} = \frac{\partial^2 u_i(\boldsymbol{x},t)}{\partial t^2}. \tag{1.84}$$

Neglecting the convective term $\boldsymbol{v} \cdot \nabla v_i$ is safe if displacement gradients are small, and this condition generally holds for seismic motion where the wave is propagating relatively far away from its source. In near-surface geophysics, practitioners must be carefully consider when this "far-field" assumption may be invalid.

Next, I substitute equations 1.77 through 1.84 into equation 1.76, assume that ρ is constant, and exclude body forces (b_i = 0). In that case, I am only considering the total surface force (Pelton, 2005):

$$\rho \frac{\partial^2 u_i(\boldsymbol{x},t)}{\partial t^2} = \frac{\partial}{\partial \boldsymbol{x}_j}\left[\eta\big(\nabla \cdot \mathbf{u}(\boldsymbol{x},t)\big)\delta_{ij} + \mu_s\left(\frac{\partial u_j(\boldsymbol{x},t)}{\partial x_i} + \frac{\partial u_i(\boldsymbol{x},t)}{\partial x_j}\right)\right]. \tag{1.85}$$

Assuming our material properties are constant as previously stated, I can gather the components of the displacements $\boldsymbol{u}$. The result is as follows:

$$\rho \frac{\partial^2 \mathbf{u}(\boldsymbol{x},t)}{\partial t^2} = (\eta + \mu_s)\nabla\big(\nabla \cdot \mathbf{u}(\boldsymbol{x},t)\big) + \mu_s \nabla^2 \mathbf{u}(\boldsymbol{x},t). \tag{1.86}$$

Equation 1.86 is the Navier equation. Furthermore the completeness theorem states that any solution to the Navier equation is the sum of a gradient of a scalar field and the curl of a solenoidal field (Pelton, 2005) (A solenoidal field is one whose divergence is zero everywhere, that is, $\nabla \cdot \mathbf{f} = 0$.):

$$\mathbf{u}(\boldsymbol{x},t) = \nabla P(\boldsymbol{x},t) + \nabla \times \boldsymbol{S}(\boldsymbol{x},t). \tag{1.87}$$

Both P and $\boldsymbol{S}$ also satisfy wave equations of the following forms:

$$\nabla^2 P(\boldsymbol{x},t) - \frac{1}{v_p^2}\frac{\partial^2 P(\boldsymbol{x},t)}{\partial \mathrm{t}^2} = 0 \tag{1.88}$$

and

$$\nabla^2 \boldsymbol{S}(\boldsymbol{x},t) - \frac{1}{v_s^2}\frac{\partial^2 \boldsymbol{S}(\boldsymbol{x},t)}{\partial \mathrm{t}^2} = 0 \tag{1.89}$$

where v_s and v_p are the velocity of the S-wave and P-wave, respectively, and are given by $v_p = \sqrt{\frac{\eta+2\mu_s}{\rho}}$ and $v_s = \sqrt{\frac{\mu_s}{\rho}}$ (Pelton, 2005). Acknowledging the assumption that ρ and μ_s are constant, I can take the the divergence of the Navier equation to arrive at the following equations:

$$\nabla \cdot \rho \frac{\partial^2 \mathbf{u}(\boldsymbol{x},t)}{\partial t^2} = \nabla \cdot [(\eta + \mu_s)\nabla\big(\nabla \cdot \mathbf{u}(\boldsymbol{x},t)\big) + \mu_s \nabla^2 \mathbf{u}(\boldsymbol{x},t)] \tag{1.90}$$

$$\rho \frac{\partial^2}{\partial t^2}\nabla \cdot \mathbf{u}(\boldsymbol{x},t) = (\eta + \mu_s)\nabla \cdot \nabla\big(\nabla \cdot \mathbf{u}(\boldsymbol{x},t)\big) + \mu_s \nabla \cdot \nabla^2 \mathbf{u}(\boldsymbol{x},t)]. \tag{1.91}$$

Using equation 1.79, I can simplify the preceding equation and write it in terms of the dilatation:

$$\rho \frac{\partial^2}{\partial t^2}\psi(\boldsymbol{x},t) = (\eta + \mu_s)\nabla^2 \psi(\boldsymbol{x},t) + \mu_s \nabla^2 \psi(\boldsymbol{x},t) \tag{1.92}$$

$$\rho \frac{\partial^2}{\partial t^2}\psi(\boldsymbol{x},t) = (\eta + 2\mu_s)\nabla^2 \psi(\boldsymbol{x},t) \tag{1.93}$$

$$(\eta + 2\mu_s)\nabla^2 \psi(\boldsymbol{x},t) - \rho \frac{\partial^2}{\partial t^2}\psi(\boldsymbol{x},t) = 0 \tag{1.94}$$

$$\nabla^2 \psi(\boldsymbol{x},t) - \frac{\rho}{\eta+2\mu_s}\frac{\partial^2}{\partial t^2}\psi(\boldsymbol{x},t) = 0. \tag{1.95}$$

Comparison of equation 1.95 with the P-wave equation (1.88) confirms that the P-wave velocity is related to the physical and mechanical material properties as stated previously:

$$v_p = \sqrt{\frac{\eta+2\mu_s}{\rho}} \tag{1.96}$$

Thus, the velocities of seismic waves depend on 3 physical properties (density, stiffness, and compressional strength). In contrast, according to equation 1.26, the velocity of EM wave propagation depends on 2 physical properties: the magnetic permeability and the permittivity of the material. Table 1.2 gives relevant representative material properties. Similarly, the seismic reflection coefficients depend on the angles of incidence and reflection as well as ρ, v_s, and v_p. For example, the acoustic reflection coefficient (R_p) is given by the following equation for a plane wave normally incident on a horizontal interface between two layers, 1 and 2 respectively (Aki and Richards, 2002):

$$R_p = \frac{\rho_2 v_{p2} - \rho_1 v_{p1}}{\rho_2 v_{p2} + \rho_1 v_{p1}} \tag{1.97}$$

The product of density and seismic velocity is impedance and of course Snell's law still applies to $\theta_1$and θ_2 (Booth et al., 2013). Note the similarities and differences between equation 1.97 and the reflection coefficient for EM waves (equations 1.69 and 1.75). Under our extensive simplifying assumptions and not considering either conductivity or seismic quality factor, one observes that the EM wave reflections exhibit a first-order dependency on just one material property (ε), while seismic wave reflections depend both on ρ and on v. The coupled nature of those two seismic properties may complicate estimation of material properties such as porosity or the application of ill-constrained geophysical techniques such as inversion algorithms.

Of course when seismic energy encounters a subsurface layer, there is P- and S-wave splitting across the boundary, such that an incident P-wave results in transmitted and reflected P- and S-waves and both P- and S-wave reflection coefficients (Castagna,

1993) (Figure 1.2). I discuss the more general case for all seismic reflection coefficients and the elastic case for the P-wave reflection coefficient in the next section.

Table 1.2: Representative seismic material properties (Burger et al., 2006; Press, 1966). All properties depend on pressure and temperature.

Material	v_p (m s^{-1})	V_s (m s^{-1})	ρ (kg m^{-3})
Air	330	0	1.275
Water	1400-1600	0	1000
Ice	3600-3800	917	917
Saturated Sand	800 - 2200	400 - 600	1500 - 2400
Unsaturated Sand	200 - 1200	100 -500	500 - 1700
Clay	1100 – 2500	200 - 800	2000 - 2400
Shale	1400-1600	1400 - 2000	2670
Sandstone	2000 - 3500	500 - 1700	2100 - 2400
Granite	4500 - 6000	2500 - 3300	2500 – 2700
Basalt	5000 - 6000	2800 – 3400	2700 - 3100

Examples and Thin-Layer Problems

In the preceding sections, I demonstrated how the propagation of wave energy in the subsurface depends on material properties that influence the velocity of the wave in either the seismic or the radar case. Changes in material properties across an interface cause some energy to be reflected back to the subsurface. A plethora of data collection techniques, data processing methods, and petrophysical transformations enable us to examine those reflections and derive information about the subsurface. For example, assuming a plane-wave contacting an infinite planar interface between two homogeneous, isotropic, linearly elastic half spaces, the Zoeppritz equations provide the full solution for

16 reflection and transmission coefficients for both P- and S-waves as a function of angle of incidence (Aki and Richards, 2002) (Figure 1.2):

$$\mathbf{Q}=\mathbf{P}^{-1}\mathbf{R}=\begin{bmatrix} P'P'' & S'P'' & P''P'' & S''P'' \\ P'S'' & S'S'' & P''S'' & S''S'' \\ P'P' & S'P' & P''P' & S''P' \\ P'S' & S'S' & P''S' & S''S' \end{bmatrix} \tag{1.98}$$

where $'$ denotes down-going waves and " denotes up-going waves. For example, $P'P''$ represents a down-going P-wave reflected to an up-going one; thus $P'P''$ is the elastic P-wave reflection coefficient as compared to equation 1.97 for the acoustic reflection coefficient. Similarly $P'S''$ represents a down-going P-wave reflected to an up-going S-wave and $P'S''$ is the standard S-wave reflection coefficient. To further hammer the point home, consider that $P'P'$ represents a down-going P-wave transmitted to down-going P-wave is therefore the P-wave transmission coefficient. The matrices **P** and **R** are functions of incidence angles and seismic properties:

$$\mathbf{P}=\begin{bmatrix} -\sin\theta_1 & -\cos\varphi_1 & \sin\theta_2 & \cos\varphi_2 \\ \cos\theta_1 & -\sin\varphi_1 & \cos\theta_2 & -\sin\varphi_2 \\ 2\rho_1 v_{S_1}\sin\varphi_1\cos\theta_1 & \rho_1 v_{S_1}(1-2\sin^2\varphi_1) & 2\rho_2 v_{S_2}\sin\varphi_2\cos\theta_2 & \rho_2 v_{S_2}(1-2\sin^2\varphi_2) \\ -\rho_1 v_{P_1}(1-2\sin^2\varphi_1) & \rho_1 v_{S_1}\sin 2\varphi_1 & \rho_2 v_{P_2}(1-2\sin^2\varphi_2) & -\rho_2 v_{S_2}\sin 2\varphi_2 \end{bmatrix} \tag{1.99}$$

and

$$\mathbf{R}=\begin{bmatrix} \sin\theta_1 & \cos\varphi_1 & -\sin\theta_2 & -\cos\varphi_2 \\ \cos\theta_1 & -\sin\varphi_1 & \cos\theta_2 & -\sin\varphi_2 \\ 2\rho_1 v_{S_1}\sin\varphi_1\cos\theta_1 & \rho_1 v_{S_1}(1-2\sin^2\varphi_1) & 2\rho_2 v_{S_2}\sin\varphi_2\cos\theta_2 & \rho_2 v_{S_2}(1-2\sin^2\varphi_2) \\ \rho_1 v_{P_1}(1-2\sin^2\varphi_1) & -\rho_1 v_{S_1}\sin 2\varphi_1 & -\rho_2 v_{P_2}(1-2\sin^2\varphi_2) & \rho_2 v_{S_2}\sin 2\varphi_2 \end{bmatrix} \tag{1.100}$$

where v_{S_1} and v_{P_1} are the S- and P-wave velocities respectively in Layer 1; v_{S_2} and v_{P_2} are the S- and P-wave velocities respectively in layer 2; ρ_1 and ρ_2 are the densities of each

layer fill; θ_1 and θ_2 are the incident and transmitted P-wave angles; $\varphi_1$and φ_2 are the incident and transmitted S-wave angles respectively; and Snell's law relates the P- and S-wave angles (Castagna, 1993) (Figure 1.2):

$$p = \frac{\sin\theta_1}{v_{P_1}} = \frac{\sin\theta_2}{v_{P_2}} = \frac{\sin\varphi_1}{v_{S_1}} = \frac{\sin\varphi_2}{v_{S_2}} \tag{1.101}$$

Unique combinations of the physical properties of the materials influencing **P** and **R** (i.e. ρ and v) give rise to unique changes in reflection coefficients as the angle of incidence changes as demonstrated by Figure 1.2. This technique is amplitude variation with offset (AVO) analysis or amplitude variation with angle (AVA) analysis. Either name is valid since angle of incidence is a function of offset. Modeling and inversions based on AVA/AVO curves may enable skilled practitioners to estimate subsurface parameters. However, the Zoeppritz equations are not valid if a thin layer is present between the two half-spaces and one must turn to reflectivity modeling or numerical solutions.

Another common tool for interpreting reflection data is velocity analysis (Yilmaz, 2002). As previously stated, the velocity of the seismic wave depends on the physical properties of the material (equation 1.96) and the velocity of the radar wave is a function of the electrical properties (equation 1.26). If one measures the velocity of the wave in the material, one can use those equations to quantify the material properties. Subsequent judicious use of petrophysical transformations can provide information about a range of parameters including porosity, pore geometry, grain size distribution, and pore fluids. Recovering information about pore geometry and pore fluids is particularly relevant to hydrocarbon exploration and extraction (Aki and Richards, 1980). Using GPR to estimate pore fluid properties may help contaminated site managers delineate source zones and

contaminant plumes and subsequently prioritize remediation efforts (Bradford and Deeds, 2006).

In either case, the foundation of conventional velocity analysis is the normal moveout (NMO) traveltime equation (Yilmaz, 2002):

$$t^2 = t_0^2 + \frac{x^2}{v^2} \tag{1.102}$$

where t is traveltime, t_0 is zero-incidence traveltime, x is separation between source and receiver, and v is velocity. This equation assumes planar horizontal layers and is limited to small angles of incidence. More advanced techniques include dip moveout analysis and pre-stack depth migration (PSDM). These provide more accurate velocity analysis in the face of subsurface irregularities or large angles of incidence. The hydrocarbon exploration industry has been using such methods for years, and more recently GPR practitioners have expanded those techniques for use with radar data (Yilmaz, 2002; Bradford, 2002; Bradford, 2006).

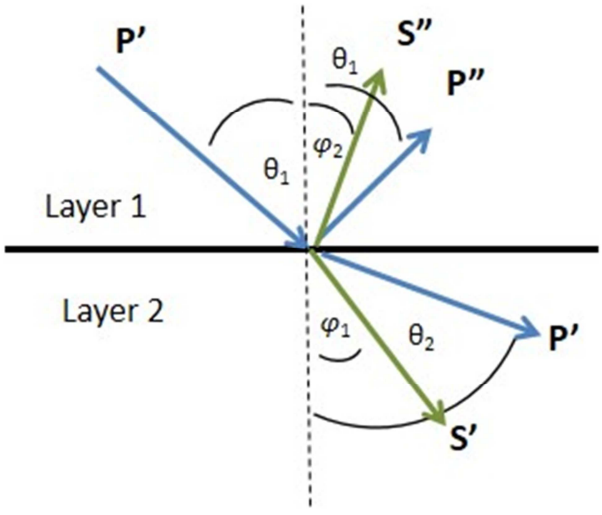

a)

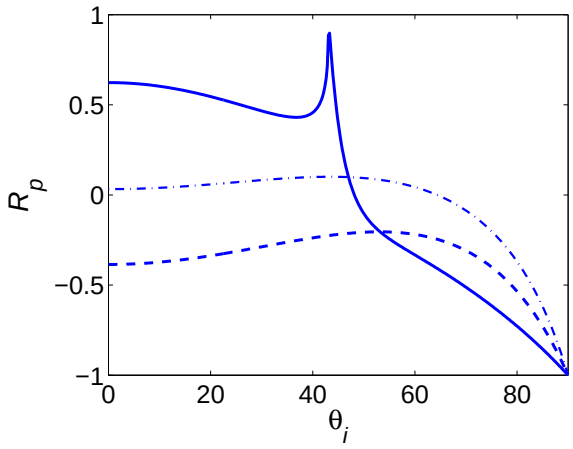

b)

Figure 1.2: a) Schematic demonstrating P- and S-wave reflections and transmissions if $v_1 < v_2$; compare to Figure 1.1. b) P-wave reflection coefficients (*Q(1,1)*, equation 1.64) versus angle of incidence (θ_i) for three different models: glacier ice (v_p = 3690 m s^{-1}, ρ = 917 kg m^{-3}) overlying bedrock (v_p= 5400 m s^{-1}, ρ = 2700 kg m^{-3}) (solid line); glacier ice overlying till (v_p= 2000 m s^{-1}, ρ = 1900 kg m^{-3}) (dash-dot line); and glacier ice overlying water (v_p= 1500 m s^{-1}, ρ = 1000 kg m^{-3}) (dashed line) with R_p calculated using the full form of the Zoeppritz equations and material properties given in Table 1.2 (following Booth et al., 2013). Note that these reflection coefficients are only accurate for a reflection from 2 homogeneous, isotropic, welded half spaces, which does not accurately account for the presence of a thin layer.

Nevertheless, I proceed using equation 1.102. Since reflection methods record traveltime at the surface, for one layer I calculate subsurface layer velocity as a function of x and t:

$$v_{nmo} = \sqrt{\frac{x^2}{t^2 - t_0^2}} \tag{1.103}$$

One can also sometimes apply this equation to reflections recorded from subsequent planar interfaces and transform the NMO velocity into a layer interval velocity using the Dix equation (Yilmaz, 2002)

Where thin-layers are present in the subsurface, NMO velocity analysis fails. If a layer is below some limiting layer thickness, the reflections from the top and bottom of that layer are inseparable (Figure 1.3) (Widess, 1973). The theoretical limit for such resolution of reflection events is ⅛λ. However, additional considerations such as noise and signal characteristics make the practical limit for wavelet separation ½λ or even ¾λ (Bradford and Deeds, 2006). Without adequate separation of these reflection events, velocity analysis of the layer fill using travel-time methods is impossible. Practical limits for velocity analysis even using PSDM are wavelet separations of 1 - 2λ. In addition, conventional travel-time analysis of such a layer cannot reliably quantify layer thickness, and practitioners must turn to other analysis tools.

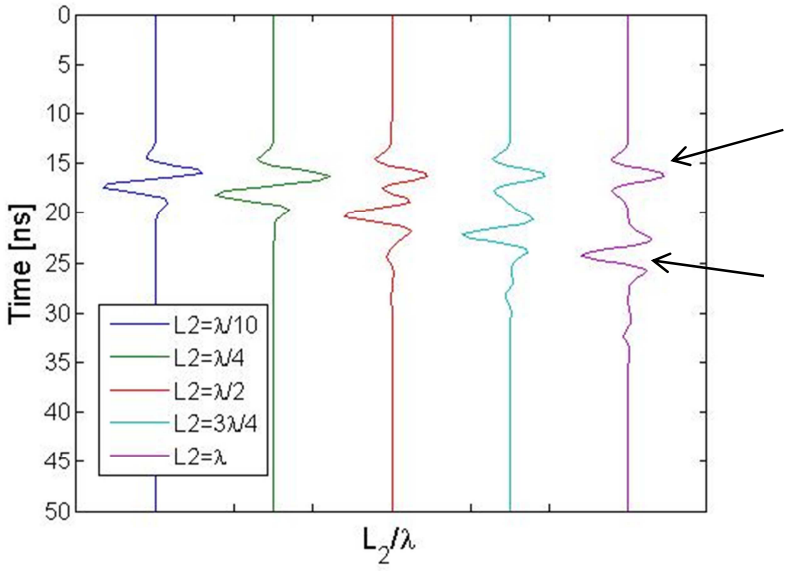

Figure 1.3: Wavelets for reflection event from a representative 3-layer system where the second layer (L2) has thickness ranging from λ/10 to λ. Note that where L2= λ (right-most trace), two reflection events are clearly present, from the top and bottom of L2 (arrows). However, below L2=3λ/4, the upper and lower reflections become convolved with one another, making clear identification impossible. (Annan, 2005; Widess, 1973).

Having demonstrated that conventional tools fail in the presence of thin layers, finally I briefly summarize 2 techniques that may be able to quantify thin-layer parameters: attribute and inversion methods.

Introduction to Attribute Analysis for Thin Layers

The attributes of the thin-bed reflectivity response depend of course on the material properties of all layers involved (Annan, 2005). Previous work with seismic and radar methods has demonstrated that analyzing instantaneous phase, instantaneous frequency, reflection strength, and AVO response may allow detection of thin subsurface layers (Booth et al., 2013; Bradford and Deeds, 2006; Bradford et al., 2010; Deparis and Garambois, 2009; Orlando, 2002; Smith, 2007; Taner et al., 1979). In the presence of a thin layer sandwiched between two half spaces, the bulk reflection response becomes a summation of successive reflection and transmission coefficients from the top and bottom of the layered stack (Annan, 2005).

In Chapter 2, I describe a method for depicting that reflection response using a 1D model. Here I use that model to demonstrate that changes in layer thickness can increase or decrease the reflection amplitude as well as alter the reflection phase (Figure 1.4) (Bradford et al., 2010). The model simulates a saturated sand (ε_r =22) overlying saturated clay (ε_r =35). For the thin layer case, I introduce a simulated thin layer of a common environmental contaminamt (ε_r =7) at the sand/clay interface. I calculate the reflectivity response at normal incidence at 1500 MHz for 2 layer thicknesses: 0.2λ and 0.1λ. Qualitatively, visual inspection of the resulting waveforms shows changes in both wavelet shape and amplitude as the thin-layer thickness decreases (Figure 1.4).

Figure 1.5 demonstrates similar response in a laboratory data set. Here I collected data over saturated sand/clay system in a plastic tank in the laboratory. Details of the experiment and data collection are in Chapter 3. The physical layer properties match those used in the previous 1D model, but I show the processed data for the control case (no thin layer present) and a thin layer with layer thickness (d) = 3%λ. Again, qualitatively it is easy to identify an amplitude anomaly where the thin-layer is present.

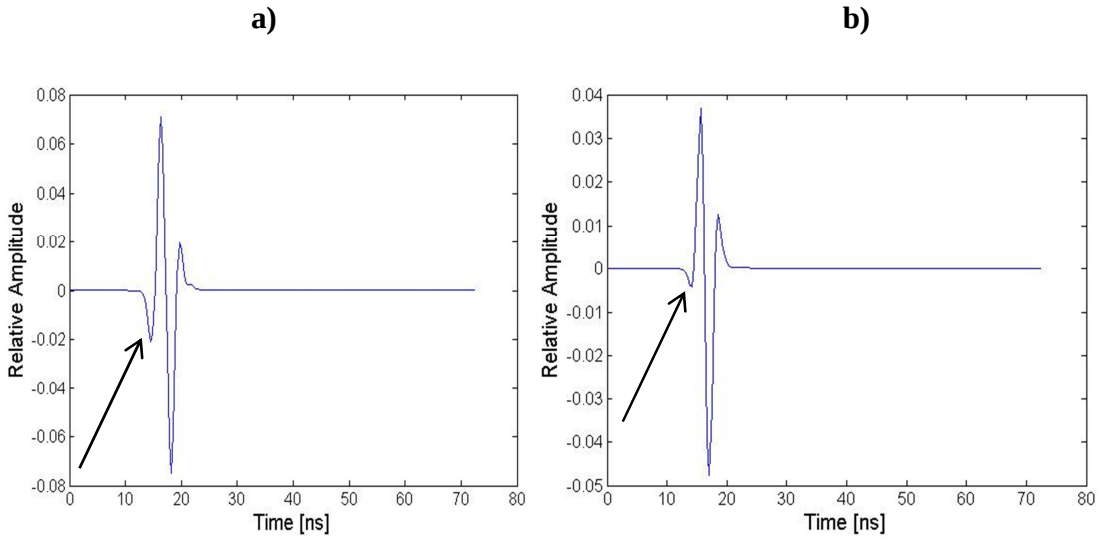

Figure 1.4: Modeled changes in reflection characteristics for a) L2=0.2λ and b)L2=0.1λ where L2 is the thin-layer thickness in a 3 layer model. Reflectivity response is from a 1D radar reflectivity model that I will describe in Chapter 2. Layer properties simulate a saturated sand (ε_r =22) / saturated clay(ε_r =35) system with a thin layer of a common environmental contaminamt (ε_r =7) present at the sand/clay interface. Relative changes in reflection phase and amplitude (note scale) are obvious in the thin-layer response of this model. For example, compare the leading edges of the two reflection events (arrows).

However, the real goal is to quantitatively assess such changes. In subsequent chapters, I use a targeted full-waveform inversion to quantitatively assess layer properties. Here, I also compare the data against a 2D model in an attempt to extract quantitative information. I use a 2D Finite-Difference Time-Domain (FDTD) algorithm

to model the laboratory experiment shown in Figure 1.5 (Figure 1.6). (For an explanation of FDTD models, see Irving and Knight (2006) and Yee (1966). Numerical analysis reveals that the reflection strength change in the model between the control and the thin layer is within 5% of the changes noted in the data for the two cases. Five percent is well within level of noise in of the data. The similarity between the model and data result is especially remarkable especially considering the thinness of the modeled and measured layers (<10%λ). Comparing relative changes in attributes between the laboratory and model data may provide some information about layer properties. Thus, one can see that using attributes in conjunction with modeling efforts may overcome some of the difficulties inherent with interpreting thin subsurface layers.

Furthermore, AVA analysis may still prove a useful tool even in the presence of thin beds. For example, Bradford and Deeds (2006) use a formulation of the reflectivity response for a 3-layered system to derive AVA curves in the presence of a thin-layer. Figure 1.7 demonstrates extraction of AVA curves from model data using the 1D reflectivity model for the same saturated sand/clay system. These data provide quantitative differences in reflection amplitude and change in reflection strength with increasing incidence angle and increasing layer thickness (Figure 1.7).

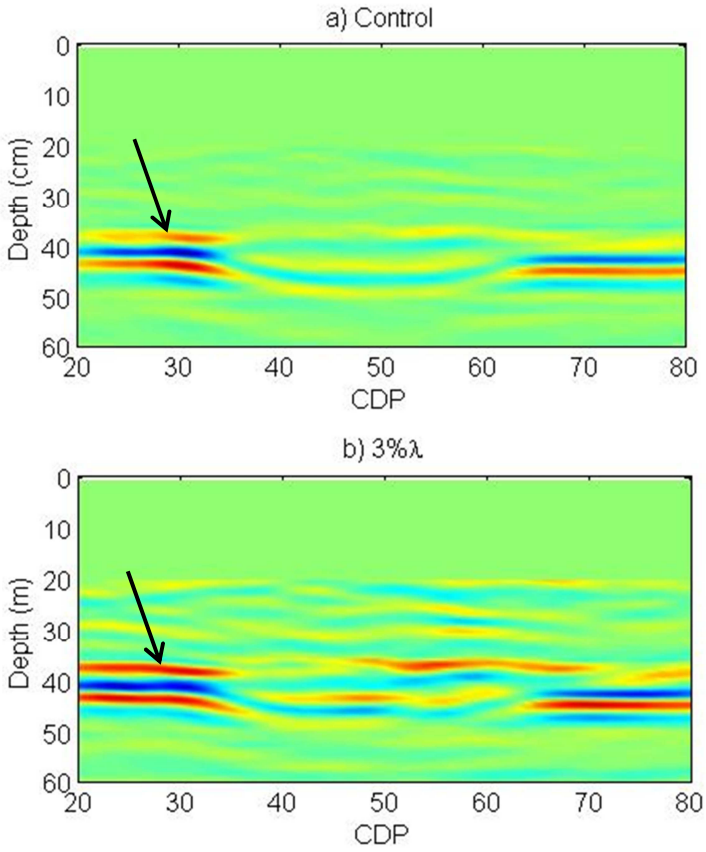

Figure 1.5: Laboratory data demonstrating changes in reflection characteristics using 1 GHz pulsed GPR data collected over a tank filled with saturated sand overlying saturated clay (for more details on data collection and processing see Chapter 3). The sand/clay boundary is approximately at 40 cm, and the sand/clay reflection event is clearly visible in both cases (arrows); Wavelets are color coded with respect to amplitude; i.e. a red/blue/red event corresponds to a wave trough/peak/trough. The depression located at CDP 40-60 contained no thin layer in a) but a 0.005 m layer (3%λ) of a simulated contaminated in b). Note the relative change in reflection strength (28% increase) and characteristics in the presence of the thin layer.

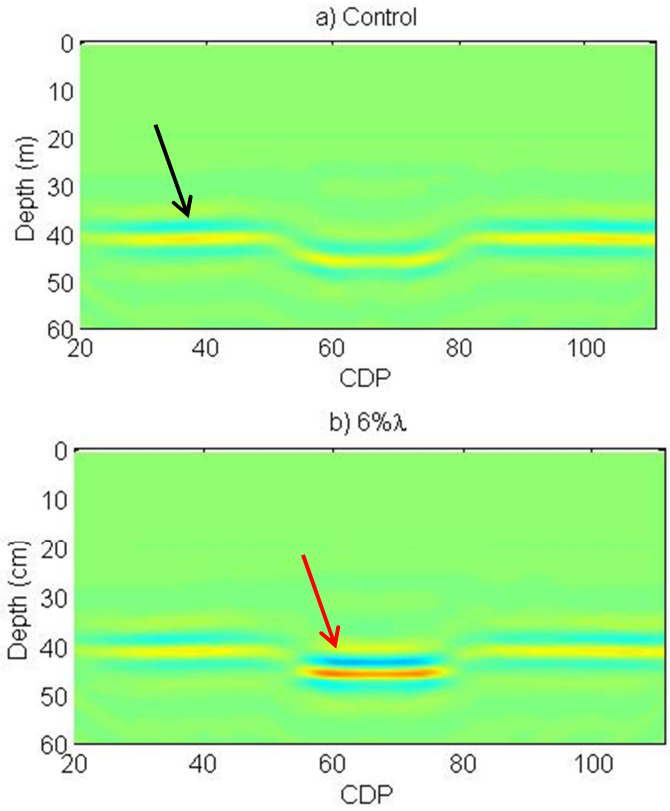

Figure 1.6: Synthetic data from a 2D model with a source frequency of 450 MHz and a model space simulating the laboratory conditions in Figure 1.5. Black arrow annotates the sand/clay reflection event; red arrow points to region of increased reflection strength where the simulated thin layer is present. Although the layer thickness in part b) is twice that in Figure 1.5b, numerical analysis reveals that the reflection strength increase for the same layer thickness (not shown) from Figure 1.5a) to Figure 1.5b) is 51% while for the model case shown is 54%. The similarity between the model and data result is remarkable especially considering the thinness of the layer (only 6%λ).

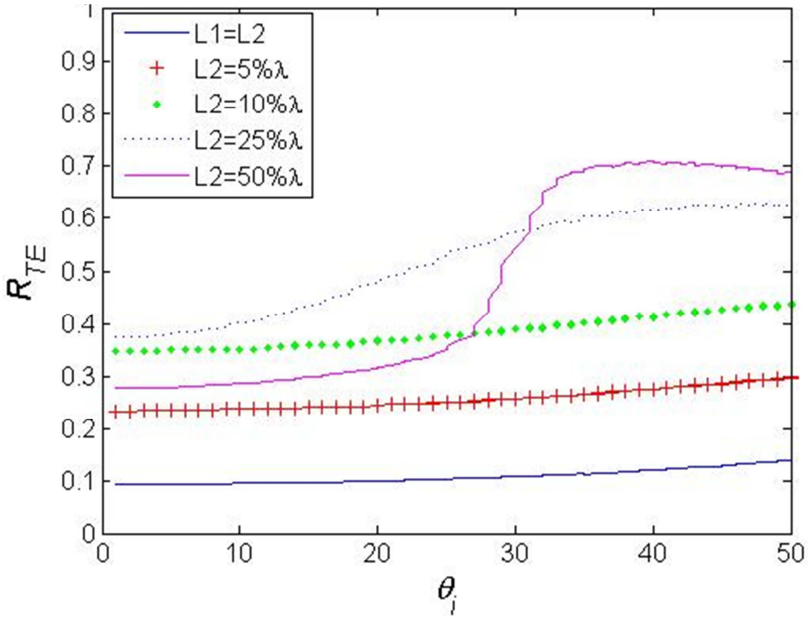

Figure 1.7: The modeled reflectivity response of the 3-layer system given in Figure 1.4 using the same 1D reflectivity model (to be described in Chapter 2). I give Layer 2 (L2) thickness as %λ; L1 = L2 is the case where no thin layer is present. Note that both the zero-offset reflection coefficient and the slope of the AVA curve may change with increasing layer thickness. Quantifying this change and comparing to the AVA response in a field data set may allow interpreters to detect thin layers and estimate thin-layer properties (following Bradford and Deeds, 2006).

Inversion Methods

The previous examples provided some insight into the use of models to understand subsurface response particularly in the presence of thin layers. Skilled practitioners can sometimes detect thin layers and estimate their parameters based on comparison of model data to the field or laboratory data. Such a process is often time-intensive and inexact. A more rigorous approach to deriving thin layer properties from reflection data could provide robust and accurate estimates of those properties. For that geophysicists often turn to inverse methods. Here I present a short discussion and example of inversion methodology.

When using radar or seismic reflection methods, one records information at the surface that arises due to subsurface properties. Inverse methods apply various algorithms to the recorded data in an attempt to recover earth properties (Figure 1.8) (Aster et al., 2005).

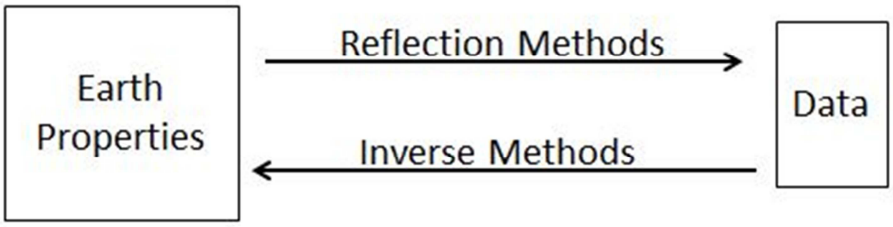

Figure 1.8: Schematic illustrating the difference between forward methods (e.g., reflection methods) and inversion.

Inverse methods often use a synthetic model to replicate the data response and then iteratively minimize the misfit between the observed data and that synthetic model. Inverse theory implies that modeled parameters relate to measured data in a coherent, meaningful fashion (Menke, 1984). A simplified summary of example ordinary least squares inversion (OLS) for reflection data proceeds as follows:

$$\boldsymbol{Gm} = \boldsymbol{d} \tag{1.104}$$

where **G** is an *n* x *m* matrix having *n* receivers to record the subsurface reflection event and *m* subsurface layers; $\boldsymbol{m}$ is an *m* x 1 vector of parameters; and $\boldsymbol{d}$ is an *n* x 1 vector of observed travel times (s). Having recorded $\boldsymbol{d}$ at the surface, I want to find $\boldsymbol{m}$, the subsurface parameters. I can calculate a relevant model, using perhaps a 1D reflectivity model or a 2D FDTD model. Then, I can implement an inversion algorithm to minimize the misfit $\boldsymbol{r}$ between the calculated model and the real data:

$$\boldsymbol{r} = \boldsymbol{d} - \boldsymbol{Gm} \tag{1.105}$$

Inverse methods often iteratively update the model parameters in an effort to minimize the misfit. Where such minimization is possible, the solution then corresponds to the parameter values that produce the minimum misfit when applied to the model. Unfortunately, one daunting and ubiquitous problem for inversion methods is that such a minimum may be only a local value and not a global one. Ongoing research continues to investigate and mitigate the problems inherent in enhancing algorithm convergence to the global minimum even in the presence of many local minimum.

In any case, in this OLS example, assuming the solution exists I can estimate $\boldsymbol{m}$ as follows:

$$\boldsymbol{m} = [\mathbf{G}^{\boldsymbol{T}}\mathbf{G}]^{-\mathbf{1}}\mathbf{G}^{\boldsymbol{T}}\boldsymbol{d} \tag{1.106}$$

where the superscript *T* indicates the matrix transpose and superscript -1 indicates the matrix inverse. If I find a solution, next I need to estimate the robustness of my solution. Assuming constant, uncorrelated data errors, the parameter covariance matrix $\boldsymbol{C_m}$ is a function of the data covariance (σ^2):

$$\mathbf{C}_{\boldsymbol{m}} = [\mathbf{G}^{\boldsymbol{T}}\mathbf{G}]^{-\mathbf{1}}\mathbf{G}^{\boldsymbol{T}}\sigma^2([\mathbf{G}^{\boldsymbol{T}}\mathbf{G}]^{-\mathbf{1}}\mathbf{G}^{\boldsymbol{T}})^{\mathrm{T}} \tag{1.107}$$

Finally, I can use the parameter covariance in combination with statistical methods such as the student's *T* distribution to bound the confidence intervals of the solution (Aster et al., 2005; Menke, 1984).

The preceding discussion was a simplified discussion of some of the methodology for a linear inverse problem. A plethora of inversion problems and algorithms exist, many of them exceedingly more complicated and often non-linear. Unfortunately, all these

inverse methods are plagued by monstrous problems, which include the following: 1) the solution may not exist; 2) if it does exist, the solution may be non-unique; 3) inverse problems may be ill-constrained or ill-posed; and 4) required computing time may be prohibitive (Aster et al., 2005).

Nevertheless, geophysical inverse methods provide a powerful weapon in the face of thin-layer problems in reflection data. For example, an inversion algorithm could potentially provide a quantitative, bounded solution for a subsurface thin-layer parameter, such as permittivity or thickness or both, by minimizing the misfit between observed AVO curves and a subsurface layered model (Deparis and Garambois, 2009). Even such a relatively simple inversion would provide a more robust and reliable technique than trial and error curve fitting.

A real advance in subsurface parameter estimation has occurred in the past thirty years with the advent of full-waveform inversions (FWIs) (Plessix et al., 2012). These inversion problems are non-linear and require advanced computational power far beyond what might be necessary for the linear OLS squares example I presented in this section. However, full-waveform inversions are able to directly invert for subsurface parameters. As such, they are uniquely able to incorporate all the information within recorded data, including the attributes, which often are relevant to thin-layer detection. Thus, these methods lend themselves to quantification of thin-layer properties. I discuss FWI more thoroughly in Chapters 2 through 4.

Overview of Research

The following chapters detail my efforts to create and test a novel targeted full-waveform inversion algorithm that can reliably quantify thin-layer parameters and a new

method to provide high-quality, reliable data for use within the inversion algorithm even in the presence of subsurface anisotropy (Chapter 5). Each chapter is a separate paper for publication. I have submitted Chapters 2 and 3 to *Geophysics*, Chapter 4 to *Journal of Glaciology*, and Chapter 5 to *Cold Regions Science and Technology*.

Chapter 2 begins by providing an in-depth discussion of the thin-layer problem as related to radar reflection data. Previous research has noted that attribute analysis such as AVO techniques may allow some detection and qualification of thin-layer properties, but in an effort to rigorously and reliably quantify those properties, I introduce a novel targeted full-waveform inversion algorithm. Chapter 2 provides a detailed description both of the inversion methodology and 1D vertical-incidence forward model. I use the reflectivity model to produce synthetic data for testing. The second chapter concludes by demonstrating the reliability of the targeted FWI as tested on synthetic data simulating thin subsurface layers of contamination: in all cases, the FWI recovered thin-layer permittivity and thickness within 10% of true values. I also test the sensitivity of the inversion to thin-layer thickness and conductivity using the synthetic data.

Chapters 3 and 4 describe inversion testing on field data. Chapter 3 gives my methodology and results for testing the targeted FWI on 4 field GPR reflection data sets. In each data set one of three different contaminants (oil and two different NAPLs) was present in a thin layer in the subsurface. The targeted inversion approach reliably recovers thin-layer parameters within 15% of real estimated values even for noisy field data. Chapter 4 demonstrates the use of the inversion algorithm as adapted to seismic reflection data. I test the algorithm both on synthetic data and also on field data collected

at Bench Glacier, Alaska. Careful analysis of the inversion results provides a greater understanding of basal conditions in the survey area.

Finally, Chapter 5 introduces a new dual-polarization radar system that uses reflection methodology to reliably image subsurface interfaces even in the presence of strong conductivity anisotropy. In particular, collecting radar data with this new system over sea ice provides a reliable image of the ice-water interface when traditional radar systems have failed to do so. Since my targeted inversion algorithm requires high-quality reflection data, this system contributes a vital component in this specific situation. Furthermore, in the event of an oil spill in or under sea ice combined use of the dual-polarization system for data collection in conjunction with my inversion algorithm for data analysis could help direct and prioritize remediation efforts.

As part of my PhD work, I have undertaken a minor focal area concentrating on the role of science within public policy and decision making for public lands and resource management. Public policy for these decisions often includes a scientific component, although both scientists and policy makers frequently and vigorously debate the relative weight and merit of that inclusion. I began my graduate work as the Department of Geosciences relocated into a new university building, the Environmental Research Building (ERB). Boise State University simultaneously moved the Departments of Civil Engineering (CE), Political Science, Public Administration, and Community and Regional Planning to the ERB with the stated goal of fostering “interdisciplinary collaboration” and promoting “research aimed at the pressing issues of the West, including the environment, energy, transportation, water, land use, and community planning.” Thus I had the fortunate opportunity to study the role of this new building as a

boundary construct that might bridge a perceived gap between scientists and policy makers. Appendix A presents a literature summary of boundary theory relevant to this problem and provides results from my research examining the role of the ERB as a boundary object.

CHAPTER TWO: TARGETED FULL-WAVEFORM INVERSION OF GROUND-PENETRATING RADAR REFLECTION DATA FOR THIN AND ULTRA-THIN LAYERS OF NON-AQUEOUS PHASE LIQUID CONTAMINANTS PART I: ALGORITHM AND SYNTHETIC MODELING

Abstract

Quantification of thin-layer parameters is a ubiquitous problem in near-surface investigations using ground-penetrating radar (GPR). We implement a full-waveform inversion algorithm to quantify thin-layer permittivity (ε), thickness (d), and conductivity (σ) for non-aqueous phase liquid (NAPL) thin ($\leq$½ dominant wavelength λ) and ultra-thin ($\leq$⅛λ) layers using GPR reflection data. The inversion uses a non-linear grid search with a Monte-Carlo scheme to initialize starting values to find the global minimum. We tested the inversion on 3 different thin ($\leq$½λ) and ultra-thin ($\leq$⅛λ) layer models with 5% added Gaussian noise. The models simulate oil overlying sea water, a dense NAPL (DNAPL) trapped at a sand/clay interface, and saturated sand overlying bedrock, respectively. In all cases, the inversion retrieved thin-layer permittivity and thickness within 10% of true values. The inversion demonstrates a robust capability to quantify ultra-thin-layer properties across a range of source functions and subsurface conditions relevant to NAPL detection and remediation. By taking a targeted approach, our algorithm reduces the complexity in the inverse problem. It appears especially useful for monitoring thin-layers at contaminated sites.

Introduction

The anthropogenic release of non-aqueous phase liquid (NAPL) contaminants causes environmental degradation and has deleterious impacts on human health (Hwang et al., 2008). Although environmental regulations in the past 40 years have reduced intentional and accidental discharge, long-term releases of NAPLs have historically occurred through improper disposal in unlined pits, leaking underground storage facilities, and other mechanisms. Such long-term releases can introduce correspondingly large quantities of NAPLs into the subsurface. On the other hand, short-term accidental pollution events, e.g. oil spills, can also release large quantities of NAPLs with similar long-term implications for ecosystem functioning (Chapman and Riddle, 2005; Sydnes et al., 1985).

NAPL contaminants fall into one of two categories: 1) Light-NAPLs (LNAPLs), which are less dense than water; and 2) Dense NAPLs (DNAPLs), which are denser than water. Examples of LNAPLs are crude oil, jet fuels, and gasoline. DNAPL contaminants include chlorinated solvents such as trichloroethylene (TCE) and tetrachloroethylene (PCE). Ubiquitous sources of NAPL contamination are dry-cleaning operations and aircraft maintenance facilities, where pit disposal of organic solvents and jet fuels was commonplace for decades (Brusseau et al., 2011; Nellis et al., 2009).

LNAPL and DNAPL release, subsequent migration, and entrapment have polluted aquifers throughout the world. Aquifer degradation is especially problematic given the implications of climate change for arid and semi-arid regions. For example, in Arizona, previously viable drinking water sources are no longer potable due to large-scale contaminant plumes containing NAPLs (Brusseau et al., 2007). Successful remediation

and recovery of contaminated aquifers depends on the detection and removal of the primary source zone and all discretely trapped contamination, which acts as secondary source zones.

Complete removal of secondary source zones depends on locating and quantifying the NAPL accurately. However, as they migrate in response to hydraulic gradients, fracture zones, capillary forces, and density profiles, NAPLs frequently become trapped in thin layers. Such traps complicate accurate characterization (Illangasekare et al., 1995; Pankow and Cherry, 1996). For instance, DNAPLs can become trapped in thin layers at permeability barriers. Examples of DNAPL traps include an aquifer/aquitard boundary or clay inhomogeneities distributed within the aquifer. LNAPLs may smear in thin zones across the top of the saturated zone in response to water table fluctuations (Bradford and Deeds, 2006). While both LNAPLs and DNAPls are biodegradable, DNAPL rates of biodegradation are so slow as to effectively nullify any temporally relevant mitigation of large-scale releases (Nellis et al., 2009). Thus remediating thin layers that act as secondary source zones is particularly imperative at DNAPL-contaminated sites.

Remediation of spilled oil in and under sea ice presents a similar case whereby thin layers of LNAPL can be dispersed in the environment for long distances in response to density contrasts and ocean currents (Stanovoy et al., 2012; Yapa and Weerasuriya, 1997). In this scenario within the Arctic environment, the presence of ice and snow, severe weather conditions, and the growth of ice sheets throughout the winter all hamper the characterization and removal of the source zone and dispersed contamination. In addition, biodegradation rates are generally proportional to temperature and thus may be even slower in these cold environments (Sydnes et al., 1985). The combination of slower

biodegradation and rapid transport mechanisms with unpredictable weather intensifies the need for timely and accurate quantification of spilled NAPL in the Arctic.

In both of these examples, the resulting thin, discrete layers of contamination cause significant uncertainty when using traditional methods to estimate NAPL quantity and location (Luciano et al., 2010). For example, conventional contaminated site work plans often implement boreholes for characterization and subsequent monitoring (USEPA, 2007). However, boreholes are expensive, time-consuming, invasive, and localized. In the Arctic, drilling boreholes through sea ice to locate spilled oil engenders significant exposure and risk to spill response personnel.

On the other hand, ground penetrating radar (GPR) has demonstrated its suitability for rapid, cost-effective, and non-invasive detection of dielectric permittivity anomalies in the subsurface in certain cases (Brewster and Annan, 1994; Bradford and Deeds, 2006; Bradford and Wu, 2007; Bradford et al., 2010; Orlando, 2002; Luciano et al., 2010). Skilled interpreters can correlate these permittivity anomalies with contaminant location by considering site characteristics and contaminant electrical properties (Bradford and Deeds, 2006; Brewster and Annan, 1994; Hwang et al., 2008). With such careful implementation, GPR can characterize a contaminated site more thoroughly and rapidly than conventional tools. However, conventional methodologies provide essential control data for such GPR site characterization.

Besides NAPL delineation, analysis of GPR data can provide additional site information relevant to remediation efforts. Examples include site stratigraphy, porosity, and current direction in the case of Arctic oil spills under sea ice (Babcock and Bradford, 2014c). At contaminated aquifers, incorporating information derived from GPR data can

reduce time for aquifer remediation using pump-and-treat, air sparging, or other technologies (Brusseau et al., 2007).

Reflection GPR methodology involves measuring the reflection of an introduced radar signal from a boundary in the subsurface and translating the measured data into information about the subsurface physical properties. The propagation of the radar signal in the subsurface and its reflection from a subsurface boundary depends on the effective subsurface permittivity (ε_{ef}) and conductivity (σ_{ef}) and the contrast in those properties across the boundary. Well-documented petrophysical transformations, such as Archie's law and the complex refractive index method (CRIM), provide the link between electrical and physical properties (Knight and Endres, 2005).

Since the electrical properties of NAPLs and NAPL-saturated earth materials can be markedly different from those of common earth materials at contaminated sites (Table 2.1), reflection GPR surveys are particularly useful for NAPL detection. However, the possible non-uniqueness in the system's material properties complicates data interpretation and subsequent identification of contaminant location (Bradford et al., 2010). Solution non-uniqueness may be particularly problematic for detecting oil in Arctic environments due to overlap between the permittivies of oil, snow, and sea ice.

If reflections from the top and bottom of a layer are well separated in time, conventional velocity analysis can yield an estimate of the speed of the radar wave propagation in that layer (Annan, 2005). Since velocity is inversely proportional to the square root of the effective permittivity, ε_{ef}, careful velocity analysis can yield an estimate of the permittivity of the layer fill and via a simple time-to-depth conversion

Table 2.1 Representative electrical properties for the NAPL contaminated sites (Bradford et al., 2010; Annan, 2005; Hinz, 2012); values for water- and DNAPL-saturated sand calculated using the complex refractive index method (CRIM) for relative permittivity (ε_r) and Archie's law for σ using m=1.3 and n=1.4 (Knight and Endres, 2005).

Material	ε_r	σ **(S/m)**	**Radar Velocity (m s^{-1} x 10^{-9})**
Air	1	0	0.3
Water	79 – 88*	0.01 - 0.5	∽0.033
Sea Water	∽88	3-5	No propagation
Sea Ice	3-8	$10^{-2} – 10^{-1}$	0.11-0.15
Snow	1.4-3.1	∽10^{-6}	0.16-0.25
DNAPLS	2 - 8	$10^{-6} – 10^{-7}$	0.1 – 0.2
Crude Oil	2 - 8	$10^{-4} – 10^{-5}$	0.15-0.21
Water-Saturated Sand	20 -30	$10^{-2} – 10^{-4}$	0.05 – 0.07
Water-Saturated Clay	5 - 40	0.1 - 1	No propagation
DNAPL Sand (85% DNAPL saturation)	5 - 8	1.9 – 9.6 x 10^{-4}	0.11 – 0.13

*Temperature-dependent

produces the layer thickness. Subsequent judicious comparison of the velocity-derived ε_{ef} to properties of known or suspected site contaminants, e.g. Table 2.1, may predict NAPL location.

However, in the case of thin layers, the reflection events from the top and bottom of the layer interfere with each other, and conventional velocity analysis is not possible (Bradford et al., 2009). We define an ultra-thin layer as one layer whose thickness is ≤⅛ the dominant wavelength (λ) of the signal (Booth et al., 2012). Below this limit, the total reflection event from the thin layer is proportional to the time derivative of the source function (Widess, 1973). However, the capability to resolve thin-layer reflection events is

influenced also by source wavelet characteristics and the presence of noise (Guha et al., 2005). Modeling results suggest that quantitative data analysis may require a thin-layer solution even at layer thicknesses up to ¾λ (Bradford and Deeds, 2006). As previously mentioned, in several relevant environmental problems spilled NAPLs tend to redistribute into thin layers. These layers may be much thinner than ¾λ, and we define thin-layers as those with thickness $\leq$ ½λ. In these cases, predicting contaminant location using conventional velocity analysis is not possible.

Attribute analysis of GPR data has proven a useful tool to estimate the electrical properties for such thin layers of NAPL contamination (Baker, 1998; Bradford and Deeds, 2006; Bradford et al., 2010; Deparis and Garambois, 2009; Orlando, 2002). These attributes include instantaneous phase, instantaneous frequency, and reflection strength (Figure 2.1). Where detection is possible, quantification of layer properties remains problematic. For example, Hwang et al. (2008) used reflection strength to quantify relative, but not absolute, DNAPL volume during a controlled spill. Bradford et al. (2010) demonstrated that reflection strength is a reliable indicator of oil trapped between snow and ice for oil thicknesses as low as 0.01 m. Nevertheless, the expected changes in reflection amplitude differed from the model prediction by 16%, making layer quantification problematic. In fact, Orlando (2002) concludes that extracting DNAPL layer thickness from reflection strength alone could be impossible.

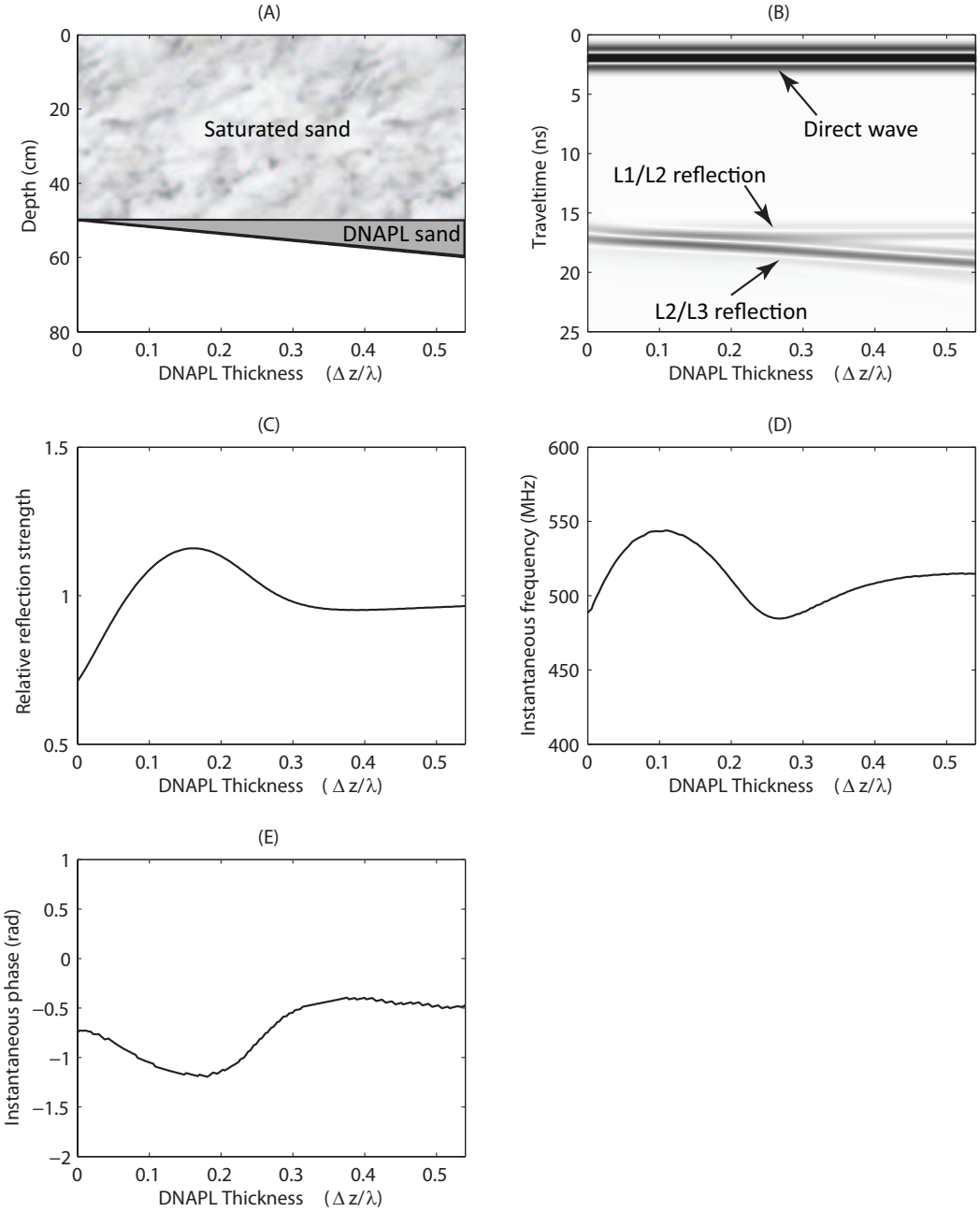

Figure 2.1: 1D reflectivity model and attribute results computed for 50 different cases of DNAPL layer thickness. a) Model with saturated sand (L1, ε_r = 29.1, brown) overlying clay (L3, ε_r = 35, white) and increasing DNAPL-saturated sand (L2, ε_r = 10.5, yellow) layer thickness from left to right; b) results from 1D reflectivity model; and extracted c) reflection strength, d) instantaneous frequency, and e) instantaneous phase. Full-waveform inversion can incorporate all of this information and best constrain the solution for thin-layer properties.

Instantaneous phase and frequency are also useful in thin-layer problems but have limitations (Taner et al., 1979). For example, Orlando (2002) found that changes in instantaneous phase and frequency delineated of a zone of DNAPL contamination, but was unable to quantify layer thickness. Bradford et al. (2010) extracted instantaneous phase within 6% of the model predication for thin-layers of LNAPL trapped between snow and ice. However, both the instantaneous phase and frequency in their research varied widely due to noise, and their results for instantaneous phase had a coefficient of variation (*cv*) greater than 150%. The high *cv* reflects the uncertainty of correlating instantaneous phase with thin-layer parameters and highlights the difficulty of attribute analysis for thin-layer quantification using GPR data.

On the other hand, full-waveform inversion allows practitioners to directly invert for subsurface properties (Plessix et al., 2012). Full-waveform inversions incorporate all the information contained in the reflected wavelet in the effort to directly quantify subsurface parameters. Thus, this methodology can be more robust than attribute analysis, which singles out specific pieces of information such as the attributes mentioned above (Figure 2.1).

Previous work has used full-waveform inversion on GPR reflection data to estimate subsurface electrical parameters (Kalogeropoulos et al., 2013; Lambot et al., 2004; Tran et al., 2012). Busch et al. (2012) implemented a full-waveform inversion to recover ε_{ef} and σ_{ef} within 15% and 62% respectively of measured data. Kalogeropoulos et al. (2013) inverted GPR reflection data for ε_{ef} and conductivity gradients within concrete due to chlorine infiltration. They retrieved the uppermost concrete ε_{ef} within 1% of the true value using the air/concrete reflection. Tran et al. (2012) use full-waveform

inversion combined with a mixing model to estimate water content and sand thickness for a sandy soil. Their solutions for water content erred by less than 1.3%. Sand thickness results were within 5% of true values. In many cases, correct parameterization of the source wavelet has proven crucial for reliable inversion results (Klotzsche et al., 2010; Busch et al., 2012).

Previous research has also implied that full-waveform inversion on GPR data may also be a promising tool for thin-layer quantification. For example, Deparis and Garambois (2009) inverted for the AVO characteristics of reflection GPR data with respect to frequency. They concluded that a global inversion scheme may allow for improved thin-layer characterization. Zeng et al. (2000) qualitatively correlated model AVO curves with field GPR data, and predicted that full-waveform inversion of GPR data may allow for quantitative analysis of thin layers. With these advantages in mind, here we present a targeted full-waveform inversion algorithm for quantifying thin ($\leq \frac{1}{2}\lambda$) and ultra-thin- ($\leq \frac{1}{8}\lambda$) layer properties using GPR reflection data.

Methodology

Forward Model

We use a 1D, vertical-incidence reflectivity method to generate our forward model. The reflectivity method provides an exact solution to the wave equation for an electromagnetic (EM) plane wave propagating through a homogeneous, isotropic, 1D layered material.

Petrophysics

Thus we begin by calculating or estimating σ_{ef} and ε_{ef}. These properties are frequency-dependent and given as follows, assuming that the imaginary part of the complex-valued σ is insignificant (Knight and Endres, 2005):

$$\sigma_{ef}(\omega) = \sigma_{dc} + \omega\varepsilon''(\omega) \quad (2.1)$$

and

$$\varepsilon_{ef}(\omega) = \varepsilon'(\omega) \quad (2.2)$$

where $\sigma_{dc}$is the low frequency conductivity limit; ε'' is the imaginary part of the complex-valued permittivity, ε; ε' is the real part of ε; and ω is frequency (Knight and Endres, 2005).

Values for σ_{dc} of common earth materials are well-known, and we can use reasonable representative values from the literature or measured values in equation 2.1 (Annan, 2005; Knight and Endres, 2005; and others). Additionally, for a saturated porous material the modified Archie's law provides an empirical approximation for σ_{dc} as function of the cementation factor (m), the conductivity of the pore fluid (σ_f), and the water saturation (S_w):

$$\sigma_{dc} = \sigma_f \phi^m S_w^n \quad (2.3)$$

Literature values for m range from 1.5 to 2.5, and for n range from 1 to 2 (Knight and Endres, 2005; Archie, 1942).

Next, we must calculate the complex-valued permittivity and substitute $\varepsilon''(\omega)$ into equation 2.1. In this paper, we use the CRIM equation to estimate ε^* of a mixture as follows (Knight and Endres, 2005):

$$\varepsilon^* = [(1-\phi)\sqrt{\varepsilon_s} + \phi S_w \sqrt{\varepsilon_w^*} + \phi(1-S_w)\sqrt{\varepsilon_3}]^2 \quad (2.4)$$

where ε_w is the complex, frequency-dependent permittivity of water; φ is the porosity of the mixture; S_w is the percent saturation; ε_s is the permittivity of the soil grains; and ε_3 is the permittivity of a third phase, if present.

The complex-valued frequency-dependent permittivity for water, ε_w^*, is given by the Debye equation (Debye, 1929). It describes the dielectric molecular relaxation of water at a specific ω:

$$\varepsilon_w^* = \varepsilon_\infty + \frac{\varepsilon_{dc} - \varepsilon_\infty}{1 + i\omega\tau} \quad (2.5)$$

where $\varepsilon_\infty$is the permittivity limit at frequencies much higher than the characteristic relaxation frequency of water, about 17 GHz; ε_{dc} is the low frequency permittivity limit; and τ is the characteristic relaxation time.

Thus, we can calculate the relevant material properties in each layer of our reflectivity model. Combining equations 2.3, 2.4, and 2.5 produces σ_{ef}. Substituting equation 2.4 into equation 2.2 provides ε_{ef}. Combining σ_{ef} and ε_{ef} gives the wave number (k) in a given material as follows:

$$k^{*2} = \mu_0 \varepsilon_{ef} \omega^2 - i\omega\mu_0\sigma_{ef} \quad (2.6)$$

where $\mu_0$is the magnetic susceptibility of free space.

Algorithm

We use the model to simulate the reflectivity response to a series of stacked layers. The 1D reflectivity calculation begins at the lowermost layer and then calculates the total reflectivity response, MB_i, recursively at each successively higher boundary using the Fresnel reflection (R) and transmission (T) coefficients and MT_i as follows:

$$\mathrm{MT_i} = \mathrm{MB_i} e^{-2\mathrm{i}k_i^* d_i} \tag{2.7}$$

$$\mathrm{MB_i} = \frac{\mathrm{R_{i+1}^d} + \mathrm{T_{i+1}^d T_{i+1}^u MT_{i+1}}}{1 - \mathrm{R_{i+1}^u MT_{i+1}}} \tag{2.8}$$

The recursive algorithm uses those relationships to compute reflectivity from the total stack, which we observe at the uppermost boundary, R_1 (Muller, 1985):

$$R_1 = MB_0 \tag{2.9}$$

where d is the layer thickness. The superscripts u and d refer to the up-going and down-going reflection and transmission coefficients, respectively, at a boundary.

The model then convolves R_1 with a source wavelet spectrum in the frequency domain. We use a Gabor wavelet (G) as it provides a source spectrum which closely models the source wavelet of our commercial radar system while allowing for flexibility in reproducing a range of source wavelets (Morlet et al., 1982). These wavelets are the product of a Gaussian window with a sine function. G is defined in the frequency domain as follows:

$$G = \frac{1}{\sqrt{2p}} e^{-\frac{2\pi(f-f_0)^2}{4p}} e^{-i\eta} \tag{2.10}$$

where f_0 is central source frequency (Hz), η is phase rotation, and p is a function of the width of the Gabor function, δ_0 (s):

$$p = \frac{1}{2\delta_0^2} \tag{2.11}$$

After convolution, we transform the result to the time domain using the inverse Fourier transform to generate a complex-valued wavelet *W*. This result simulates a radar reflection event from the layer stack. It provides the full analytical 1D solution including all multiples.

Inversion

The inversion evaluates the cost function, ϕ, as follows:

$$\varphi = \sum(d_{obs} - d_{calc})^2 \tag{2.12}$$

where d_{calc} is a reflected wavelet calculated using the 1D reflectivity model, and d_{obs} is the data. In taking this approach, we assume a 1D response is an adequate representation of the radar data. Furthermore, based on the derivation of the 1D reflectivity model, we are assuming the electrical properties of the layers are homogenous and isotropic.

The inversion uses a Nelder-Mead gradient-based simplex search method to find the values of those user-chosen inversion parameters which minimize ϕ (Lagarias et al., 1998). The total set of inversion parameters within the reflectivity model are the source wavelet parameters (f_0, δ_0, and η) and all layer properties (ε_{ef}, σ_{ef} , and d). Thus for the 3-layer case there are a total of 12 available parameters. We can choose to invert for the values of any subset of those parameters, and we define that subset as the inversion parameters. In general, we may choose to include an arbitrary number of layers, but all models in this paper have 3 layers.

Typically, we seek a solution for the thin-layer parameters while assuming that the upper and lower layer properties are well-known. With that assumption, we first

invert for the source parameters. Then we can use the resulting source wavelet parameters within the inversion to solve for the thin-layer properties ε_{ef}, d, and σ_{ef}. In most cases, the thickness of the overburden, ℓ, is an additional inversion parameter. Inverting for the effective source function allows us to include propagation effects due to the overburden in our source wavelet characterization. The model may not directly include such effects. Thus, this method provides the most complete estimate of effective source properties.

While inverting for either thin-layer or source parameters, we take a Monte-Carlo approach to initialize the starting values for each inversion parameter. We randomly select the initial value for each parameter from a uniform distribution that bounds the range that is physically realistic for each case. The inversion continues the gradient-based search to minimize ϕ using the specified inversion parameters until reaching a user-specified minimum value for ϕ or a user-specified maximum number of function evaluations. The algorithm then returns the thin-layer parameters and ℓ which correspond to that local minimum value (ϕ_{LM}). For all inversion testing, the complete inversion routine replicates 1000 times and finds the global minimum (ϕ_{GM}) from those 1000 iterations. We report the mean of the inversion parameters from the subset of solutions which correspond to ϕ_{GM}.

To estimate uncertainty, we evaluate equation 2.11 for 10,000 parameter pairs around the solution mean. We then calculate the root mean square (RMS) error and estimate the range of parameter pairs that fit the data within an estimated noise level. For the source parameters, we test the coupled uncertainty for f_0, δ pairs and for f_0, η pairs. For the thin-layer problems, we report uncertainty from ε_r, d pairs and from ε_r, σ pairs. Although additional exploration of the solution space is necessary to fully constrain the

coupled, multi-dimensional uncertainties, this approach gives a good idea of solution uncertainty while remaining easy to visualize.

In summary, steps for implementation of this algorithm are as follows:

- Estimate/define layer properties for contaminated and uncontaminated case
- Estimate/define source properties
- Invert for effective source wavelet parameters using uncontaminated reflection event
- Define inversion parameters (subset of all layer parameters, usually contaminated layer properties) and invert for those parameters using effective source function in 1D reflectivity model
- Estimate uncertainties from parameter pairs

Testing

In order to test the inversion, we first calculate 3 forward models. We use 3 different source frequencies to test inversion robustness and add 5% random Gaussian noise to each of the models before the inversion. Each model has up to 3 layers each (Table 2.2). Relative change in permittivity from layer 1 to layer 3 is low/medium/high, high/low/high, and low/high/low for Models 1, 2, and 3, respectively. These models simulate oil overlying salt water, a DNAPL trapped a sand/clay interface, and dry sand overlying saturated sand trapped above bedrock. We also generate 3 corresponding secondary 2-layer models representing a reflection from an uncontaminated Layer 1/Layer 3 boundary with Layer 1 and Layer 3 properties as listed for the primary model in Table 2.2. We use these models to invert for the source wavelet parameters. Thus, for

the source parameters inversions, f_0, δ_0, and η were the inversion parameters. For the thin layer inversions, ε_r, d, σ, and the thickness of the overburden (ℓ) are the inversion parameters. We estimate uncertainties from the range of coupled parameter pairs that fit the data within 5% of ϕ_{GM}.

Models

Model 1 simulates an oil layer overlying sea water with 1 m of air between the antennas and the oil layer (Table 2.2). The model replicates a radar trace collected with the antennas suspended in air over oil spilled in ocean water. We use representative values for ε_r and σ_{ef} of air, oil, and salt water, where ε_r equals ε_{ef} divided by the permittivity of free space, ε_0. For this model, we generate 2 separate examples having oil layer thicknesses equal to 10%λ and 25%λ respectively. The central source frequency (f_0) is 1500 MHz, and η=0. The secondary model for the source inversion testing on Model 1 simulates air over salt water.

The second model simulates a DNAPL contaminant trapped at a sand/clay impermeability barrier. DNAPLs can become trapped in this way at the bottom of an aquifer or at isolated clay lenses within the aquifer. We use equations 2.4 and 2.5 to calculate the ε_{ef} for the saturated sand (layer 1) assuming φ=37% and $\varepsilon_s=4\varepsilon_0$ for quartz. For the properties of water (equation 2.5), we set $\varepsilon_\infty = 1.8\varepsilon_0$, $\varepsilon_{dc} = 81\varepsilon_0$, and τ = 9.3 x 10^{-12} s (Cole and Cole, 1941). To calculate ε_{ef} for the DNAPL-saturated sand (layer 2), we assume that the DNAPL displaces 85% of the pore water (S_w=15%), and that $\varepsilon_3 = 2\varepsilon_0$ for the DNAPL (Hinz, 2012). Finally, substituting $\varepsilon''(\omega)$ from equation 2.4 and representative values for σ_{dc} into equation 2.1 yields σ_{ef} in layers 1 and 2. We use

equation 2.3 to calculate σ_{dc} using m = 2, n = 1, and σ_f = 1 x 10^{-2} S/m and representative values from the literature for clay ε_{ef} and σ_{ef} (Knight and Endres, 2005). The DNAPL layer thickness in this model is 9%λ; f_0 is 500 MHz; and η=0 (Table 2.2). The secondary model for the source inversion testing on Model 2 simulates a reflection from the sand/clay barrier.

The final model simulates a thin layer of saturated sand underlying the vadose zone and overlying bedrock. We calculate ε_{ef} for the saturated sand following the methodology for Model 2. However, we set σ_{ef} = 0.01 S/m for the thin layer in order to test the inversion at higher values of conductivity. Electrical properties for layers 1 and 3 are based on representative values from the literature for dry sand and granite (Knight and Endres, 2005). The thin-layer thickness for Model 3 is 8%λ. Central source frequency is 1000 MHz, and η=0. The secondary model for the source inversion testing on this model simulates a reflection from the sand/granite interface.

Table 2.2: Model parameters: Model 1 simulates an oil layer overlying sea water; Model 2 represents a DNAPL trapped at a saturated sand/clay interface; and Model 3 describes an overland flow model with a saturated sand layer underneath a dry sand overlying bedrock. We estimated or calculated parameters as described in the text; *d* is also given as %λ. Note that we generated Model 1 for 2 layer thicknesses.

Model	Layer #	ε_r	σ_{ef} (S/m)	*d* (m)
1	1, air	1	0	1
f_0=1500 MHz	2, oil	3.5	5.3×10^{-4}	a) 0.01 (10%λ) b) 0.025 (25%λ)
δ_0 = 0.3 ns	3, salt water	81	1	1
2	1, saturated sand	22	0.004	0.039
f_0=500 MHz	2, DNAPL- sand	7	9.6×10^{-4}	0.02 (9%λ)
δ_0 = 0.9 ns	3, clay	35	0.1	1
3	1, dry sand	4	10^{-4}	1
f_0=1000 MHz	2, saturated sand	22	0.01	0.005 (8%λ)
δ_0 = 0.9 ns	3, granite	5	10^{-5}	1

Inversion Results

Source Inversion

For all models, the inversion recovers the source parameters within <1% of the true values for f_0 and δ_0 (Figure 2.2 and Table 2.3). The values for η are small ($<4 \times 10^{-3}$) positive numbers in all three tests, but the true value of η is 0. Uncertainties for the inversion results for f_0 and δ_0 are <10% of solution values (Table 2.3). However, the *cv* associated with the solution η is up to 25%.

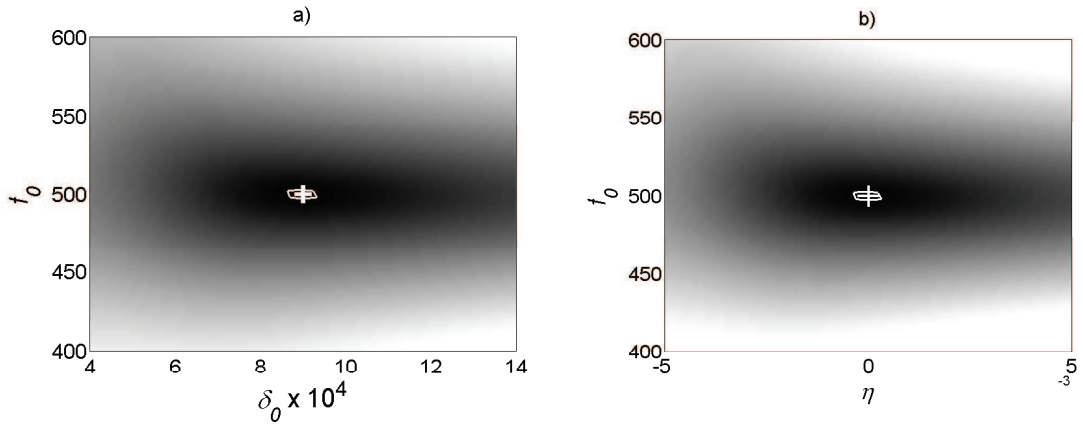

Figure 2.2: a) Paired f_0, δ_0 uncertainties and b) paired f_0, η uncertainties for the solutions from the source parameter inversion for Model 2; darker indicates lower values. The + is the true model value and the line encloses all paired values where the objective function is within 5% of ϕ_{GM}, which is the level of added Gaussian noise in the models. Although we only include the plots for the inversion solution for Model 2, the results from Models 1 and 3 are similar and are enumerated in Table 2.3.

Table 2.3: Inversion solution and standard deviation for source wavelet parameters using reflection from Layer 1/Layer 3 in an uncontaminated area for models; true η = 0 for all model source functions.

Model	Convergence Rate	f_0 (true value) (MHz)	f_0 (solution) (MHz)	δ_0 (true value) (ns)	δ_0 x 10^{-4} (solution) (ns)	η (x 10^{-3})
1	24%	1500	1499 ± 3	0.3	0.30 ± 0.03	3.4 ± 0.2
2	43%	500	499 ± 3	0.9	0.90 ± 0.03	1.1 ± 0.2
3	57%	1000	1000 ± 4	0.9	0.89 ± 0.04	1.2 ± 0.3

Model 1

For Model 1, the rate of convergence is 2%. (We define the rate of convergence as the percentage at which the inversion algorithm converges to ϕ_{GM} out of the 1000 iterations. Convergence to ϕ_{GM} is constrained to starting values for layer depth from the surface (ℓ) being within 50% of the true value (Table 2.4). The mean inversion solution is

within 8% and 14% of the true values for the oil layer ε_r and d, respectively (Table 2.4). The solution for ℓ is within 1% of the true value. However, the σ solution deviates up 66% from the true model value. The inversion algorithm does not appear to be sensitive to the thin-layer conductivity for this example.

The solution ε_r and d are 6% and 13% more accurate for the thin oil layer (Model 1b, $d = 25\%\lambda$) than for the ultra-thin one (Model 1a, $d = 10\%\lambda$), and the associated uncertainties are 90% smaller (Figure 2.3). In addition, the difference between ϕ_{GM} and the next lowest ϕ_{LM} is 3 times larger for the thin-layer case ($\phi_{GM} \cong 27\%\phi_{LMnearest}$) than for the ultra-thin layer example ($\phi_{GM} \cong 96\%\phi_{LMnearest}$) (Figure 2.4). Thus overall results for Model 1 suggest that the inversion accuracy may increase as layer thickness increases, if all other parameters were to remain constant.

Model 2

The rate of convergence to ϕ_{GM} is 20%, and ϕ_{GM} is 75% greater than the next lowest ϕ_{LM}. The inversion on Model 2 data retrieved the ultra-thin-layer parameters within 2% of the true values for ε_r, d, and ℓ (Table 2.4). The paired ε_r, d uncertainties are ±15% of the true values (Figure 2.3). The accuracy of these results is promising given the thinness of the DNAPL layer ($9\%\lambda$) as compared with Model 1 oil layer thinness ($25\%\lambda$ and $10\%\lambda$). The conductivity solution deviates up 80% from the true layer σ.

Model 3

The rate of convergence to ϕ_{GM} is 11% for this model, and ϕ_{GM} is 18% of the next lowest ϕ_{LM}. Examining the starting range for thin-layer parameters (Table 2.4) reveals that convergence to ϕ_{GM} again is limited to the randomly chosen starting value for ℓ being

within 50% of the true value. (In field data, the overburden thickness will likely be constrained within ±5% of the true values, but here we allowed deviations up to 100% from true overburden thickness in order to test model robustness.)

The inversion solution for the thin-layer parameters is within 4% of the true ε_r and d, and within 1% of the true ℓ (Table 2.4). The paired ε_r, d uncertainties are within ±25% of the true values (Figure 2.3). Here we purposely tested a thin-layer σ 2 orders of magnitude higher than either Model 1 or Model 2. In this case, the resulting solution for σ is 5 orders of magnitude lower than the true layer σ.

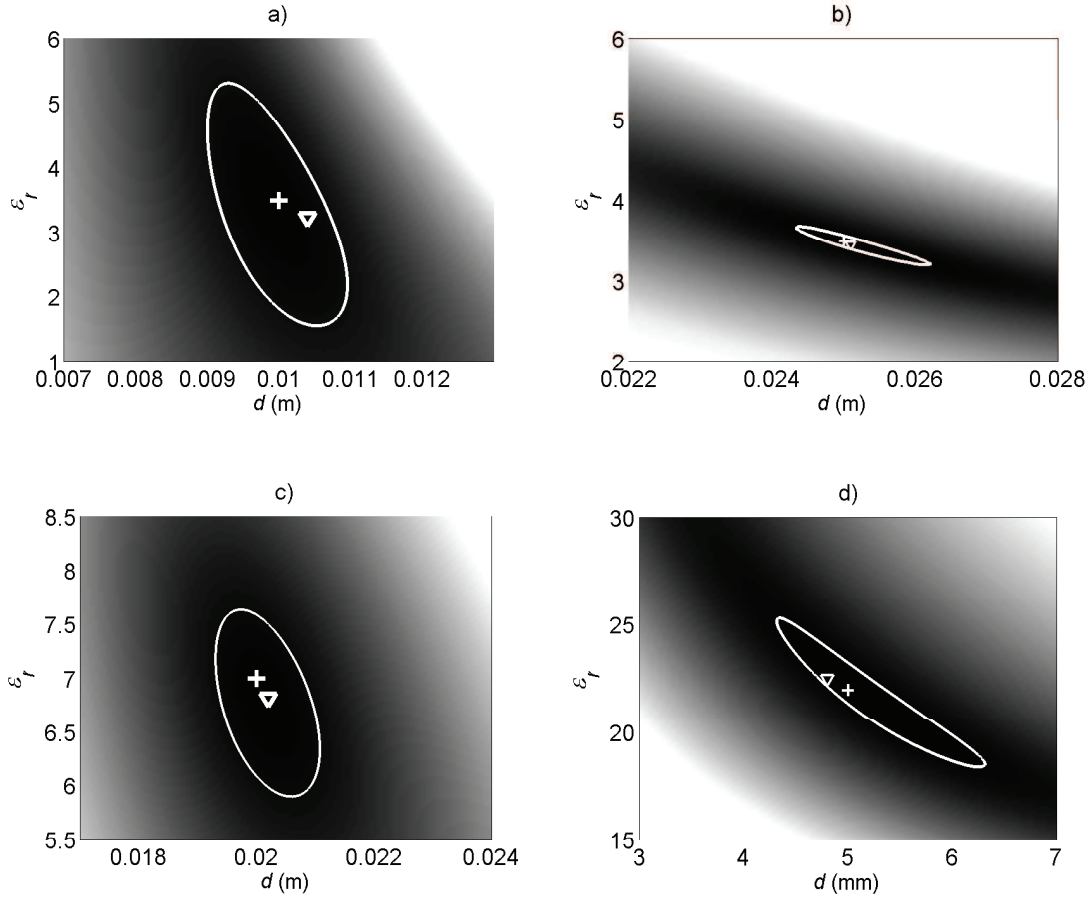

Figure 2.3: Uncertainties calculated for ε_r, d pairs centered around the inversion solution for a) Model 1a, b) Model 1b, c) Model 2, and d) Model 3; blue colors are low. The + is the exact model value, the triangle is the inversion solution, and the

line encloses all paired values where the objective function is within 5% of ϕ_{GM}. Uncertainties in solutions for σ and l are the range of values enclosed by the line for these parameters for coupled ε_r, σ pairs and ε_r, l pairs respectively (not pictured here, values in Table 2.4).

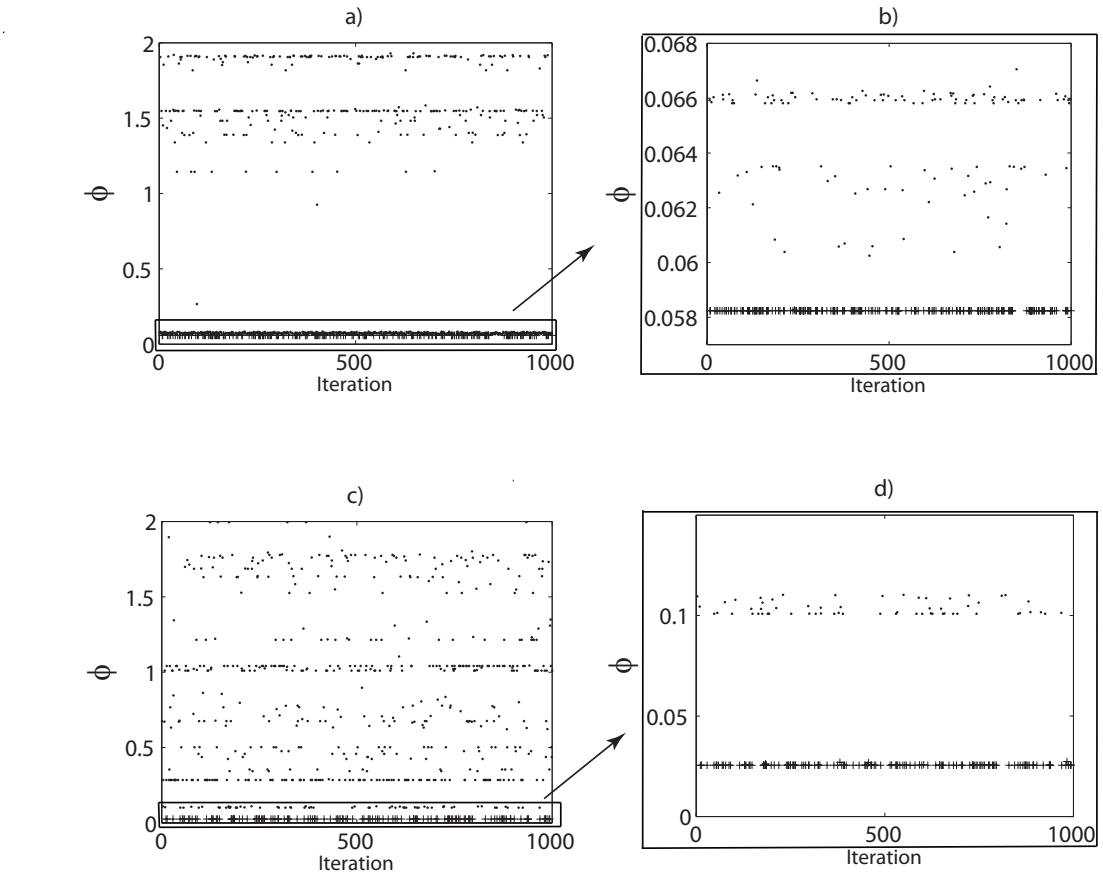

Figure 2.4: Comparison of the difference between ϕ_{GM} (+) and ϕ_{LM} (.) from the 1000 inversion iterations for a) Model 1a and b) Model 2. For Model 2, $\phi_{GM} \cong 25\% \phi_{LMnearest}$, while for Model 1a, $\phi_{GM} \cong 96\% \phi_{LMnearest}$. A larger difference between the two may indicate a more reliable solution.

Table 2.4: Ultra-thin-layer parameters for a) Model 1, b) Model 2, and c) Model 3 and the inversion mean calculated from all results for ϕ_{GM}. Uncertainties for ε_r , d pairs are in Figure 2.3.

a) $\phi_{GM(a)}$=96%$\phi_{LM(a)nearest}$ and $\phi_{GM(b)}$=27%$\phi_{LM(b)nearest}$

Parameter	True Value	Solution	Bounds	Starting Range	Range Leading to ϕ_{GM}
ε_{ef}	3.5	a) 3.24 b) 3.45	1 - 50	2 - 15	2-15 2.39 - 14.94
d (m)	a) 0.01 b) 0.025	a) 0.01 b) 0.025	0 – 1	0.001 - 0.15	0.001-0.15 0.0011 - 0.107
l (m)	1	0.99 ± 0.01 1.001 ± 0.001	0 – 10	0.2 - 2	0.51-1.49 0.56 - 1.49
σ (S/m)	5.3 x 10^{-4}	3.8 ± 3.1 x 10^{-4} 1.8 ± 1.3 x 10^{-4}	0 – 0.1	1 - 25 x 10^{-4}	1.13 – 8.96 x 10^{-4}

b) ϕ_{GM}=25%$\phi_{LMnearest}$

Parameter	True Values	Solution	Bounds	Starting Range	Range Leading to ϕ_{GM}
ε_{ef}	7	6.9	1-40	2 - 15	2.02 - 15
d (m)	0.02	0.02	0-1	0.001 - 0.15	0.01 - 0.145
l (m)	0.40	0.399 ± 0.002	0-10	0.2 - 1.0	0.2 - 0.69
σ (S/m)	9.6 x 10^{-4}	1.8 ± 1.6 x 10^{-4}	0 - 0.1	1 - 25 x 10^{-4}	1 x 10^{-4} – 2.4 x 10^{-3}

c) ϕ_{GM}=18%$\phi_{LMnearest}$

Parameter	True Values	Solution	Bounds	Starting Range	Range Leading to ϕ_{GM}
ε_{ef}	22	22.51	1-40	15 - 30	15 – 29.9
d (m)	0.005	0.0048	0-1	0.001 – 0.05	0.001 - 0.0048
l (m)	1	1.007 ± 0.005	0-10	0.1 - 2	0.57 – 1.42
σ (S/m)	0.01	8.2 ± 3.5 x 10^{-7}	0 - 1	0.005- 0.05	5 x 10^{-3} – 5 x 10^{-2}

Parameter Sensitivity Testing

First we test the robustness of the source parameter inversion to errors in overburden permittivity for Models 2 and 3. For each model, we inverted for the source wavelet parameters 20 separate times. For each separate inversion, the model overburden permittivity (ε_1) deviated from the true permittivity while the rest of the inversion routine remained constant. We tested the source parameter inversions for deviations in ε_1 ±20% in increments of 2%. For both Model 2 and Model 3, the solution f_0 was within 5% of the true value even when ε_1 varied ±20% from the true value. The same is true of the solution δ_0 for Model 2. However, in Model 3, the solution for δ_0 deviated up to 135% from the true value as ε_1 increased above +10% of the true value. In addition, the solution η for both models deviated from the true value. Over the range of deviations from true ε_1 tested, the change in phase Model 3 was 1 order of magnitude greater than that for Model 2. The discrepancy in the solution deviations between the two models may be due to the fact that the Model 3 overburden was 2.2 times as thick as in Model 2. The greater the propagation distance through the overburden with a fixed conductivity, the greater the apparent change in phase of the wavelet. Thus, as the overburden thickness increases, any errors in overburden characterization have a greater effect on the inversion solution for the source parameters.

After testing the inversion robustness for overburden permittivity estimation errors, next we systematically test the inversion for conductivity only using Model 3. We generate 9 different models based on Model 3 with the other parameters listed in Table 2.2 held constant. Each model has a different σ starting from Model 3_1 having $\sigma = 10^{-0.5}$ S/m to Model 3_7 having $\sigma = 10^{-7}$ S/m. In this inversion, we hold all other model

parameters constant and allow σ to be the sole inversion parameter. The inversion solutions were within 10% of the true value for the models with the 4 highest σ values (10^{-2}, $10^{-1.5}$, 10^{-1}, and $10^{-0.5}$ S/m), but for the other 5 tests the solutions for σ vary more than 5 orders of magnitude from the true value. The associated uncertainties encompass roughly the same set of values for all σ except the two highest values tested (Figure 2.5). Furthermore, the inversion solutions for $\sigma_{true}= 10^{-4}$ S/m and for $\sigma_{true}= 10^{-5}$ S/m were within 12% of the solution given when $\sigma_{true}= 10^{-2}$ S/m. We conclude that there are no discernible trends in the inversion solution accuracy over the range of σ values from 10^{-7} to $10^{-1.5}$ S/m. For the 2 highest conductivities tested, the solution is reasonable and the error is confined to 1 order of magnitude. Reliably estimating σ and its uncertainty may only be possible when layer $\sigma > 10^{-1.5}$ S/m. However, the limit for σ estimation most likely also depends on f_0 as well as the layer thickness (Tsoflias and Becker, 2008). Here we have tested σ sensitivity using an ultra-thin layer model, and it may be possible that sensitivity will increase with increasing layer thickness.

Finally, we test the inversion sensitivity to layer thickness using variations on Model 2. With the other parameters in Model 2 constant (Table 2.2), we test the following values of DNAPL-layer thicknesses: d = 0.02 m (9%λ); d = 0.015 m (7%λ); d = 0.01 m (4%λ); d = 0.005 m (2%λ); d = 0.002 m (0.9%λ); and d = 0.001 m (0.4%λ). In this case, we hold all other parameters constant and allow d to be the sole inversion parameter. The inversion algorithm demonstrated a remarkable accuracy (within 5%) in retrieving ultra-thin-layer thicknesses that were much less than 10%λ, including two tests where d <1%λ (Figure 2.5). This result demonstrates that reflection radar data is sensitive to extremely thin-layers (<1%λ).

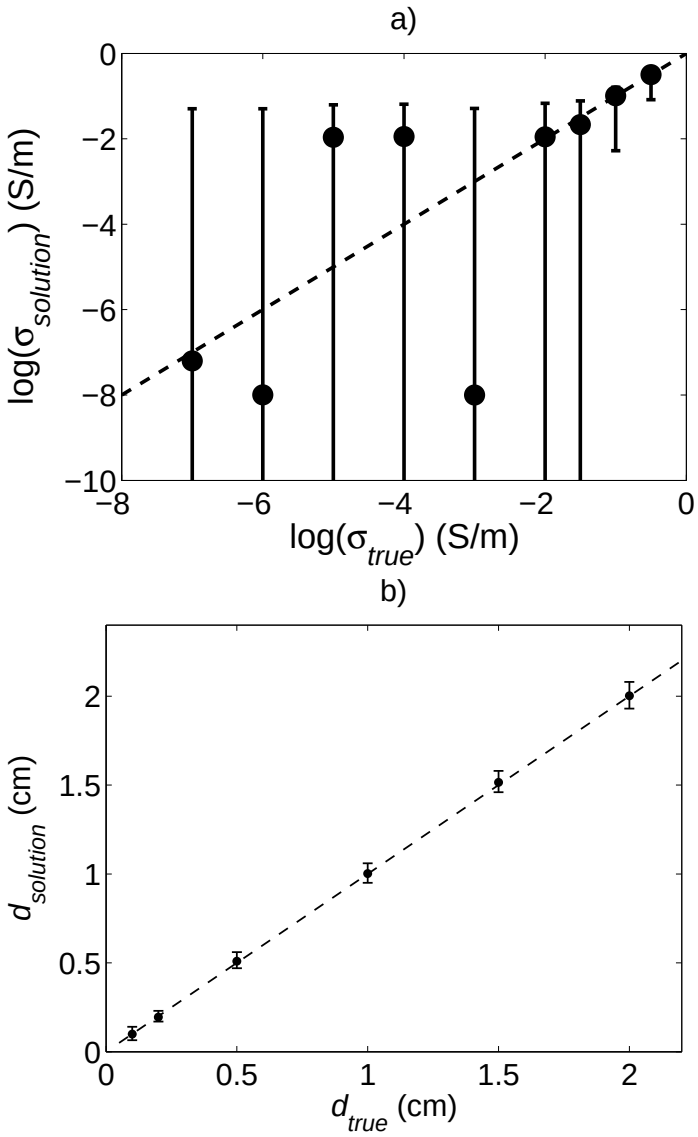

Figure 2.5: Sensitivity testing for a) σ using Model 3 and b) d using Model 2, where $\cdot$ is the inversion solution, and the dashed line marks 1:1 correlation. Note scales. Error bars are those solutions within 5% of ϕ_{GM}. The inversion does not appear to be sensitivity to σ, which corroborates our observations throughout model testing. On the other hand, the inversion retrieves layer thicknesses accurately (within 5% of the true model value) down to a layer thickness of 0.4%λ.

Conclusions

The full-waveform inversion performs robustly for 4 different models. The inversion recovers thin-layer ε_r within 8%, d within 14%, and ℓ within 2% of the true

values for all models, but is insensitive to low σ values. The inversion performed well for layer thickness well less than ⅛λ. Accurate overburden characterization will aid the inversion's rates of convergence by tightening the range for initial values of ℓ. Our results demonstrate the importance of accurate overburden characterization as conversion to the true solution depends on the starting estimate for overburden thickness being within 50% of true value. GPR site characterization can provide these parameters using velocity analysis or other methods such as Time Domain Reflectometry (TDR) before implementing the full-waveform inversion for quantification of thin-layer parameters. Careful analysis of the overburden should allow users to determine overburden permittivity, and thus thin-layer depth, within 5% of its true value (Bradford et al., 2009).

We demonstrated a positive correlation between solution accuracy and increasing differences between ϕ_{GM} and ϕ_{LM}. Thus comparing the two may provide an indication of solution reliability, in that a larger difference (>70%) between them may signify a more accurate result (Figure 2.4). Finally, convergence rates are as low as 2% (Model 1) and less than 20% in all model examples, confirming the requirement to perform multiple iterations in order to generate reliable results. Our protocol calls for 1000 iterations per inversion. This protocol gives good results for these models.

Although it performs well for all other layer parameters, the inversion is not sensitive to conductivity values. During specific testing for solution σ, solution σ deviated up to 5 orders of magnitude from true or estimated values at low σ values. Examination of the wave number reveals that wave attenuation depends on σ_{ef} whilst the wave propagation depends on ε_{ef}. Therefore, changes in ε_{ef} dominate the reflectivity response at low σ values (Zeng et al., 2000). Thus, although the 1D reflectivity model computes

d_{calc} based on the full, frequency-dependent wave number calculation, the impact of σ_{ef} is much less than that of ε_{ef} on the objective function. Therefore, the insensitivity of the inversion to the thin-layer conductivity follows from the nature of the reflectivity model used to calculate the objective function.

Overall, the accuracy of our inversion algorithm for recovering thin- and ultra-thin-layer parameters other than σ using GPR reflectivity data demonstrates its potential usefulness for quantitatively characterizing thin-layer parameters. Our inversion may provide reliable estimates of layer thickness well below the conventional thin-layer resolution limits, and even at layer thicknesses below 1%λ as demonstrated during model testing. Since we use an effective source function inversion, the inversion is well-suited for application to targeted time-lapse monitoring of contaminated sites. Future work includes testing the inversion on field data from contaminated sites. If successful, site managers could implement this inversion to estimate total contamination at a site and to prioritize remediation efforts based on NAPL concentrations and thicknesses. Due to the ubiquitous nature of these classes of contaminants, careful implementation of this algorithm could greatly reduce remediation costs and time. Finally, the accuracy of the inversion performance for the third model suggests that this full-waveform algorithm may be applied to other thin-layer problems such as snowmelt monitoring or fracture characterization.

CHAPTER THREE: TARGETED FULL-WAVEFORM INVERSION OF GROUND-PENETRATING RADAR REFLECTION DATA FOR THIN AND ULTRA-THIN LAYERS OF NON-AQUEOUS PHASE LIQUID CONTAMINANTS PART 2: DATA TESTING

Abstract

Accurately quantifying thin-layer parameters by applying full-waveform inversion methodology to GPR reflection data may provide a useful tool for near-surface investigation. Such quantification would be particularly useful for contaminated site investigation where non-aqueous phase liquid (NAPL) contaminants are present. We test a full-waveform inversion algorithm on 4 GPR reflection data sets in an attempt to quantify thin-layer permittivity (ε), thickness (d), and conductivity (σ) for thin ($\leq$½ dominant wavelength λ) and ultra-thin ($\leq$⅛λ) layers using GPR reflection data. The data examples include 3 different contaminants: 1) oil overlying cold salt water, 2) dense NAPL (DNAPL) trapped at a sand/clay interface, 3) light NAPL (LNAPL) accumulated at the top of the saturated zone, and 4) oil overlying sea ice covered by a thin layer of snow. We collected the first two data sets in a laboratory, while the latter two are from field sites. The inversion initializes starting values with a Monte-Carlo scheme and finds the global minimum of the objective function using a non-linear grid search. In all 4 examples, the inversion solved for NAPL-layer properties within 15% of the measured values. The inversion successfully quantified thin-layer properties for 2 different source frequencies and 4 different subsurface conditions relevant to the investigation and

remediation of contaminated sites. This algorithm provides a tool for site managers to prioritize remediation efforts based on quantitative assessments of contaminant quantity and location using GPR.

Introduction

Subsurface accumulation of non-aqueous phase liquid contaminants (NAPLs) can degrade soil and groundwater resources and pose a significant risk to human health (Hwang et al., 2008). These classes of contaminants falls into two categories based on density: light NAPLs (LNAPLs) are less dense than water and thus rise to the top of a water column while dense NAPLs (DNAPLs) sink (Carcione et al., 2003; Luciano et al., 2010). Many NAPL-contaminated sites are the result of improper disposal of used solvents or fuels (Brusseau et al., 2011; Nellis et al., 2009). Over time, these NAPLs can migrate vertically and horizontally for long distances in the subsurface. LNAPLs can smear across the vadose zone/saturated zone interface due to fluctuations in the water table (Bradford and Deeds, 2006). DNAPLs can become trapped at impermeability barriers as they simultaneously migrate downward and laterally in response to dominant groundwater gradients.

In both scenarios, the result is the same: NAPLs often disperse into thin layers. These thin, discrete layers of contamination pose a problem for traditional methods of detection such as borehole sampling (Illangasekare et al., 1995; Pankow and Cherry, 1996). However, ground penetrating radar (GPR) has proven a useful tool for characterizing contaminated sites in a rapid and cost-effective manner (Brewster and Annan, 1994; Bradford and Deeds, 2006; Bradford and Wu, 2007; Orlando, 2002; Luciano et al., 2010). Careful assessment of GPR reflection data can allow practitioners

to identify zones of anomalous subsurface permittivity and correlate these anomalies with the presence of subsurface contamination (Carcione et al., 2003).

However, when NAPLs disperse into thin layers, the problem of reliably detecting and quantifying the contamination becomes more difficult. Here we define thin layers as those layers where recorded reflection events from the top and bottom of the layer are not well-separated in time (Widess, 1973). Depending on source characteristics, noise, and other factors, this limiting layer thickness may be as high as ¾ the dominant wavelength of the signal, λ (Bradford and Deeds, 2006; Guha et al., 2005). Following Babcock and Bradford (2014a), we take thin layers to be those whose thickness is $\leq$½λ and ultra-thin layers those whose thickness is $\leq$⅛λ. In such cases, measuring layer thickness (d) or effective permittivity (ε_{ef}) using conventional velocity analysis is impossible, and we must turn to other techniques if we seek to quantify thin-layer parameters (Bradford et al., 2009).

Full-waveform inversion may provide such a tool to quantify contaminated sites by directly inverting for the properties of subsurface layers (Babcock and Bradford, 2014a). Full-waveform inversion methods incorporate all the information present in the reflected waveform and thus may provide a tool to reliably and accurately quantify thin-layer parameters even in the presence of signification noise. Previous research has demonstrated the efficacy of this approach using GPR reflection data for a variety of subsurface problems, including detecting contaminant infiltration (Kalogeropoulos et al., 2013), measuring soil water content (Lambot et al., 2004; Tran et al., 2012), and quantifying subsurface ε_{ef} and conductivity (σ) (Busch et al., 2012; Klotzsche et al., 2010). Babcock and Bradford (2014a) use a targeted full-waveform algorithm to estimate

thin- and ultra-thin layer properties on model GPR reflection data. Targeting a single reflection event of interest, e.g. a reflection from a contaminated zone, simplifies the inverse problem. They recovered thin-layer ε_{ef} within 8% and d within 10% of the true value for layer thicknesses as low as 8%λ for 4 different models. Here, we test that inversion algorithm on GPR reflection data collected in the field and in the laboratory.

Methodology

Inversion

The inversion uses Nelder-Mead gradient-based simplex search method to minimize the cost function, ϕ, with respect to user-defined parameters as follows (Lagarias et al., 1998):

$$\varphi = \sum(d_{obs} - d_{calc})^2 \tag{3.1}$$

where d_{obs} is the data and d_{calc} is a model wavelet. Babcock and Bradford (2014a) provide a full description of the forward model used to generate d_{calc}. Given a layered earth model, the 1D reflectivity model starts at the lowermost layer and recursively computes reflection and transmission coefficients upwards through a stacked multi-layer system to compute R_1, the reflectivity from the total stack, which we observe at the uppermost boundary (Muller, 1985). The model then convolves R_1 with a user-defined source wavelet. The resulting waveform simulates the measured GPR signal assuming that a 1D model is a good approximation and that layer properties are homogeneous and isotropic.

The 1D model can include any number of layers. It uses ε_{ef}, σ, and d for each layer in calculating R_1. Then, we can define any subset of these parameters as the

inversion parameters. In most cases, we fix the layer properties above and below the thin-layer and solve for thin-layer parameters as well as overburden thickness (ℓ). We assume that some other methods (velocity analysis, direct sampling) have provided estimates of the upper and lower layer properties. As demonstrated in the model testing, we first must invert for the effective source parameters using a reflection from an uncontaminated layer 1/layer 3 boundary. Inverting for the effective source function allows the algorithm to compensate for propagation effects due to overburden characteristics. Assuming a Gabor wavelet source function, the user-defined inversion parameters are central frequency (f_0) (Hz), phase rotation (η), and function width (δ_0) (s). We then can use these source parameters as the effective source wavelet parameters in the reflectivity model to invert for thin-layer parameters.

In either case, we randomly select starting values using a Monte-Carlo approach from a pre-determined uniform distribution. The algorithm searches for those inversion parameters that minimize equation 3.1 and returns parameters that correspond to that local minimum value (ϕ_{LM}). It replicates this gradient-based search 1000 times and finds the global minimum (ϕ_{GM}) from all ϕ_{LM}. We estimate uncertainty from the root mean square (RMS) error of 10,000 parameter pairs around a parameter pair corresponding to ϕ_{GM} and choose those paired parameters which fit equation 3.1 within the estimated level of noise. We perform this analysis for several available combinations of parameter pairs, but caution that the total uncertainty is coupled to the 4+ dimensions of the solution. For additional details, see Babcock and Bradford (2014a).

Testing

Examples

We tested the inversion on 2 laboratory and 2 field data sets for 4 different NAPL scenarios. All data were collected in transverse electric (TE) mode using Sensors and Software PulseEkko Pro antennas. Example 1 is air -oil-water. Example 2 is saturated-sand/DNAPL-sand/clay. Example 3 is moist sand/LNAPL-sand/saturated sand. Finally, Example 4 is air/snow/oil/ice, where the snow layer was a thin-layer and the oil layer was an ultra-thin layer. This example presents a challenging test case for the inversion algorithm as we inverted for the electrical properties of both the snow and oil layers.

For each data example, the reflection event from an uncontaminated area provides a background wavelet which we use to invert for the source parameters. For that inversion, the electrical properties of the uncontaminated layers can remain fixed, while f_0, δ_0, and η act as the inversion parameters. For Example 2 and 4a, additional thin layers in our data forced us to simultaneously invert for the source parameters as well as additional thin-layer properties.

Except for the change in parameters to be optimized, the source inversion routine follows the same methodology as the thin-layer inversion. Subsequently, for each example, we use the corresponding inversion solution for f_0, δ_0, and η as the source parameters in the inversion for thin-layer properties. In taking this approach, we assume that the background electrical properties are constant over the survey area.

Example 1

The first data example simulates an oil spill on cold ocean water. We set up a plastic tank in a freezer room and maintained the water temperature at 2° C. The addition of commercial rock salt (NaCl) raised the water salinity to 32 parts per thousand (ppt) in order simulate cold sea water. We collected data with antennas (f_0=1000 MHz) suspended on a wooden plank 1.16 m over the water (Figure 3.1). After collecting control data without oil present, 189 liters (L) of oil released into the tank formed a 0.027 m (16%λ) layer of oil over the salt water. The oil for the experiment was a commercially available motor oil. Addition of 0.1% by volume naphthenic acid and 0.5% by volume brine solution (35 ppt) altered motor oil conductivity and total acid number (TAN) to be more similar to that of crude oil. Direct measurements of salinity and TDR measurements for ε_{oil} provided a comparative reference for inversion performance (Table 3.1). Pre-inversion data processing steps included a time-zero correction, bandpass filter (250-500-2000-4000 MHz), spherical spreading correction (t^1), and reflection event windowing.

Example 2

The second laboratory example consisted of a plastic tank filled with a well-sorted saturated sand overlying a saturated sodium bentonite clay ($Na_2Ca[Al_2Si_4O_{10}(OH)_2(H_2O)_{10}]_{10}$) (Figure 3.2 and Table 3.1). The tank was 1.25 m x 0.48 m x .45 m. A depression with dimensions 0.34 m x 0.47 m x 0.04 m in the center of the saturated clay simulated a stratigraphic trap. Plastic tubing provided an injection port to introduce a non-toxic DNAPL (Novec HFE-7200) into the trap. We collected data before and after introduction of the simulated contamination. Calculated DNAPL-layer

thickness was approximately 0.022 m (9%λ). Babcock and Bradford (2013) further describe characterization of relevant material properties for the experiment.

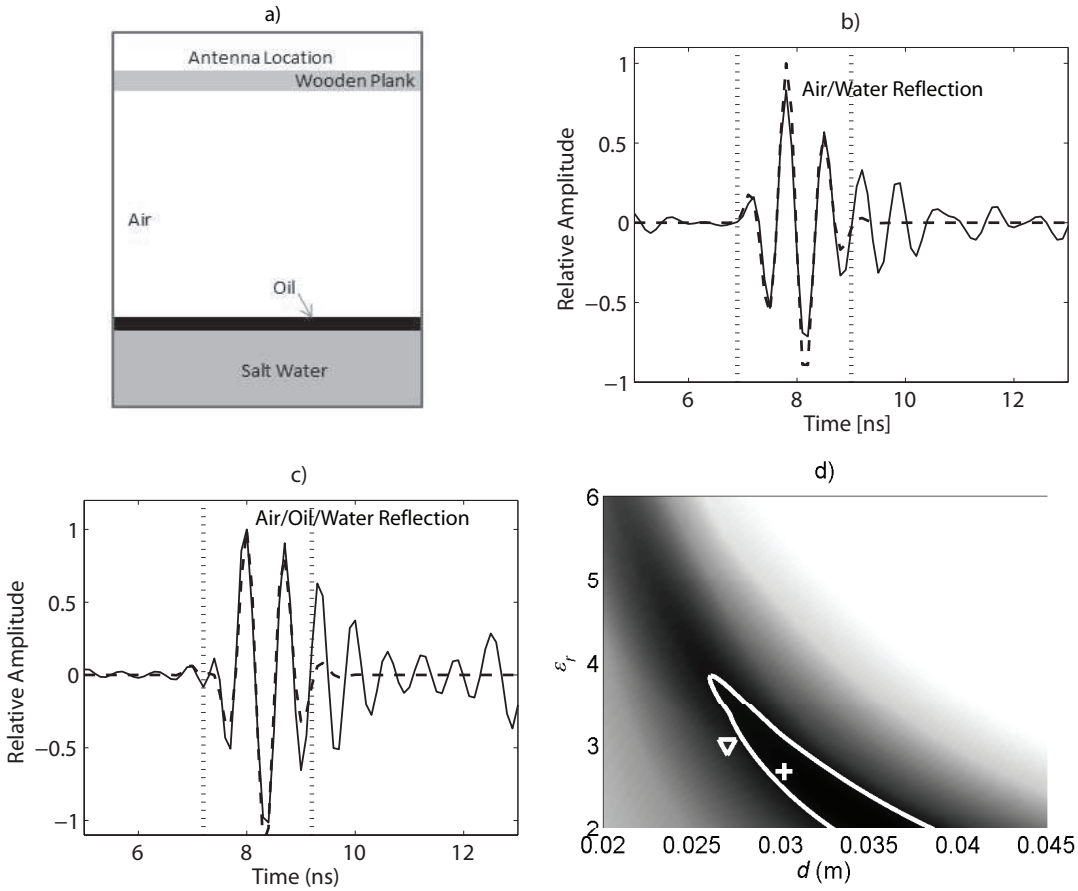

Figure 3.1: Example 1 showing a) Diagram of setup for data collection; b) Data (solid line) from the air/salt water reflection and the inversion results (dashed line) from the source wavelet inversion; c) Data (solid) from the air/oil/water reflection and inversion results (dashed). Vertical dotted lines indicate the data window used for the targeted inversion algorithm. d) plot showing coupled uncertainties between ε_{oil} and d_{oil}; + is solution corresponding to ϕ_{GM}, triangle is measured values, and the line encloses all paired values where the objective function is within 10% of ϕ_{GM}. Darker shading indicates lower values of the objective function.

Table 3.1: Physical and electrical properties for laboratory and field data examples.

Data	Layer	ε_r	σ_{ef} (S/m)	d (m) (%λ)
1	1, air	1	0	1.01
	2, oil	3.0 ± 0.5	$5 \pm 1 \times 10^{-4}$	0.027 (16%)
f_0=1000 MHz	3, salt water	88	3.5 ± 0.1	0.25
2	1, saturated sand	25 ± 1	0.007 ± 0.003	0.39
	2, DNAPL-saturated sand	7.3 ± 0.4	9.6×10^{-4}	0.022 (9%)
f_0=1000 MHz	3, clay	35	1	0.07
3	1, dry sand	4.9	5×10^{-5}* 2×10^{-4}*	4
	2, LNAPL-saturated sand	8.5	0.016 ± 0.007	0.3 (19%)
f_0=100 MHz	3, saturated sand	21.3	$3.3 \pm 0.2 \times 10^{-3}$	15
4a	1, air	1	0	1
	2, snow	1.4 – 2	10^{-5}	0.05 – 0.14 (<50%)
f_0=1000 MHz	4, sea ice	4.5	0.03	NA
4b	1, air	1	0	1
	2, snow	1.4 - 2.4	10^{-5} **	0.05 – 0.20
f_0=1000 MHz	3, oil	3.5	10^{-5} **	2 ± 1 (≅ 9%)
	4, sea ice	4.5	0.03	NA

*** Reported σ values for vadose zone are higher in contaminated region; lower value used in source inversion; see Sauck et al. (1998) for details.**
**** Estimates only; not measured on-site (Bradford et al., 2010)**

We collected multi-offset data in 0.02 m source-receiver separation increments across the top of the tank with 1000 MHz antennas. Data processing steps included a time-zero correction, bandpass filter (100-200-2000-4000 MHz), pre-stack phase-shift time migration (Gazdag and Sguazzero, 1964), stacking, applying a top mute, and target windowing.

We picked individual traces to use for the source wavelet inversion from the uncontaminated layer 1/layer 3 reflection (Figure 3.2). However, close examination of the data indicated the presence of another thin layer above the primary sand/clay horizon. This thin-layer was likely caused by sand compaction during the experimental setup and therefore probably reflects a porosity difference between the bulk overburden sand and the sand just above the clay layer. Due to the extra thin layer, during the source inversion we inverted for the permittivity (ε_{sand2}) and thickness (d_{sand2}) of the extra layer as well as for f_0, δ_0, η, and ℓ. Unfortunately, we have no direct measurements of the properties of this layer to use in evaluating solution accuracy. Subsequently, we used the inversion solution for ε_{sand2} in the inversion for the DNAPL-layer parameters for the 4-layer case: saturated sand/dense-saturated sand/DNAPL-saturated sand/clay. We inverted ε_{napl}, σ_{napl}, and d_{napl} as well as d_{sand2} and σ_{sand2}.

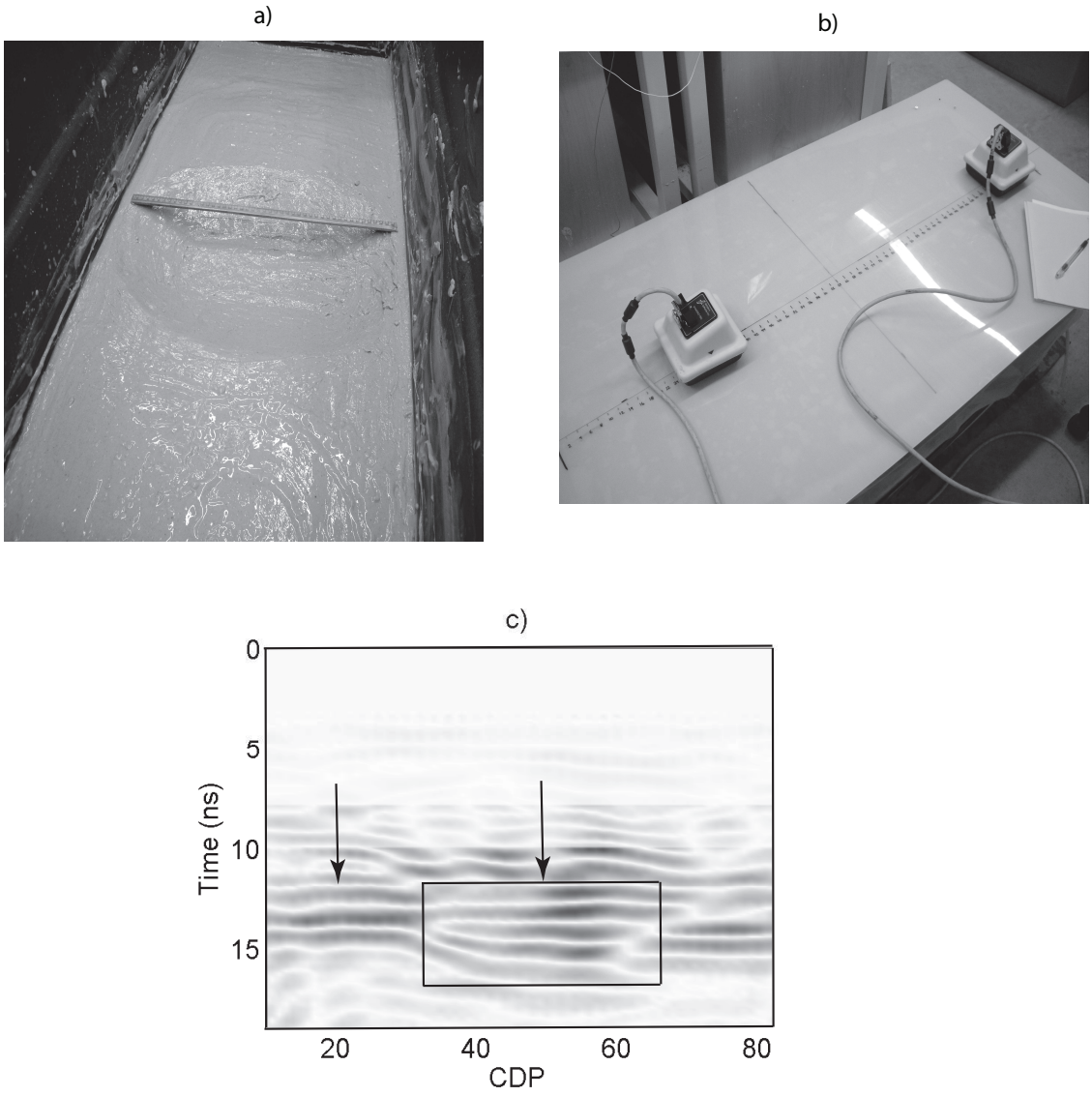

Figure 3.2: Laboratory setup for saturated-sand/DNAPL-saturated sand/clay system, where a) shows Layer 3, the sodium bentonite clay, with the depression to contain the injected DNAPL, and b) shows an example of antenna positioning for multi-offset data collection after filling the remaining tank space in the tank with saturated sand. c) The processed, time-migrated stacked data with top mute applied; topographic depression is located approximately between CDP 40 and 60 (box). Solid arrow points to first arrival of the sand/dense sand/clay reflection event; the reflection arrives earlier in time at the center of the tank (CDP 50), corroborating our result for a thicker dense sand layer over the topographic depression. Dashed arrow points to the first arrival of the sand/dense sand/DNAPL sand/clay reflection event over the center of the depression.

Example 3

The first field example was collected at former Wurtsmith Air Force Base, Michigan. A plume of spilled LNAPL hydrocarbons is floating on the water table and has subsequently smeared approximately 0.3 m thick over the vadose zone/saturated zone interface (Figure 3.3). Extensive use of geophysical methods including GPR has thoroughly characterized this contaminated site (Table 3.1) (Bradford and Deeds, 2006; Bermejo et al., 1997; Sauck et al., 1998). Markedly reduced reflection strength and a "shadow" zone of preferential attenuation clearly marks the contaminated region (Bradford and Deeds, 2006; Sauck et al., 1998).

We collected data using 100 MHz unshielded antennas with a fixed offset of 0.3 m and suspended slightly above ground level. We performed the source inversion on 2 different traces from the uncontaminated regions (located at approximately 152 m and 240 m) and the thin-layer inversion using 3 traces from the contaminated region (at approximately 187, 198, and 210 m) (Figure 3.3). Processing steps include a time-zero correction, bandpass filter (12-25-200-400 MHz), spherical spreading correction (t^1), and reflection event windowing. We also tested the thin-layer inversion routine on 3 traces from the uncontaminated region in order to assess the robustness of the inversion.

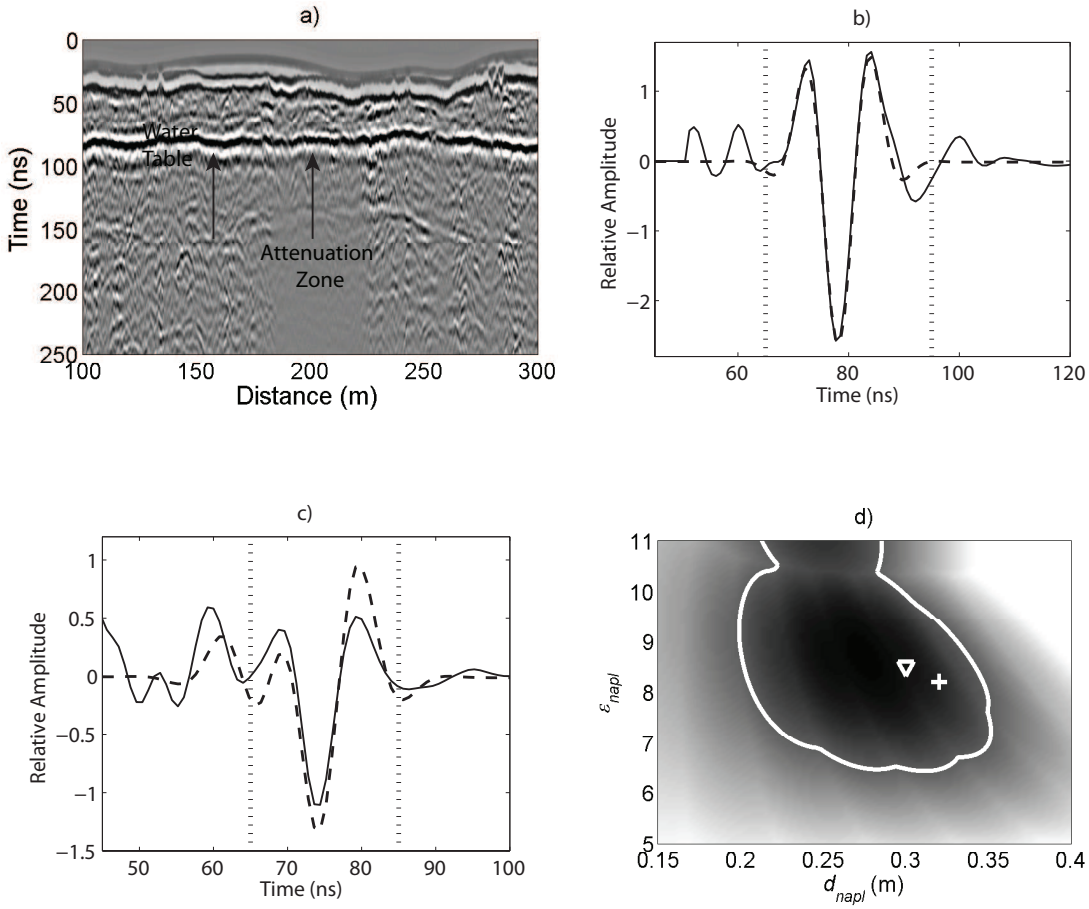

Figure 3.3: a) Data from Wurthsmith field site; contaminated region is marked by increased attenuation below the water table. Leftmost arrow is approximate position of traces for source parameters inversion; rightmost arrow is approximate position of traces for thin-layer inversion. b) Data (solid line) from the uncontaminated water table reflection and the inversion results (dashed line) from the source wavelet inversion; c) Data (solid) from the LNAPL region and inversion results (dashed). Vertical dotted l;ines indicated target window. d) Coupled uncertainties between ε_{napl} and d_{napl}; + is solution corresponding to ϕ_{GM}, triangle is measured values, and the line encloses all paired values where the objective function is within 10% of ϕ_{GM}. Darker shading indicates lower values of the objective function.

Example 4

The second field example is a controlled oil spill above sea ice. Testing occurred at Svalbard, Norway. We collected radar data over clean and contaminated areas using 1000 MHz central-frequency antennas slung beneath a helicopter (Figure 3.4) (Bradford

et al., 2010). In the contaminated zone, the introduced ultra-thin oil layer overlying the ice was covered by a thin layer of snow. The inversion uses data from helicopter traverses at 5 m elevation above the surface; elevations are approximate due to helicopter flight characteristics. Bradford et al. (2010) provide further details on the experiment design and describe measurement of the relevant electrical properties using travel-time analysis. Data processing steps included a time-zero correction, bandpass filter (250-500-2000-4000 MHz), background subtraction, and target windowing.

For Example 4, we performed the inversion routine on 5 different data traces: 2 from the uncontaminated region and 3 from the contaminated locations across the survey area. We hand-picked data traces having different snow and oil thicknesses in order to demonstrate the inversion robustness. In example 4a, we used the snow/ice reflection event for the source wavelet inversion in the uncontaminated three-layer case of air/snow/ice, meaning that f_0, δ_0, η, ε_{snow}, d_{snow}, and ℓ were the inversion parameters. The snow layer was less than ½λ for all traces. For Example 4b, two thin layers were present: snow and oil (Table 3.1). Thus ℓ, ε_{snow}, and ε_{oil} as well as d_{snow} and d_{oil} were all inversion parameters in the contaminated area. Snow permittivity at the site varied due to wind redistribution (Bradford et al., 2010). We used the range for ε_{snow} from the source inversion to bound solution values for ε_{snow} in Example 4b. Oil layer thickness ranged from 0 to 0.036 m (<17%λ). Mean oil thickness was 0.0192 m (<9%λ). We do not report values for either σ_{snow} or σ_{snow} since previous work demonstrated that the algorithm is not sensitive to low σ values (Babcock and Bradford, 2014a).

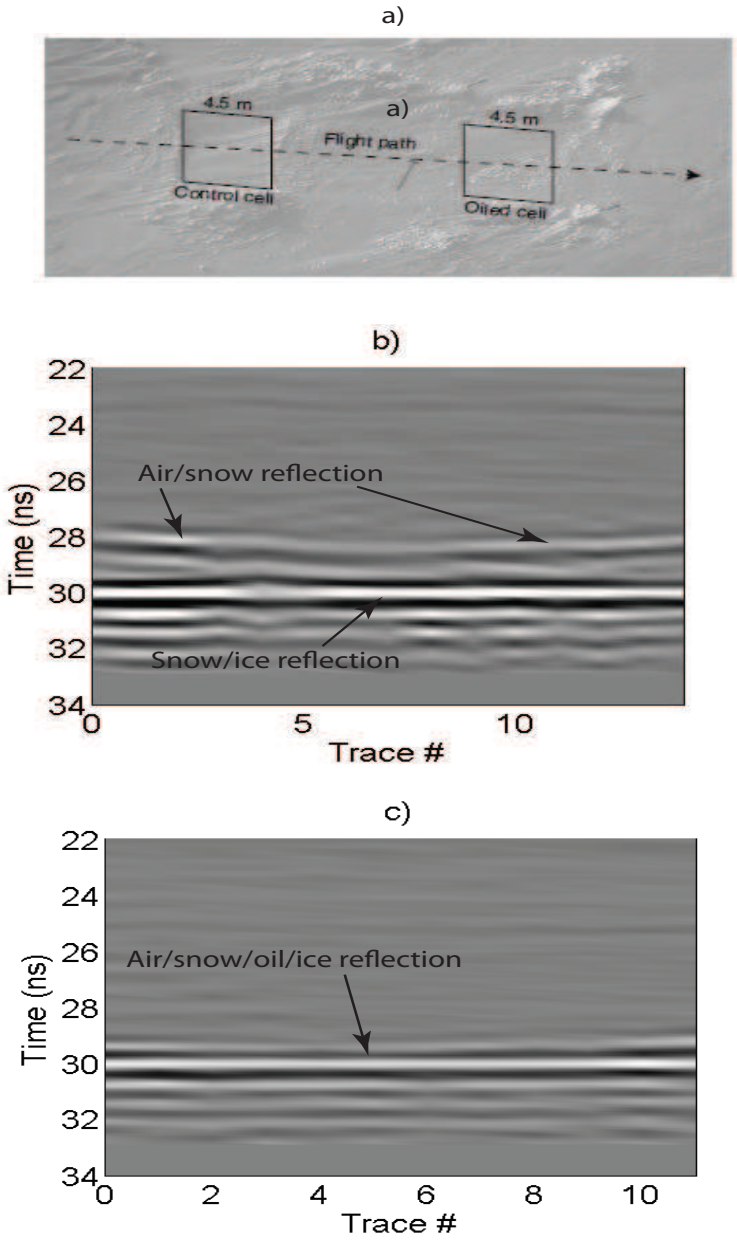

Figure 3.4: a) Helicopter flight path over the uncontaminated (control) cell and the oily cell for Example 3; b) example data collected along flight path over clean test cell demonstrating variable snow thickness, and c) oily cell (Bradford et al., 2010).

Inversion Results

Source Wavelet Inversion

All data were collected with 1000 MHz antennas. In Example 1 and 4, with the antennas suspended in air, the inversion solution for f_0 is up to 40% greater than the manufacturer-specified f_0 (Table 3.2). In Example 2, the antennas were coupled to the saturated sand, and the effective source frequency corresponding to the inversion solution is 525 MHz. Estimated f_0 for Example 3 is within 6% of the values reported by Bradford and Deeds (2006). Uncertainties in the source parameters are estimated from coupled f_0, δ_0 and f_0, η pairs (Figure 3.5 and Table 3.2). We proceed with the inversion for the thin- and ultra-thin-layer parameters using the results for the Gabor source wavelet parameters for the effective source function.

Example 1

The inversion retrieves ultra-thin layer ε_r and d within 10% of the estimated value (Figure 3.1 and Table 3.3). The inversion solution for σ deviates over an order of magnitude from the estimated oil σ. The rate of conversion to ϕ_{GM} is 5%, and the global ϕ_{GM} is 99% of the next closest ϕ_{LM}.

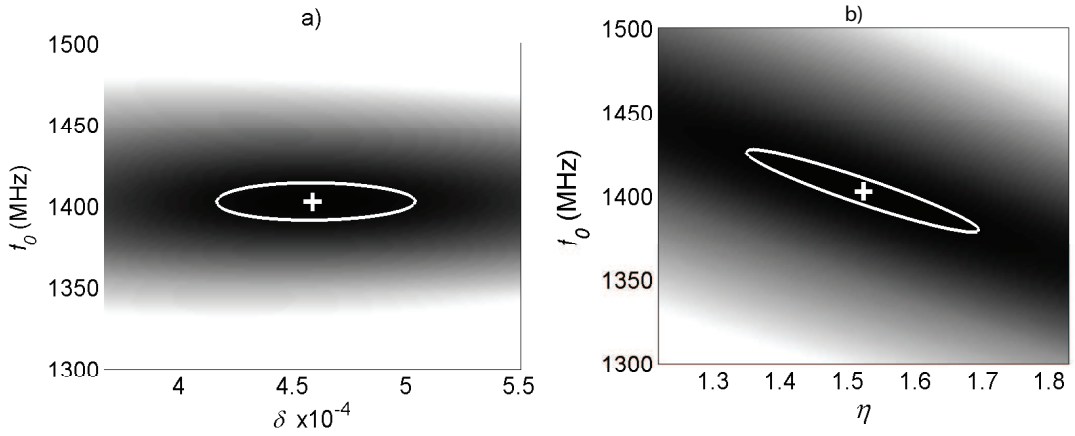

Figure 3.5: Paired f_0, δ_0 (a) and f_0, η (b) and uncertainties for the solutions from the source parameter inversion for Example 1. The + marks the inversion solution and the line encloses all paired values where the objective function is within 10% of ϕ_{GM}. Darker shades are smaller values of the objective function. Results for other tests are in Table 3.2.

Table 3.2: Inversion solution and standard deviation for source wavelet parameters using reflection from Layer 1/Layer 3 in an uncontaminated area; in Examples 2 we simultaneously inverted for additional dense-sand thin layer parameters, and in Example 4 for thin snow layer parameters; those results are in Table 3.3. Figure 3.5 shows an example of solution uncertainties for f_0, δ_0 and f_0, η pairs.

Example	Source (MHz)	Convergence Rate	f_0 (MHz)	δ_0 (ns)	η
1	1000	22%	1400 ± 10	.46 ± 0.04	1.5 ± 0.2
2	1000	<1%	525 ± 30	1.175 ± 0.001	-0.785 ± 0.01
3	100	47%	75 ± 5	6.3 ± 0.7	0.54 ± 0.06
4	1000	<1%	1360 ± 200	.63 ± 0.08	0.745 ± 0.005

Example 2

Results obtained during the source parameter inversion included the parameters of the thin dense sand layer: d_{sand2} = 0.037 m and ε_{sand2}=20.7 (Figure 3.6). The inversion for DNAPL-layer parameters retrieved ε_{napl} and d_{napl} within 6% of measured values (Figure 3.6 and Table 3.3). The solution for σ_{sand2} is reasonable, but the solution σ_{napl} is an order of magnitude different from the calculated value. Although the solution for Example 2 is quite good overall, as discussed by Babcock and Bradford (2014a) low rates of convergence (<1%) and small differences (<1%) between ϕ_{GM} and $\phi_{LMnearest}$ may indicate the increased difficulty of finding a unique and accurate solution given the complicated nature of this 4-layer problem.

Example 3

Bradford and Deeds (2006) estimated the control values using a calculation of the offset-dependent reflectivity and comparison of measured values to a range of background models. There are also several literature values for NAPL thickness at this site (Bradford and Deeds, 2006; Sauck et al., 1998). The inversion retrieves ultra-thin layer ε_r within 8% of their estimated value and *d* within 13% (Figure 3.3 and Table 3.3). The rate of conversion to ϕ_{GM} is 24%, and the global ϕ_{GM} is 96% of the next closest ϕ_{LM}. The uncertainty associated with these results is highly variable depending on the coupling between parameters pairs, and may not be well-constrained by the 2D representation of the RMS error (Figure 3.3). When tested in the uncontaminated area, the inversion retrieved "layer" permittivity within 2% (ε_r = 4.8 + 0.2) of the value measured by Bradford and Deeds (2006) (ε_r = 4.9).

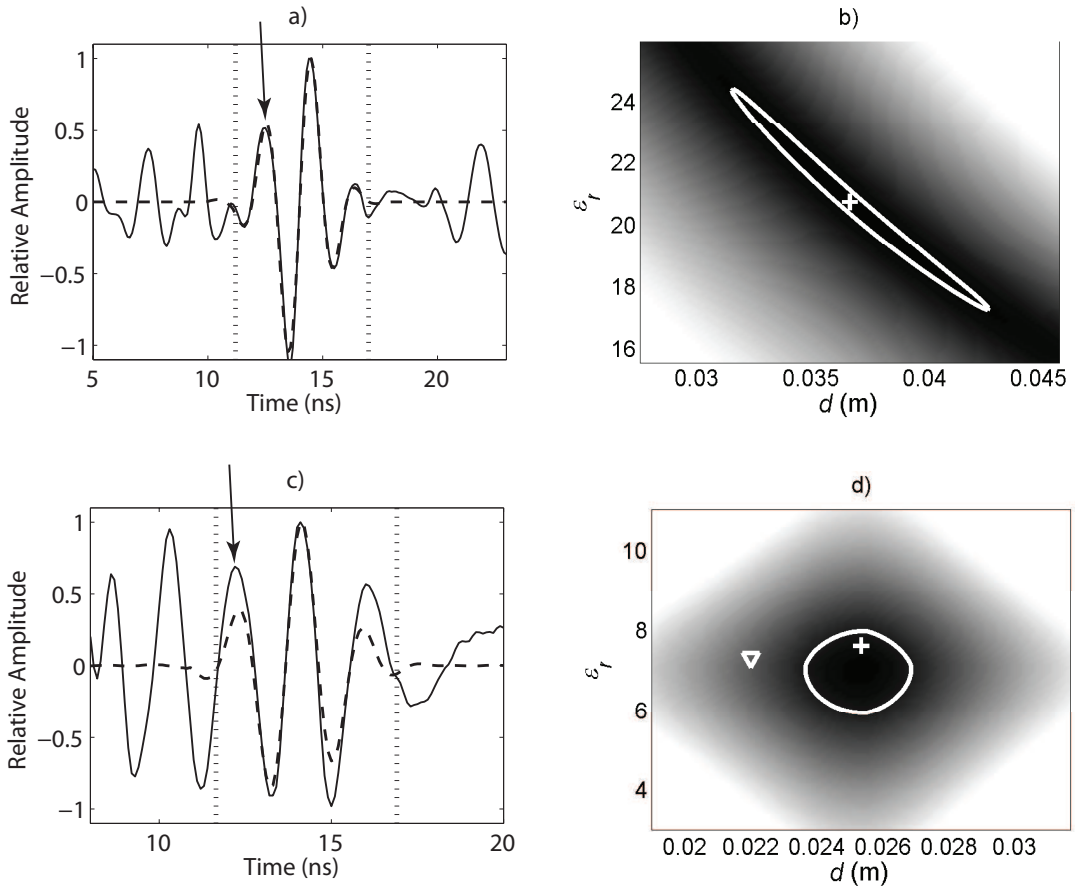

Figure 3.6: a) Trace (solid line) located at CDP 20 with inversion solution for source parameters (dashed line); vertical dotted lines indicate target window used in inversion algorithm; arrow points to the same location as the leftmost arrow in Figure 3.2c. Note the high amount of noise present in the data. b) Plot showing coupled uncertainties for ε_{sand2} , d_{sand2} from the source inversion; + is solution corresponding to ϕ_{GM} and the line encloses all paired values where the objective function is within 10% of ϕ_{GM}; darker shading indicates lower values of the objective function. The true values for ε_{sand2} , d_{sand2} are unknown. c) Solution (solid) vs data (dashed) for DNAPL parameters using trace at CDP 50; the arrow corresponds to the rightmost arrow in Figure 3.2c. The presence of multiple reflection events causes uncertainty in defining the target window. d) Plot showing coupled uncertainties between ε_{napl} and d_{napl}; triangle indicates measured values (other notation the same as part b).

Example 4

Solutions for ε_{snow} from the source wavelet inversion ranged from 1.46 to 1.81 (Table 3.3). Assuming a $d_{snow} \leq 2\varepsilon_0$, these results suggest a maximum %error for snow

permittivity in the uncontaminated area of 10% (Figure 3.7). Results for d_{snow} from the source inversion were well within the measured values across the cell. In addition, the inversion solution matches the data well over a range of snow layer thicknesses (Figure 3.7). The inversion demonstrates an overall lack of sensitivity to σ again in this example.

We proceed with the inversion for oil and snow layer parameters in Example 4b and constrain ε_{snow} to the solution range from Example 4a during the inversion for snow and oil thin- and ultra-thin layer properties. Low rates of convergence (<1%) and small differences between ϕ_{GM} and ϕ_{LM} (ϕ_{GM} >90% $\phi_{LMnearest}$) may indicate that the non-uniqueness of the solution is problematic for this example. Nevertheless, the inversion retrieved ε_{oil} within 10% of the estimated value, and the solutions for d_{oil} are within the range of measured oil thicknesses (Figure 3.7 and Table 3.3). The inversion results for d_{snow} exceed the measured snow cover by a maximum of 12% (Table 3.3).

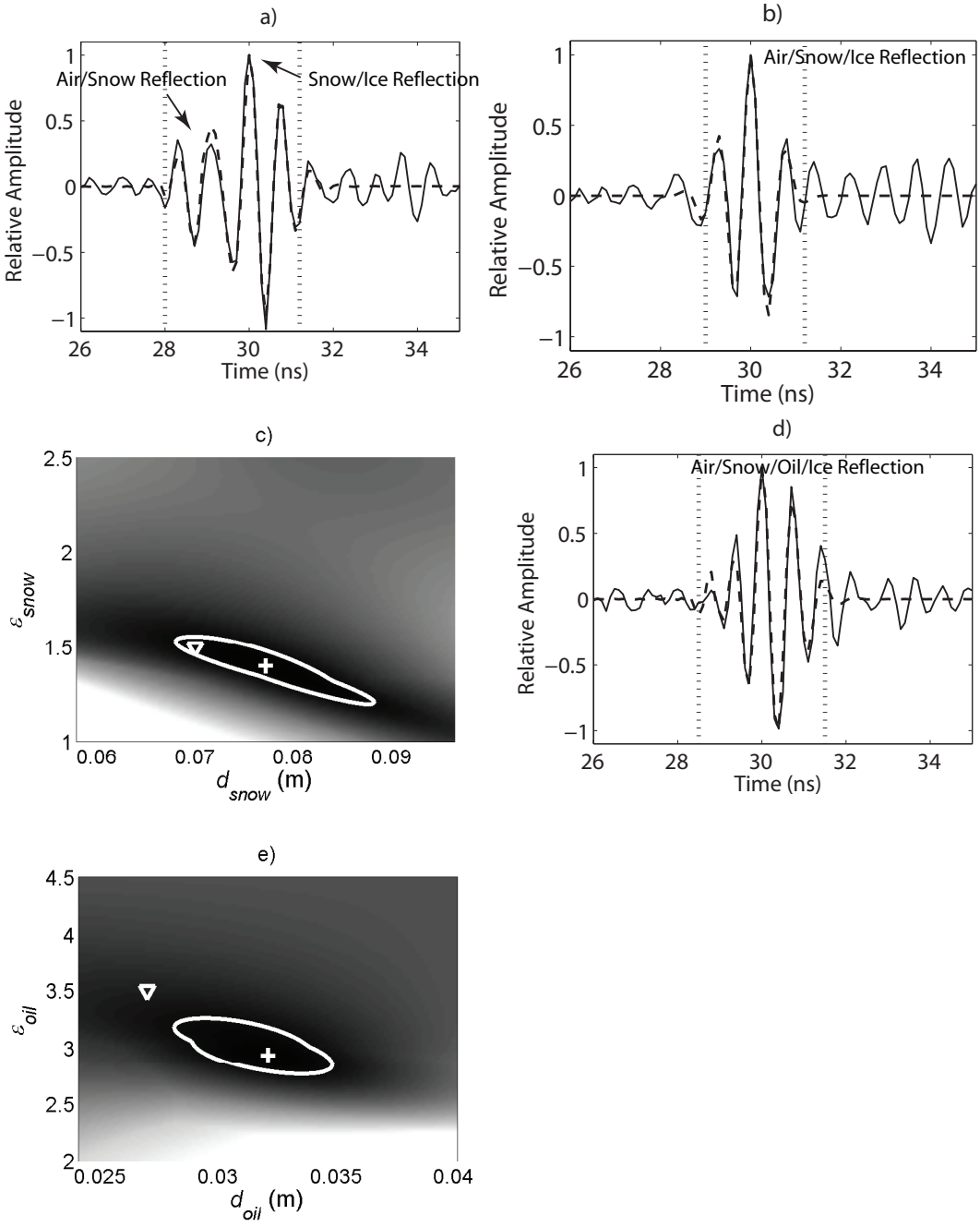

Figure 3.7: Data (solid) and inversion results (dashed) for Example 3. Labels indicate reflection events and vertical dotted lines show the data window used for the targeted inversion algorithm. a) uncontaminated snow over ice with $d_{snow} \cong 0.11$ m (46%λ); b) uncontaminated snow over ice with $d_{snow} \cong 0.07$ m (25%λ) ; c) Plot showing coupled uncertainties between ε_{snow} and d_{snow} for b); + is solution corresponding to ϕ_{GM}, triangle marks the estimated values, and the line encloses all paired values where the objective function is within 10% of ϕ_{GM}. d) data (solid) and

inversion results (dashed) for an ultra-thin oil layer (0.02 m, 9%λ) underneath an thin snow layer (0.04 m, 16%λ). e) Plot showing coupled uncertainties between ε_{oil} and d_{oil}; notation same as part c).

Table 3.3: Ultra-thin-layer parameters for a) Example 1, b) Example 2, c) Example 3, d) Example 4a, and e) Example 4b with the inversion results corresponding to ϕ_{GM}. Uncertainties for ε_r, d pairs are shown graphically in Figures 3.1- 3.7.

a) $\phi_{GM} = 99\%\phi_{LM\ (nearest)}$

Parameter	Control Value	Solution	Bounds
ε_{oil}	3	2.686 ± 1.3	2 - 8
d_{oil} (m)	0.027	0.030 ± 0.05	0 – 1
l (m)	1.03	0.965 ± 0.001	0 – 5
σ (S/m)	≈5 x 10^{-4}	8 ± 3 x 10^{-6}	0 – 0.1

b) $\phi_{GM} = 99\%\phi_{LM\ (nearest)}$

Parameter	Control Value	Solution	Bounds
ε_{napl}	7.3 ± 0.3	7.7 ± 0.8	2-10
d_{sand2} (m)	*	0.050 ± 0.001	0 – 0.1
d_{napl} (m)	0.022	0.024± 0.002	0 – 0.1
σ_{sand2} (S/m)	*	0.012 ± 0.002	0 – 0.1
σ_{napl} (S/m)	9.6 x 10^{-4}	4 ± 5 x 10^{-3}	0 – 0.1

*Properties not measured; refer to text for discussion

c) $\phi_{GM} = 96\%\phi_{LM\ (nearest)}$

Parameter	Control Value	Solution	Bounds
ε_{napl}	8.5	8.2 ± 1.5	2 - 12
d_{napl} (m)	0.3	0.34 ± 0.06	0 – 1
l (m)	4	4.1 ± 0.2	2 – 10
σ (S/m)	0.016 ± 0.007	0.001 ± 0.001	0 – 0.1

d) ϕ_{GM}= 76% - 94%$\phi_{LM\ (nearest)}$

Parameter	Control Value	Solution	Bounds
ε_{snow}	1.4 – 2	1.46 – 1.81	1 - 5
d_{snow} (m)	0.05 - 0.14	0.04 – 0.15**	0 – 1
l (m)	5 - 10	5.4 - 8.3	5 - 15

**Dependent on snow depth at trace location; see Figure 3.7

e) ϕ_{GM} = 74 - 94%$\phi_{LM\ (nearest)}$

Parameter	Control Value	Solution	Bounds
ε_{oil}	3.5	3.2 ± 0.2	1 – 8
d_{snow} (m)	0.04 – 0.07	0.005 – 0.0787	0.001 – 1
d_{oil} (m)	0 – 0.036	0.004 - 0.0321	0.001 – 1
l (m)	5 – 10	8.67 ± 0.5	0 - 20

*Estimated range based on snow density at site and constrained by solution from
**Snow σ and oil σ not measured at field location

Discussion

In 2 different scenarios, the inversion algorithm recovered effective source wavelet parameters and an additional set of thin-layer parameters simultaneously (Examples 2 and 4). For Example 2, since we have no direct measurement of these properties, we assess the resulting estimate for sand permittivity in relation to known physical properties using petrophysical transformations. Babcock and Bradford (2013) calculated to the bulk overburden sand porosity of approximately 37.8% from Time Domain Reflectometry (TDR) measurements. The inversion retrieved thin-layer permittivity for this addition layer of 20.7. Assuming complete saturation, an ε_{sand2} of 20.7 yields a porosity of 34.8% using the CRIM equation (Knight and Endres, 2005). Thus, the inversion result for ε_{sand2} seems to corroborate the presence of a compacted,

lower-porosity sand layer above the clay. We were unable to measure the depth of this layer directly, but 0.037 m ≅ ¼λ at 525 MHz. In addition, the inversion solution for d_{sand2} from thin-layer inversion for contaminant properties is approximately 0.013 m thicker than the solution for d_{sand2} from the effective source parameter inversion. Visual examination of the stacked section corroborates this result as the reflection event arrives slightly earlier in time above the center of the depression than over the flat-lying part of the clay/sand horizon (Figure 3.2).

In Example 4a, the inversion results for ε_{snow} from the source parameter inversion agreed well with the findings of Bradford et al. (2010). They observed that snow densities, and therefore permittivities, were relatively low for the loosely packed snow in the uncontaminated area, and our results for ε_{snow}, ranging from 1.46 – 1.81, are within 10% of the values measured in the field. When inverting for snow and oil layer properties simultaneously in Example 4b, the overall reliability of the results are remarkable considering the thinness of both the oil and snow layers and the added difficulty having one thin layer (snow) and one ultra-thin layer (oil) present above the ice.

However, the inversion results for σ deviate significantly from real values. Previous work (Babcock and Bradford, 2014a) notes that σ solutions may be unreliable until reaching a certain threshold value. This observation makes intuitive sense given that σ functions both to attenuate EM wave propagation and also to change the reflectivity response (notably in the case of high σ). That threshold may be >0.0316 S/m, and none of these data had a thin-layer σ greater than that value. Thus, we caution that this inversion algorithm, while performing robustly for ε_r and d, is not likely to retrieve σ accurately for thin-layers of these types of contaminants. Continued work to retrieve

thin-layer σ should include testing on data at lower frequencies, <100 MHz, as per Tsoflias and Becker (2008).

Finally, our full-waveform inversion relies on a user-defined window to target the reflection event. Correctly identifying and windowing the desired reflection event is paramount for robust inversion performance. The choice of the reflection window has a large impact on inversion results and subsequent errors. Our testing indicates that choosing a shorter window length centered on the peak of the reflection event promotes more reliable inversion performance (Figure 3.8). In fact, this result is promising because it demonstrates that the inversion algorithm may be relatively insensitive to noise, since it depends on more of the information within the wavelet that is contained near the peak of the reflection event and that peak is less sensitive to noise than the edges of the wavelet.

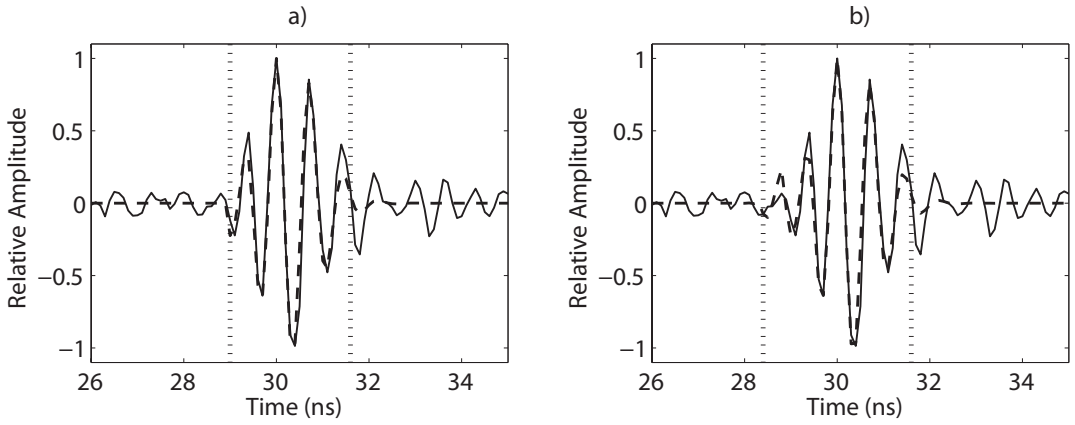

Figure 3.8: Inversion results (dashed) plotted vs data (solid) to demonstrate the effect of changes in user-defined reflection window on solution accuracy; dashed lines show the data window used for the targeted inversion algorithm. a) Solution corresponding to data windowed between 29.0 and 31.5 ns; b) Solution when using a longer reflection window (28.5 - 31.5 ns). The solution shown in b) returns anomalously high values for ε_{oil} (>6).

Conclusions

Reliable estimation of thin-layer parameters using this inversion algorithm hinges on estimating the effective source wavelet parameters. Our source wavelet inversion was able to recover effective wavelet parameters as well as additional thin-layer parameters in the case of Example 2 and Example 4a. Given an effective source parameter function, this full-waveform inversion algorithm for GPR reflection data may accurately recover thin- and ultra-thin layer ε_r and d at contaminated sites. The full-waveform inversion recovered thin- and ultra-thin layer ε_r and d within 15% of the measured or estimated values down to layer thicknesses as low as 9%λ. In Examples 2 and 4b, the algorithm also successfully simultaneously inverted for the properties of 2 thin layers: an overburden layer and the contaminant layer. Our testing and observations indicate that practitioners could implement this algorithm to characterize contaminated sites where contamination has dispersed throughout the subsurface into thin- and ultra-thin layers. Careful use of this inversion could reduce remediation costs and time. Our algorithm is especially applicable to time-lapse monitoring of NAPL-contaminated sites.

CHAPTER FOUR: QUANTIFYING THE BASAL CONDITIONS OF A MOUNTAIN GLACIER USING A TARGETED FULL-WAVEFORM INVERSION: BENCH GLACIER, ALASKA

Abstract

Understanding glacier dynamics is a vital component of long-range climatological modeling, and glacier dynamics are inextricably linked to the basal conditions of glaciers. Seismic reflection methods can image the glacier bed under certain conditions. However, where a seismically thin layer of material is present at the bed, traditional analyses may fail to fully characterize bed properties. We use a targeted full-waveform inversion algorithm to quantify the basal layer parameters of Bench Glacier, Alaska: thickness (*d*), P-wave velocity (α), and density (ρ). We simultaneously invert for the seismic quality factor (*Q*) of the bulk glacier ice. The inversion seeks to minimize the difference between the data and a 1D reflectivity model using a gradient-based algorithm with starting values initialized from a Monte-Carlo scheme. We test the inversion algorithm on 4 basal layer models with 5% added Gaussian noise. The inversion retrieved thin-layer parameters within 10% of model parameters with the exception of seismic *Q*. For the seismic data set from Bench Glacier, inversion results indicate a thin basal layer of debris-rich ice within the study area having mean velocity 4000 ± 700 m s^{-1} , density = 1900 ± 200 kg m^{-3}, and thickness = 6 ± 1.5 m.

Introduction

Glacier dynamic processes contribute to climate change. Furthermore, changes in the dynamic parameters even of relatively small glaciers may have a disproportionately large impact on climate cycles (Meier, 2007). Thus ongoing research efforts recognize that understanding and modeling the glacier dynamics of mountain glaciers contributes a significant component to the validity of long-range climatological modeling (Nolan and Echelmeyer, 1999).

Glacier dynamics are strongly tied to the basal conditions of glaciers (Dow et al., 2013; MacGregor et al., 2005; Nolan and Echelmeyer, 1999). For example, movement of hard-bedded glaciers depends largely on friction and shear forces at the ice/bedrock interface (Cohen et al., 2005). In other cases, a distinct basal layer of debris-rich ice may exist (Hart, 1995). Increased rates of shear deformation or compression due to stratified facies and debris lenses within such a layer may cause over 50% of overall overall glacier motion (Chandler et al., 2005; Hart and Waller, 1999; Knight, 1997; Waller et al, 2000). Water inputs at the bed of the glacier can cause glacier surging (Anderson et al., 2004; Clarke, 2005; Howat et al., 2008; Magnusson et al., 2010; Smith, 2007), and the thickness of an existing water layer may be critical to estimating debris-bed friction (Cohen et al., 2005). The presence of subglacial sediments may impact glacier movement through deformation, decoupling, sliding, and uplift mechanisms (Alley et al., 1987; Anandakrishnan, 2003; Evans et al., 2006; Hart et al., 2011; MacGregor et al., 2005; Porter and Murray, 2001). In fact, interactions with basal sediments may be responsible for up to 80% of glacier movement in some cases (Hart et al., 2011). Given the gamut of possible basal parameters, it is obvious that reliably estimating subglacial conditions

predicates the understanding and modelling of glacier dynamics and of larger global climate models.

However, reliably quantifying the exact nature of the glacier bed is difficult (Smith et al., 2013). Such quantification is especially problematic over the substantial spatial extent of even small mountain glaciers. For instance, borehole video and penetrometer tests are time-consuming and only provide discrete observations. Previous research has used a plethora of geophysical techniques including both radar and seismic reflection methods in attempts to define basal conditions such as estimations of basal water conditions, constraining thickness and physical properties of glacial sediments, characterizing debris-rich basal ice layers, and defining bedrock topography (Baker et al., 2003; Blankenship et al., 1986; Bradford et al., 2013; Brown et al., 2009; Booth et al., 2013; Dow et al., 2013; Hart, 1998; Harper et al., 2010; Kim et al., 2010; King et al., 2004; Smith, 2007; Smith et al., 2013; Waller et al., 2000). Proper interpretation of seismic reflection data in particular can sometimes provide information about the physical properties of glacial ice and subglacial materials (Anandakrishnan, 2003; MacGregor et al., 2005; Smith, 2007). Velocity analysis is one common seismic tool often applied in the glacier environment.

Nevertheless, when a thin layer of material is present between the glacier bed and underlying bedrock, conventional seismic analysis tools may fail to reliably define basal conditions. If a thin-layer is present between two half-spaces, reflections of an incident wave from the top and bottom of that layer become convolved with one another. Widess (1973) demonstrated that resolving distinct reflections from the top and bottom of such a layer becomes impossible as a layer's thickness decreases below ¼ the dominant

wavelength, λ, of the signal in the material of interest. Depending on the source wavelet characteristics and the presence of noise, the limiting layer thickness for resolving those reflections may be as high as ½ or even ¾λ (Booth et al., 2013; Bradford and Deeds, 2006; Guha et al., 2005; Smith, 2007). In these situations, using traditional velocity analysis to quantifying the layer thickness (d), density (ρ), and P-wave velocity (α) is therefore also impossible (Anandakrishnan, 2003).

In the glacial environment, the limitations due to thin-bed problems may preclude detection of basal layers (Booth et al., 2013; Smith, 2007). Given the typical range of seismic P-wave velocities (α) for subglacial materials (Table 4.1), at a central frequency of 250 Hz, the resulting wavelength of 8 m means that a layer of sediment may be seismically thin even at thicknesses up to 6 m. Furthermore, at that frequency, an 11 m thick basal ice layer (BIL) may still be "thin." Although subglacial sediments or basal ice layers can sometimes accumulate in layers as thick as 12 -15 m, realistically these layers or layers of basal water may be much thinner still, on the order of 1 or 2 m or even less (Hart, 1995; Hart et al., 2011; Knight, 1997; MacGregor et al., 2005; Smith, 2007). Nonetheless, these "thin" layers may dramatically impact glacier dynamics (Chandler et al., 2005; Smith, 2007). In such a scenario, quantifying the basal characteristics is essential. Performing such quantification using seismic reflection methods can require the use of advanced techniques such as attribute analysis and inversion methodologies (Booth et al., 2013).

Accordingly, previous research has detected and parameterized subglacial characteristics based on reflection attributes such as phase, reflection strength, and reflection amplitude variation with offset (AVO) attributes (Anandakrishnan, 2003;

Booth et al., 2013; Dow et al., 2013; Smith et al., 2013). King et al. (2004) detected high amplitude reflection anomalies in a seismic reflection survey on an Antarctic ice stream and correlated the amplitude variances with the presence of basal water layer as thick as 0.6 m. Smith and others (2013) identified a basal sediment layer by extracting reflection coefficients from seismic data using the ratio of the multiples to primary reflections and comparing the reflection strength to common values for the acoustic impedances of sedimentary layers. Smith (2007) isolated changes in reflection polarity at the glacier bed within a seismic data set and defined spatially-discrete changes in ice sheet basal conditions based on reflection attributes. He concluded that saturated basal sediment thickness was ≥ 1.5 m.

Amplitude variation with offset analysis is particularly applicable to analysis of basal conditions in the presence of thin layers of basal material. This technique comprises quantification of change in reflection strength as a function of source-receiver offset (Castagna, 1993). Since the direction and amplitude of the AVO response depends on the properties of any thin layers present at a reflecting boundary, judicious analysis of AVO attributes thus can sometimes produce estimates of thin-layer parameters (Dow et al., 2013). For example, Anandakrishnan (2003) identified two different sediment lithologies beneath an ice sheet using normal incidence reflection strength and estimated $\alpha = 1700$ m s^{-1} for a dilatant sedimentary layer by examining the AVO reflection attributes. Dow et al. (2013) used a modified AVO approach to model the reflection characteristics of an ice sheet basal reflection event and infer the presence of thin underlying sediments having $\alpha = 2100$ m s^{-1} and $\rho = 1700$ kg m^{-3}, but were unable to quantify layer thickness.

However, AVO analyses often rely on comparison of modeled AVO curves with extracted amplitude information or inversions based on the AVO curves (Dow et al., 2013; Booth et al., 2013). On the other hand, targeted full-waveform inversions (FWIs) incorporate all the information contained within a reflection event rather than parameterizing individual attributes such as phase or AVO characteristics (Babcock and Bradford, 2014b; Plessix et al., 2012). In general, FWIs invert for subsurface parameters by iteratively minimizing the difference between the observed data and a synthetic model with respect to subsurface parameters (Operto et al., 2012). Full-waveform inversions thus have the potential to directly recover layer properties (Babcock and Bradford, 2014a). However, full-waveform inversion is complicated by problems of non-linearity and solution non-uniqueness, the coupled nature of material properties, and computing speed (Operto et al., 2012). Nevertheless, previous work has successfully applied a targeted full-waveform inversion algorithm to quantify thin-layer properties using radar reflection data (Babcock and Bradford, 2014b). The targeted approach simultaneously reduces the complexity of the inverse problem and minimizes computing time. Here we demonstrate the efficacy of that approach on synthetic seismic data. We then apply the inversion algorithm to a seismic data set from Bench Glacier, Alaska, in an attempt to quantify its basal conditions.

Table 4.1: Representative material properties in the glacier system (Booth et al., 2013; Bradford et al., 2009; Fowler, 1990; Gusmeroli et al., 2010; Johansen et al., 2003; McGinnis et al., 1973; Mikesell et al., 2013; Nolan and Echelmeyer, 1999; Press, 1966; Smith, 2007). We distinguish basal ice from bulk glacier ice as ice carrying stratified or dispersed debris from the glacier bed with distinct physical, chemical, and mechanical properties (Knight, 1997).

Material	α (m s^{-1})	ρ (kg m^{-3})	Q
Glacial Ice	3600 - 3800	917	22 - 220*
Water	1400 - 1600	1000	800 - 1000
Saturated Sediment	1400 - 2500	1700 - 2400	200 - 400
Basal Ice	2300 - 5700**	1500 - 2100	22 - 400
Bedrock	5000 - 5500	2700	100 -1500

* for temperate ice

** strongly temperature- and saturation- dependent

Materials and Methods

Forward Model

We use a 1D, vertical incidence reflectivity method to generate a reflection series from any given layered subsurface model (Babcock and Bradford, 2014c; Muller, 1985). This model accounts for multiples and attenuation via the full wavenumber calculation. However, it assumes a vertical incidence reflection in a system composed of linearly elastic, homogeneous layers and does not account for 2- or 3-D effects. Obviously these assumptions are violated to some extent in the glacier environment since glacier ice is not homogeneous and the bed of the glacier may be able irregular. Nevertheless, we feel this 1D approach provides a reasonable first-order approximation for modeling seismic reflection events where a thin layer is present and violations of the assumptions are not too severe. Babcock and Bradford (2014b) detail the use of a similar forward model for

modeling radar data. Here we present additional considerations and theory relevant to seismic methods.

Seismic Considerations

Seismic velocities are well-known to be frequency-dependent (Aki and Richards, 1981). We calculate the frequency-dependent velocity α' as follows:

$$\alpha' = \alpha \left(1 + \frac{1}{\pi Q} ln \frac{\omega}{\omega_0}\right) \quad (4.1)$$

where ω is frequency, Q is the seismic quality factor, and α denotes the material's reference velocity P-wave velocity at the central frequency ω_0 (Aki and Richards, 2002). The real part of complex-valued seismic wavenumber k^* is a function of α' while the imaginary part is the attenuation component and depends on α' and Q as follows:

$$k^* = \frac{\omega}{\alpha'} - \frac{\omega}{2Q\alpha'} i \quad (4.2)$$

When seismic energy traveling through the subsurface encounters a contrast in material properties, the energy is partitioned at that interface and some of the energy is reflected back to the surface. We use k^* and ρ to compute the acoustic reflection and transmission coefficients for upgoing and downgoing energy at an interface assuming waves impinging at normal incidence on planar, flat-lying layers composed of homogeneous linearly elastic materials separated by a welded interface.

The reflectivity method uses those coefficients to calculate the reflectivity response from the uppermost boundary (R_1) in a series of stacked layers by calculating the reflectivity response starting at the lowermost layer first and recursively thereafter at each successively higher boundary following Muller (1985):

$$\mathrm{MT_i} = \mathrm{MB_i} e^{-2ik_i^* d_i} \tag{4.3}$$

$$\mathrm{MB_i} = \mathrm{R_{i+1}^d} + \frac{\mathrm{T_{i+1}^d T_{i+1}^u MT_{i+1}}}{1-\mathrm{R_{i+1}^u MT_{i+1}}} \qquad i= n\text{-}1,\ n\text{-}2,\ldots \tag{4.4}$$

where d_i is layer thickness and superscripts *d* and *u* denote upgoing and downgoing coefficients. We use the appropriate equations to calculate the downgoing reflection coefficient and upgoing and downgoing transmission coefficients (e.g., T_i) at any boundary. For example, R_i^d denotes the reflection coefficient for a downgoing wave at a boundary as follows:

$$R_i^d = \frac{\rho_{i+1}k_i^* - \rho_i k_{i+1}^*}{\rho_{i+1}k_i^* + \rho_i k_{i+1}^*} \tag{4.5}$$

where *i* denotes layer number. The resulting reflectivity from the total stack models that which we observe at the surface. It is the exact analytical response including multiples, scattering, and transmission effects:

$$R_1 = MB_0 \tag{4.6}$$

We then convolve R_1 with a source spectrum. After transforming the result to the time domain with an inverse Fourier transform, the final model result is a simulated seismic reflection series from the layer stack that includes all multiples.

Inversion

The inversion algorithm uses a Nelder-Mead simplex search to minimize the objective function ϕ with respect to user-defined parameters (Babcock and Bradford, 2014a; Lagarias et al., 1998). The objective function minimizes the misfit between the data and the computed model as follows:

$$\varphi = \sum (d_{obs} - d_{calc})^2 \tag{4.7}$$

where d_{obs} is the data and d_{calc} is the reflectivity response calculated using the 1D forward model discussed in the previous section.

We use a Monte-Carlo scheme to initialize starting values from a random distribution bounded by physically realistic limits for each parameter. The inversion parameters may consist of any subset of the input model parameters. In the 3-layer case, each layer has 4 parameters (α, Q, ρ, and d) for a total of 12 parameters. We can invert for any subset of these parameters. The algorithm then uses the gradient-based search around the user-defined parameters to find a local minimum (ϕ_{LM}) for each iteration. We repeat the minimization routine 1000 times for each example and calculate the mean (x) for each parameter from the subset of global minima (ϕ_{GM}).

We estimate uncertainty by evaluating equation 4.4 for 10,000 parameter pairs around the global minimum and then computing the root mean square error (RMS) for those pairs. The subset of paired solutions that fit the data within a 5% noise level define the solution. We report errors for the following solution pairs: α,ρ; α,Q; and α,d. While this method does provide an easily-visualized estimate of uncertainty, note that the solution space is multi-dimensional and thus the 2-dimensional uncertainty calculations do not entirely constrain the solution space.

Field Site

Bench Glacier is a temperate glacier located near Valdez, Alaska, in the coastal Chugach mountain range (Figure 4.1). The glacier's convenient location and moderate slope (<10°) have made it a conducive field site for multiple campaigns (e.g., Bradford et al., 2013; Brown et al., 2009; Harper et al., 2010; Fudge et al., 2008; MacGregor et al., 2005; Mikesell et al., 2012; Nolan and Echelmeyer, 1999; Riihimaki et al., 2005). Bench

Glacier is approximately 7-8 km long and 1 km wide. (Anderson et al., 2004; Bradford et al., 2009; MacGregor et al., 2005). Ice thickness ranges from 150 – 185 m (Brown et al., 2009; Riihimaki et al., 2005).

Mafic and ultramafic rocks are the major components of the geology of the Chugach Mountains (Burns et al., 1991). The bedrock of Bench Glacier is part of the Valdez Group (MacGregor et al., 2005). This lithology is characterized by meta-greywacke, which is dominated by quartz and feldspars (Winkler et al., 1980). Representative seismic attributes for this bedrock include α = 5400 – 6300 m s^{-1}, ρ = 2.68 – 2.71 kg m^{-3}, and Q = 200 - 1500 (Fowler, 1990; Press, 1966). P-wave velocities reported for Bench Glacier range from 3630 to 3780 m s^{-1} (Bradford et al., 2013; Mikesell et al., 2012). The ice velocity show weak, azimuthal anisotropy due to an extensive crevasse system (Bradford et al., 2013). Mikesell et al. (2013) report mean ice Q = 42 ± 28 from Rayleigh waves at a central frequency (f_0) of 45 Hz. We assume bulk glacier density to be 917 kg m^{-3} (Petrenko and Whitworth, 1999).

Climate records at Thompson Pass, approximately 10 km north of the glacier, indicate a mean annual air temperature (MAAT) of -2.2° C and a mean air temperature(MAT) of +6.2° C from May through September (Brown et al., 2009). (Refer to Brown et al. (2009) for a more detailed summary of climatic data.) Extensive borehole data show that the entire glacier is near the pressure melting point (PMP). Water may remain unfrozen throughout the glacier except perhaps near the surface during cold weather (Brown et al., 2009). Bradford et al. (2013) report bulk volumetric water content < 1%.

Previous seismic surveys have uncovered the possible presence of a discontinuous basal layer beneath Bench Glacier. A 2D seismic profile collected in 2007 highlights the presence of a layer that thins in the cross-glacier direction (Figure 4.2c). The reflection profile demonstrates an additional reflection separating from the bed arrival starting at common depth point (CDP) 80. This layer pinches out around CDP 150 indicating the presence of a discontinuous or thinning basal layer. Previous researchers have conjectured that the glacier may be hard-bedded or have possible discontinuous sediment present at the bed ranging from 1 -2 m thick (Fudge et al., 2009; MacGregor et al., 2005). It is also possible that there is a layer of debris-rich basal ice similar to other glaciers in this region (Hart, 1995). With that in mind, we apply the FWI to a discrete set of data co-located with the 2D survey to determine what this basal layer could be.

Data Collection

We conducted a seismic survey in summer 2007 using an 8 kg manual jackhammer source in a 10 x 10 m shot grid over a 300 x 300 m surface area (Figure 4.1). The resulting 3D P-wave seismic reflection profile had a checkerboard receiver pattern (40 Hz vertical geophones) in 4, 5x5m grids. The nominal CMP bin size is 2.5m, and CMP fold in our area of interest ranges from about 50 to 70 (Figure 4.1). Maximum offset was 384 m. The lack of snow or firn cover at the glacier surface during the data collection period allowed for effective source coupling but also caused some receiver coupling problems as receiver locations melted out of the ice over the course of a day of data collection and had to be reset.

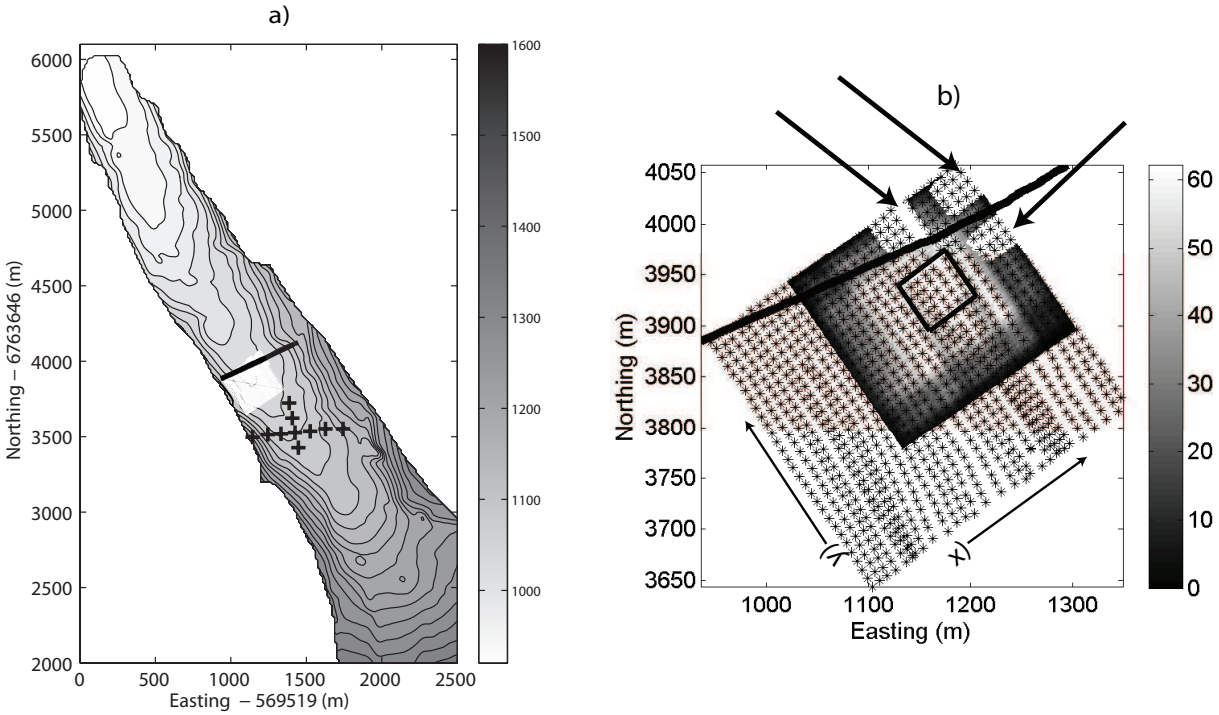

Figure 4.1: a) Bench Glacier, Alaska showing location of 3D seismic survey (white box) and surface seismic monitoring station locations (+) where Mikesell et al. (2012) report surface ice velocities and *Q* values; 20 m contour lines show bed elevation. Black line intersecting 3D survey area is location of 2D seismic profile shown in Figure 4.2c. b) 3D survey map with grey-scale fold density (lighter shade indicates higher fold) showing trace locations for inversion within the box in area of highest fold; x and y directions marked on plot correspond to those in Figures 4.5 and 4.6 with x_0,y_0 at lower left corner of inversion box. * indicates source locations and arrows point to white boxes enclosing receiver locations.

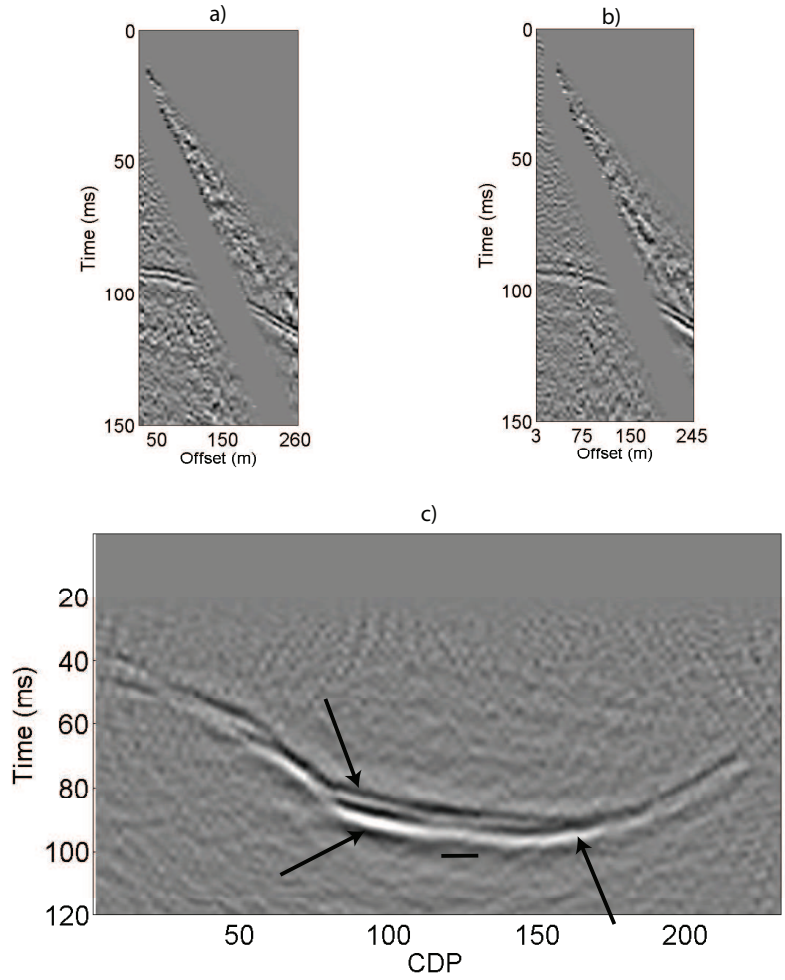

Figure 4.2: Data from Bench Glacier, Alaska: a) and b) show 2 representative supergathers with binned offsets as discussed in text. For viewing purposes these data have automatic gain applied with a 50 ms sliding window. c) Time-migrated 2D seismic profile across the survey area (solid line in Figure 4.2a and b). Note change in reflection characteristics across the length of the bed: arrows on left point to the peaks of two reflection events that converge across the glacier to the point marked by third arrow. At ice velocity, the maximum peak-to-peak distance closest to our survey is 8 m, or about 55%λ. Black line underscores region of seismic profile corresponding to inversion traces.

Data Processing

Basic processing steps include killing unusable traces caused by receiver melt-out or other problems, muting the Rayleigh wave, employing elevation statics, as well as

applying a bandpass filter (50-100-400-600 Hz) and a geometric spreading correction (t^1). Following Bradford et al. (2013), in the area of greatest fold we created 3D supergathers by combining 3 x 3 groups of binned CMPs. Nominal bin size was 7.5 m^2 and thus reflections in any given supergather represent a possible subsurface area of approximately 56 m^2. To further reduce noise, after NMO velocity analysis we combined and stacked offsets in 5 m increments for offsets less than 80 m. Constraining offsets to this range limits stretch effects in NMO processing and reduces problems associated with the azimuthal anisotropy known to exist in this glacier ice. Figure 4.2 shows representative supergathers.

Testing

A key step to implementing any full-waveform inversion algorithm is accurately characterizing the effective source wavelet. With that in mind, we begin by delineating steps to recover the effective source parameters from the direct arrivals in the seismic data collected at Bench Glacier. Next we use that source function within the reflectivity model to generate synthetic models simulating four different basal conditions that could generate the reflection event seen in Figure 4.2c. One model is a control simulating glacier ice overlying bedrock. The other three model a thin layer of basal sediment, a thin layer of basal water, and a basal layer of debris-rich ice. We subsequently test the inversion algorithm on recovering the model parameters. Finally, we implement the inversion algorithm on the field data collected at Bench Glacier to quantify its basal properties.

Source Recovery

Before we can test the inversion algorithm on either synthetic or field seismic data, we must accurately recover the source parameters. We use the direct arrivals from the seismic data set to derive the effective source parameters as follows. Visual examination of the data and comparison with results from Mikesell et al. (2013) reveals that the direct P-wave arrivals are well separated from the Rayleigh wave after about 50 m of offset. Therefore, we select offsets ranging from 50 to 75 m from which to extract the source wavelet characteristics. After basic processing steps as listed above, we apply a linear moveout (LMO) correction at an average velocity of 3640 m s^{-1}. Although lower than the bulk ice velocity, this velocity proved effective at flattening the direct arrivals. Surface velocity could be lower than bulk velocity due to a higher fracture concentration of crevasses and other heterogeneities near the surface. Finally, we stacked all traces within each offset bin to produce a single representative trace containing the direct P-wave arrival for a given offset (Figure 4.3).

After correcting for spherical divergence, we invert for seismic *Q* using a version of the primary gradient-based search algorithm. In this case, the objective function ϕ minimizes the differences between the five traces after back-propagation and attenuation (*Q*) correction as follows:

$$\phi = \sum_{i=1}^{5}(4P_i - [\boldsymbol{R} \subset \boldsymbol{P} | P_i \notin \boldsymbol{R}]\boldsymbol{j})^2 \quad (4.8)$$

where $\boldsymbol{P}$ is a matrix of 5 column vectors each composed of one back-propagated and attenuation-corrected waveform P_i, i denotes a column of $\boldsymbol{P}$, and $\boldsymbol{j}$ denotes the row-wise sum of the matrix **R** formed from **P**. We calculate the back-propagated and attenuation-

corrected waveform P_i for each of the 5 source wavelets (S_i) using the Fourier transform of the direct arrivals shown in Figure 4.3:

$$P_i = FFT(S_i)e^{\frac{i\omega x}{a'}+\frac{\omega x}{2a'Q}} \quad (4.9)$$

Thus, this technique inverts for the seismic attenuation factor by using equation 4.9 to minimize equation 4.8 with respect to Q. We calculate the solution uncertainty for the single inversion parameter as those Q values having RMS error ≤ 5%.

Source Results

The source parameter inversion returns $Q = 26 \pm 6$. The result is within the range for Bench Glacier surface Q values calculated by Mikesell et al. (2013) but 40% lower than their average value. However, their survey is located slightly up-glacier from our data collection region (Figure 4.1). In addition, Mikesell et al. (2013) used low-frequency Rayleigh waves rather than the higher-frequency P-wave direct arrivals and thus the representative volume of their Q measurement include deeper ice than the surface waves. Surface ice Q (Q_{ice}) should be lower than bulk Q_{ice} since attenuation is likely to be greater near the surface due to scattering caused by surface topography and air filled crevasses. Furthermore, ice Q is known to vary widely in response to ice conditions and temperature: i.e. Gusmeroli et al. (2010) report a range for Q_{ice} from 6 – 175 for temperate ice. With these considerations defending the reasonableness of our inversion Q result, we apply this Q to all 5 traces after spherical divergence correction, take the mean, and input the resulting spectrum as the source spectrum for the 1D reflectivity model (Figure 4.3).

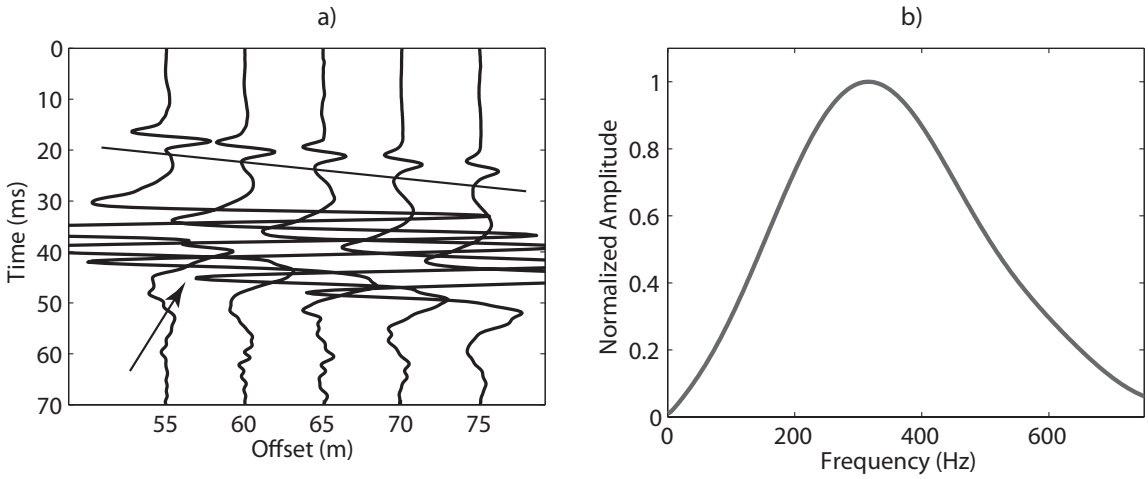

Figure 4.3: a) Seismic record for stacked traces binned between 55 and 75 m offset; straight solid line underscores direct arrivals and arrow points to Rayleigh waves; b) extracted source wavelet spectrum.

Synthetic Testing

Models

We use the 1D reflectivity model to produce four synthetic seismic traces which serve as a basis for inversion testing. We add 5% random Gaussian noise to each model before inversion. The models simulate 4 different basal conditions that could contribute to the reflection event observed in Figure 4.2: 1) glacier ice overlying bedrock; 2) a thin layer of sediment between the ice and bedrock; 3) a thin layer of water at the bed of the glacier; and 4) an underlying layer of frozen unconsolidated glacier debris. Model 1 acts as a control where layer 2 thickness was set to 0 and thus the model reflection comes from the layer 1/layer 3 boundary. Table 4.2 gives parameters used in model testing based on representative literature values from several sources including Booth et al. (2013), Johansen et al. (2003), Mikesell et al. (2012), Smith (2007), and Press (1966). Layer 2 α, Q, ρ, and d are the user-defined inversion parameters. We also input the overburden thickness l as an inversion parameter. We derive uncertainties from parameter

pairs as described in the inversion methods. Finally, we test Model 2 for 6 different layer thicknesses in order to demonstrate inversion robustness.

Table 4.2: Model parameters: Model 1 simulates a hard bed; Model 2 simulates a thin layer of basal till; Model 3 simulates water at the bed of the glacier; Model 4 simulates a basal ice layer. Layers 1 and 3 are the same for all models. Note that *d* is also given as %λ.

Model	Layer # and Fill	α (m s^{-1})	ρ (kg m^{-3})	Q	d (m)
	1, ice	3690	917	50	165
1	2, NA	NA	NA	NA	0 (NA)
2	2, saturated till	2000	2100	256	2.0 (25%λ)
3	2, water	1500	1000	1000	1.0 (17%λ)
4	2, basal ice	4000	2000	200	4.0 (25%λ)
	3, bedrock	5400	2700	500	100

Parameter Sensitivity Testing: Sediment Layer Thickness

In order to test the sensitivity of the inversion algorithm to sedimentary layer thickness, we generate 6 additional models with sediment thickness (d_{sed}) from 0.2 m (1/40λ) to 4 m (½λ) thick. Following Bradford and Babcock (2014b), for this test we hold other parameters constant having values as shown in Table 4.3 and define d_{sed} as the sole inversion parameter. We estimate 1D solution uncertainty as described for source Q inversion uncertainty estimates previously.

Synthetic Results

Model 1

Although we generated the model with d_2 = 0 m, as with the other models we inverted for layer 2 properties as if a thin layer were present. The inversion algorithm

returned $d = 0.05 \pm 0.05$ m, layer $\alpha = 2400 \pm 800$ m s^{-1}, $Q = 1 \pm 1$, and $\rho = 2200 \pm 700$ kg m^{-3} (Table 4.3). While solution α and ρ fall near acceptable values for glacial sediment (Table 4.1), the solution d is negligible when compared to the wavelength ($d = 1/200\lambda$ at $\alpha = 2500$ m s^{-1}). This solution d is likely the result of the inversion algorithm fitting some of the noise in the trace. Thus, this inversion test provides confirmation that the algorithm performs well in the model case simulating no thin layer present at the bed.

For this model, examination of parameter pairs did not produce any meaningful assessment of solution uncertainty. This problem could arise when parameter coupling is too complicated to be resolved with 2D solution appraisal. Therefore, here we estimated solution uncertainty from the subset of the 1000 inversion iterations where ϕ_{LM} was within 5% of ϕ_{GM}. This method for estimating solution uncertainty gives reasonable constraints on the inversion solution for this model (Table 4.3).

Models 2, 3 and 4

Inversion results for thin-layer parameters are within 5% of the true values for the remaining models with the exception of solution d for Model 3 and of solution Q (Table 4.3). Error in solution d for Model 3 is 10%, while all solution Q values appear unreasonable. Estimated solution uncertainty for both α and ρ is large in some cases, with estimated coefficient of variations (cv) ranging from 5% to a high of 25% for Model 4 (Table 4.3). On the other hand, uncertainty estimates for model Q are unreasonably low ($cv < 3\%$). This cv is likely not a reliable representation of Q uncertainty especially given the fact that Q results are well outside model parameters.

Parameter Sensitivity Testing

Figure 4.4 shows model traces and bounded solutions for 6 different test cases of sediment thickness. Table 4.4 reports associated uncertainties and *cv* for each result. The inversion performs remarkably well even when $d_{sed} = 1/40\lambda$, and all inversion solutions are within 5% of the true value. In all cases, the inversion solution underestimates layer thickness. Estimated uncertainty increases ($cv_{max} > 50\%$) as d_{sed} decreases from the Model A through Model F.

Summary of Model Results

The inversion solution for layer parameters except *Q* during synthetic testing was within 5% of true values for the four models with the exception of the erroneously low value for Model 3 *d*. In the control model example, solution *d* is extremely small ($\leq .05$ m), and it is obvious that in reality layer 2 is negligible (Table 4.3). For Models 2, 3, and 4, other than solution *Q* the estimated parameter uncertainties encompass the true model values. Associated uncertainties for several layer properties were high, notably in the case of ρ and α for Model 1 ($cv \cong 30\%$) and Model 4 ($cv \cong 25\%$). This result highlights the problem of non-uniqueness inherent in effective implementation of FWI. However, since the solution space is 4-dimensional, absolute estimation of uncertainty requires 4-dimensional analysis of the solution space, which we have not attempted.

The relative uncertainties associated with the results for α and ρ are twice that of corresponding uncertainties reported with previous use of this inversion algorithm (Babcock and Bradford, 2014b). However, those results were taken from radar data. In radar data, with certain assumptions, contrasts in permittivity provide reflectivity response. In our model, there are two primary reflectivity parameters (ρ, α) instead of

one. The coupled nature of this problem exacerbates the difficulty of solution non-uniqueness and thereby likely causes the large uncertainties that we report here.

On the other hand, solution *Q* is inaccurate for all model testing. For Models 2 and 3, solution *Q* is over 200% of the true *Q* and associated uncertainties for *Q* are unreasonably low. For Model 4, solution *Q* is 15% of the true value. Thus the model testing demonstrates that the inversion algorithm is not sensitive to layer *Q* for these layers and thicknesses and that reasonable constraints on *Q* values for the bounded inversion may be necessary in order to produce physically meaningful inversion results. Holding *Q* fixed during the inversion may prove a better option since using fewer inversion parameters will increase inversion speed. Additional model *Q* testing could possibly provide more comprehension concerning the implications of paired solution non-uniqueness. Overall, the preceding model results contribute to user comprehension both of the functionality and also of the limitations inherent in this FWI algorithm. Thus we can reasonably expect that this inversion algorithm can recover the basal properties of a glacier in the presence of a thin layer.

Table 4.3: Thin layer parameters for model testing and the inversion mean for Layer 2 parameters calculated from all results for ϕ_{GM}. Uncertainties reported for *Q* and *d* are estimated from *α*, *Q* and *α*, *d* pairs respectively, with the exception of Model 1 as noted in the text.

a) Model 1 (control)

Parameter	True Value	Solution	Bounds
α (m s^{-1})	NA	2400 ± 800	1000 - 5400
ρ (kg m^{-3})	NA	2200 ± 700	900 - 2700
Q	NA	1 ± 1	1 - 500
d (m)	0	0.05 ± 0.05	0 - 5

b) Model 2 (sediment)

Parameter	True Value	Solution	Bounds
α (m s^{-1})	2000	2100 ± 300	1000 - 5400
ρ (kg m^{-3})	2100	2000 ± 100	900 - 2700
Q	256	500 ± 10	1 - 500
d (m)	2.0	2.1 ± 0.3	0 - 5

c) Model 3 (water)

Parameter	True Values	Solution	Bounds
α (m s^{-1})	1500	1400 ± 100	1000 - 5400
ρ (kg m^{-3})	1000	1000 ± 100	900 - 2700
Q	1000	2500 ± 200	1-2500
d (m)	1.0	0.9 ± 0.1	0 – 5

d) Model 4 (basal ice layer)

Parameter	True Values	Solution	Bounds
α (m s^{-1})	4000	4000 ± 1000	1000 - 5400
ρ (kg m^{-3})	2000	2100 ± 500	900 - 2700
Q	200	30 ± 1	1-500
d (m)	4.0	4 ± 1	0 – 20

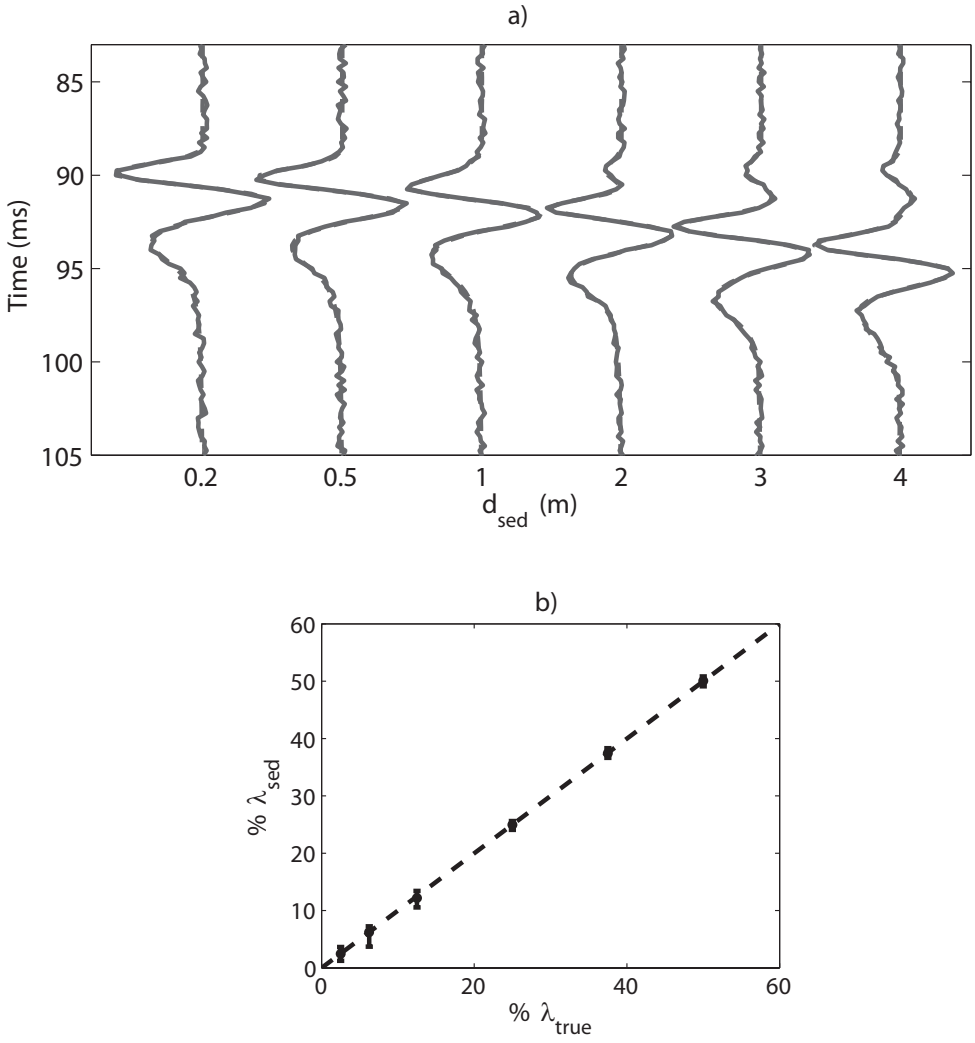

Figure 4.4: Results for parameter sensitivity testing with Model 2: a) shows the 6 models with increasing layer thickness from left to right. Dashed line is model with 5% added Gaussian noise, and thin solid line indicates inversion solution. All traces are normalized by the maximum source amplitude. b) Inversion solution for d_{sed} versus true model d and estimated solution uncertainties. Uncertainties for lower layer thicknesses are 25 times greater than the uncertainty associated with thickest layer which is not evident in plot (see Table 4.4).

Table 4.4: Results for parameter sensitivity testing for 6 models with increasing d_{sed}; the coefficient of variation (cv), which is the standard deviation divided by the mean, describes the relative uncertainties. Uncertainty associated with smallest value for d_{sed} is over 25 times greater than for the thickest layer tested. These results demonstrate the robustness of the inversion but also the caution needed in interpreting very thin layer results.

Model	A	B	C	D	E	F
d_{true} (m)	0.2	0.5	1.0	2.0	3.0	4.0
d_{sed} (m)	0.19 ± 0.1	0.49 ± 0.1	0.97 ± 0.12	1.99 ± .07	3.0 ± 0.07	3.98 ± 0.08
cv	52.6%	20.4%	12%	3.5%	2.3%	2%

Data Testing

After basic processing steps, we select 25 supergather formations in the area of greatest fold (Figure 4.2). Based on bin size, geometry, and estimating the size of the Fresnel zone, these traces cover about 62 x 62 m, or approximately 4000 m^2 which is about 0.05% of the total glacial area. In this small area, the basal geometry is relatively flat and we can reliably perform NMO velocity analysis. We limit incidence angles to those below 15° so that the normal incidence assumption is valid and to minimize effects associated with azimuthal anisoptropy. After NMO correction using α = 3690 m s^{-1}, we stack the traces within each supergather. The result is a single trace per supergather formation simulating a zero-offset seismic reflection event (Figure 4.5). We implement the inversion on each of the 25 traces after target windowing around the basal reflection event following Babcock and Bradford (2014b).

User-defined inversion parameters are α, ρ, d, and overburden Q (Q_{ice}). We invert for Q_{ice} instead of layer Q for three reasons: 1) the impact of Q_{ice} on wavelet attenuation is greater than that of layer Q since the wave's travel path in the ice is over 300 m as

compared to an estimated maximum thin-layer travel path of 4 m (Fudge et al., 2009); and 2) effective Q_{ice} is not well-known as robust estimates for Q_{ice} on Bench Glacier are surface-derived measurements and do not reflect bulk Q_{ice} over the ice volume which our inversion traces sample; and 3) model testing demonstrated inversion insensitivity to thin layer Q. Overburden thickness also functions as an inversion parameter. We use the source spectrum derived from the direct arrivals for the source in the 1D reflectivity model as described previously (Figure 4.3).

Data Results

Mean results for the inversion parameters over the whole inversion area (box, Figure 4.1) are $\alpha = 4000 \pm 700$ m s^{-1}, $\rho = 1900 \pm 200$ kg m^{-3}, $d = 6 \pm 1.5$ m, and $Q_{ice} = 68 \pm 21$ (Table 4.5). We refer to these values as the total solution. For visualization purposes, Figure 4.5 shows 5 traces and the corresponding inversion solutions. Total ranges for the 25 inversion solutions are 3200 – 4700 m s^{-1} for α, 1700 – 2400 kg m^{-3} for ρ, 2 – 9 m for d, and 50 – 100 for Q_{ice} (Table 4.5, Figure 4.6). Out of the 25 solutions, three have $d < 5$ m and two have $d > 7$ m, and the remaining solution d fall within 5 – 7 m. Similarly, if we exclude 2 solutions having $\rho \cong 2400$ kg m^{-3}, the total range of solutions for ρ becomes 1700 – 2100 kg m^{-3}. Excepting 2 high and low values noted in Table 4.5, solution α ranges from 3500 – 4200 m s^{-1}. The range of solutions for Q_{ice} exhibit more variability than the other 3 parameters with up to 100% variations in Q_{ice} depending on trace location (Figure 4.6). We calculate the paired parameter uncertainties as described previously for the 4 parameters for 5 of the 23 solutions. The total uncertainty for the mean solutions reported in Table 4.5 results from the average *cv* for each variable from those 5 paired solution uncertainties applied to the mean of the

solutions. Figure 4.7 shows the complicated nature of the paired uncertainties, especially for solution *Q*.

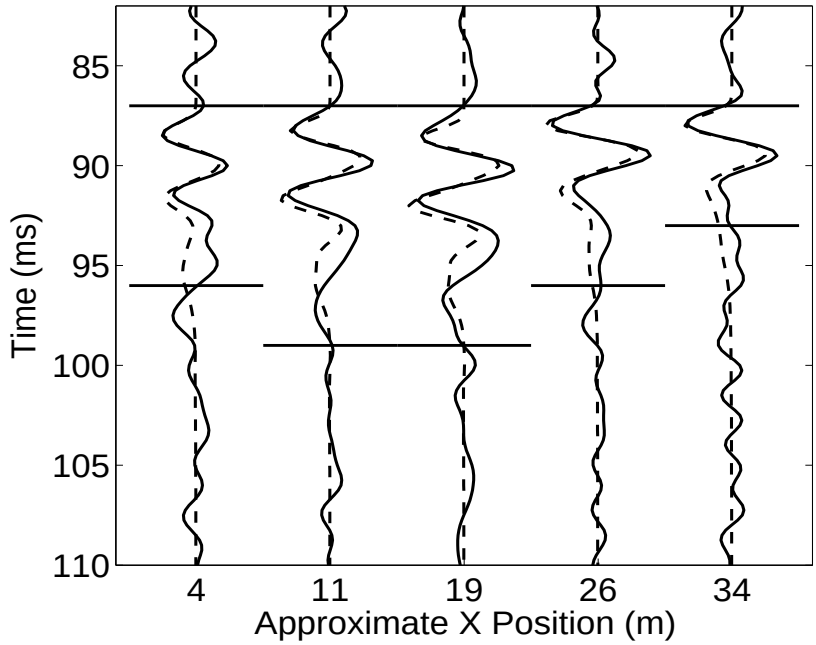

Figure 4.5: 5 representative supergather traces (solid line) and the inversion solution (dashed line) taken from approximately y = 4 m and x positions across the lower portion of the inversion box shown in Figure 4.1b. Horizontal solid lines define the target window for each trace and all traces are normalized by the maximum source amplitude. Target window choice depends on user discretion and is an essential consideration in the inversion process.

Table 4.5: Solution range and total mean solution with estimated uncertainty and inversion bounds for 25 supergather traces. Solution range is given without high and low outliers as discussed in text; values for those outliers are in parentheses.

Parameter	Total Solution	Solution Range	Inversion Bounds
α (m s^{-1})	4000 ± 700	3500 – 4200 (3200, 4700)	1200 – 5400
ρ (kg/m^3)	1900 ± 200	1700 – 2100 (2400)*	1000 - 2700
Q_{ice}	68 ± 21	50 - 100	26 – 100
d (m)	6 ± 1.5	5 – 7 (2**,8.5, 9)	0 - 20

* 2 solutions had $\rho \cong 2400$ kg/m^3

** 3 solutions had $d \cong 2$ m

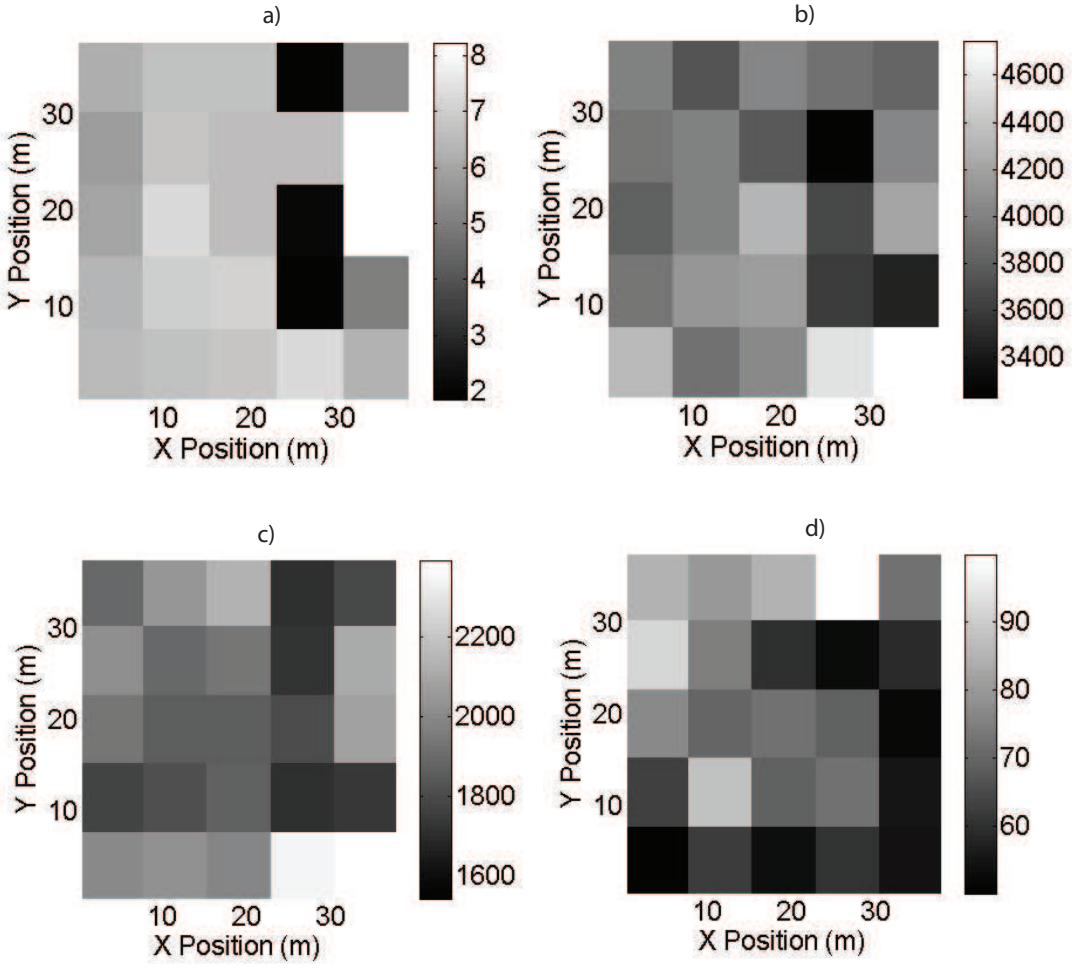

Figure 4.6: Solutions for 25 supergathers for a) layer *d* (m); b) α (m s^{-1}); c) ρ (kg m^3); and d) overburden *Q* (Q_{ice}); note scales for each plot, where x,y positions are relative to inversion box shown in Figure 4.2 starting at lower left corner. Mean estimated uncertainties are not shown but reported in Table 4.5. Each box represents the inversion solution for the appropriate variable from one stacked supergather as described in text.

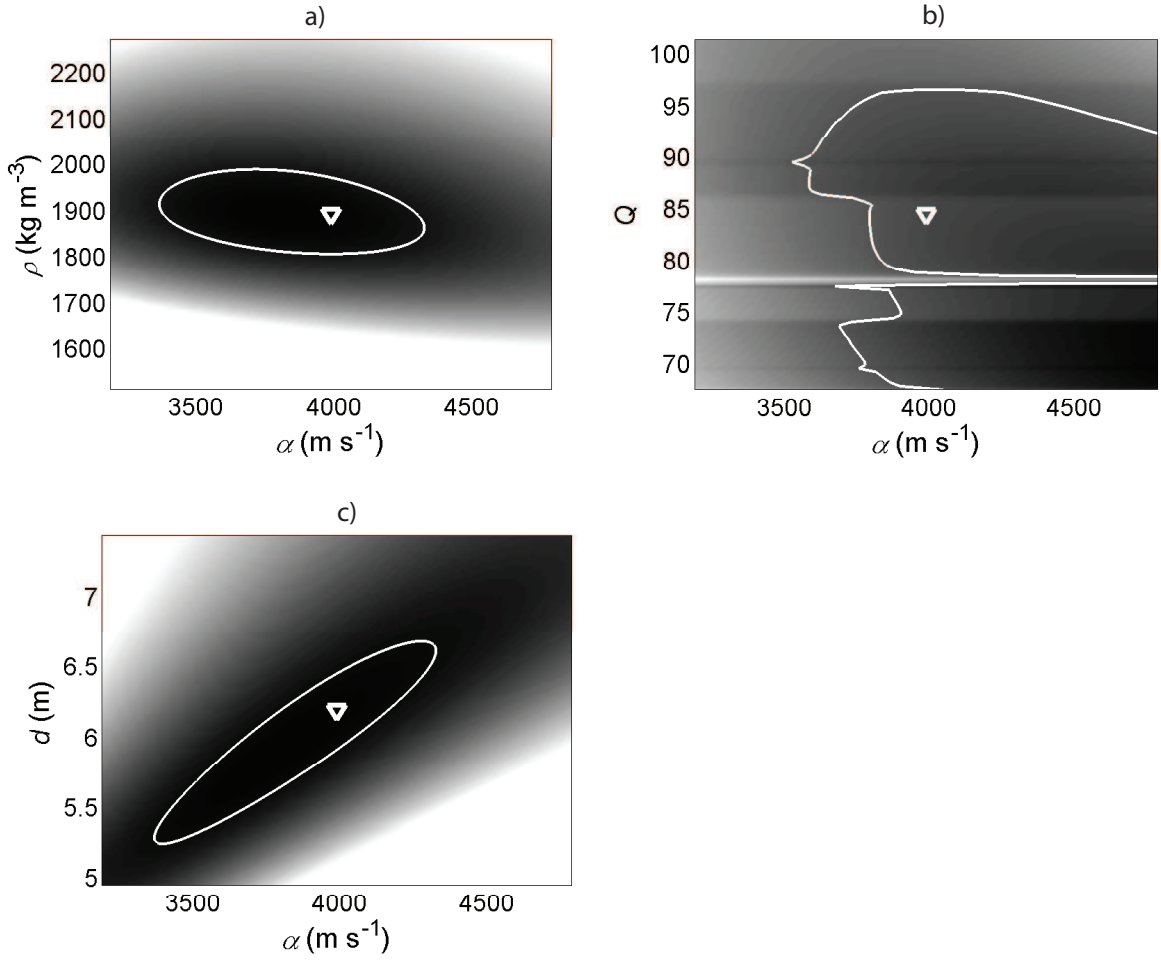

Figure 4.7: Demonstration of paired parameter solution uncertainty plots for 1 reference inversion solution for a) α (m s^{-1}) vs ρ (kg m^3); b) α vs Q_{ice}; and c) α vs *d* (m). Darker colors correspond to lower uncertainties and scale is relative to each parameter pair. White line encloses solutions from the parameter pair with RMS ≤ 5%, and triangle marks the inversion solution. In general other uncertainty plots show similar characteristics. Here α, Q_{ice} pairs (c) demonstrates the possibilities of multiple local minima with the concurrent difficulties such a situation poses for ill-constrained FWI problems.

Discussion

The total inversion solution for α (4000 ± 700 m s^{-1}) is within published ranges for debris-rich basal ice layers (BIL) or frozen sediments layers (e.g. 2300 - 5700 m s^{-1}) (Table 4.1 and Figure 4.6) (Johansen et al., 2003; McGinnis et al., 1973). The total slowness or velocity inverse(*s*, s m^{-1}) of the composite material is approximately the sum of the fraction *f* of each component times the slowness (Hauck et al., 2011):

$$s_{BIL} = s_i f_i + s_r f_r + s_a f_a + s_w f_w \quad (4.10)$$

where the subscripts *BIL*, *i*, *r*, *a*, and *w* denote basal ice layer, bulk ice, rock, air, and water respectively. We assume that the water content of the BIL is negligible since Bradford et al. (2013) determined the volumetric water content of Bench Glacier in our survey area to be <1%. We further assume that there is no void space in the BIL, i.e. f_a = 0. With these two simplifications, equation 4.10 reduces to a two-component mixing equation for slowness:

$$s_{BIL} = s_i f_i + s_r f_r. \quad (4.11)$$

where $f_i = 1 - f_r$. We can simplify and solve equation 4.11 for the rock fraction as follows:

$$f_r = \frac{s_{BIL} - s_i}{s_r - s_i}. \quad (4.12)$$

The corresponding slowness s_{BIL} = 2.5 x 10^{-4} s m^{-1} to the mean inversion velocity yields a rock fraction of 30%. Excluding outliers, the highest seismic velocity from the inversion is 4200 m s^{-1} (Table 4.5). This velocity corresponds a to rock fraction of 43%. Equation 4.12 fails where reported layer seismic velocities are less than ice velocity (α_{ice}) (i.e., layer slowness $s_{BIL} > s_i$). Solution α for two of the twenty-five inversion traces were below α_{ice}.

However, equation 4.12 does not take into account the geometry or distribution of the rock inclusions. Another source of error is our assumption that there is no free water in the BIL. Harper et al. (2010) show that water-filled basal crevasses are present on Bench Glacier. These observations combined with the timing of the data collection (August) suggest that water in liquid form is present throughout the glacier crevasse system. It is possible that BIL volumetric water content is as high as 2.5% (Bradford et al., 2009). Using the 3-phase approximation to equation 4.10 with f_w = 2.5% and f_i = 70%, the BIL bulk seismic velocity may be as low as 3700 m s^{-1} (Figure 4.6). This value is well within the uncertainty of the mean solution (Table 4.5).

The total inversion solution for ρ is 1900 ± 200 kg m^{-3} with the solution ranging from 1700 – 2000 kg m^{-3} excluding 1 outlier (Table 4.5). We use a common mixing equation to interpret these results with respect to rock fraction for the two phase system (Nolan and Echelmeyer, 1999):

$$\rho_{BIL} = f_r\rho_r + (1 - f_r)\rho_i. \quad (4.13)$$

Solving for f_r, the resulting rock fractions for the inversion results range from 40 – 65%. These values are within published ranges for debris-concentrations of debris-rich BIL layers (30 – 59%) (Hart, 1995; Hart and Waller, 1999). In addition, the robustness of the inversion solution is corroborated by the consistency of the rock fraction results from analysis of both α and ρ. Combined interpretation of the analysis for inversion solutions for α and ρ suggests that there is indeed a thin layer of debris-rich basal ice present below the glacier at this location. Given the range of solution ρ, this BIL likely has relatively high concentrations of debris (40 -65%). An alternative interpretation could be the presence of basal layers of saturated, frozen sediments with high-porosity.

However, such layers are not likely to form beneath a temperate glacier such as this one. The 2D seismic profile previously collected at our survey location corroborates our findings (Figure 4.2). Based on peak to peak time difference between arrivals of the thinning basal layer observed in the stacked data, the thickness of this layer nearest our survey area is approximately 8 m. The inversion result for d (6 ± 1.5 m) corresponds roughly to the center of the section where visual examination shows the basal layer is thinning out.

Next we interpret our results for overburden Q (Q = 68 ± 21). Overall the inversion solution for Q_{ice} falls well within reported literature values (e.g., Gusmeroli et al., 2010). Furthermore, our surface wave inversion, the model inversion results, and the bulk Q_{ice} inversion results all demonstrated that the inversion algorithm is not sensitive to Q for these high Q values. To test that observation, we reran the inversion for the entire set of 25 traces with Q_{ice} fixed and equal to the inversion mean solution (Q_{ice} = 68). The resulting mean inversion solutions deviated less than 5% from the solutions in Table 4.5 and the average run time was half the run time when including Q_{ice} as an inversion parameter. Thus we conclude that fixing Q_{ice} to a reasonable value based on some knowledge of overburden conditions has minimal impact on inversion accuracy and may prove a reasonable approach especially given the complicated nature of Q solution, which may trap the inversion in discrete local minima (Figure 4.7).

Finally, it is important to note that target window length is an inversion input based on user discretion. Babcock and Bradford (2014b) noted that a shorter window length may provide a more accurate inversion result than a longer one. Thus we attempt to define window length so as to include the entire reflection event but exclude noise

(Figure 4.5). Target window remains based on practitioner judgment; future work should include a more robust assessment of ideal target window.

Conclusions

We applied a full-waveform inversion algorithm to synthetic seismic data and to field data taken from Bench Glacier, Alaska, in an effort to quantify thin layer parameters for basal layers. The inversion implements a gradient-based search algorithm in conjunction with a 1D vertical incidence reflectivity model. The direct arrivals in the field data set provide an estimate of the effective source spectrum for the reflectivity model. During synthetic testing on 4 models with 5% added random Gaussian noise, the inversion recovered thin-layer parameters within 10% of true model values. Additionally, we tested the inversion on 6 different cases of d_{sed} from 1/40λ to ½λ. Inversion results for d_{sed} were within 5% of true model values. Finally, the FWI algorithm recovers mean α = 4000 ± 700 m s^{-1}, ρ = 1900 ± 200 kg m^{-3}, and d = 6 ± 1.5 m using a subset of field data collected during a glacier seismic survey. We interpret these results to be indications of the presence of a debris-rich basal ice layer at the sample locations.

Future work includes quantification of inversion sensitivity to seismic Q, investigation of the effects of window length on solution robustness, and implementation on additional data sets. Judicious implementation of this algorithm could quantify properties of thin layers under glaciers and ice sheets. Such accurate quantification of basal parameters will aid interpretation and modeling of glacier and ice sheet dynamics in response to climate change.

CHAPTER FIVE: ELECTRICAL ANISOTROPY IN SEA ICE AND A DUAL-POLARIZATION RADAR SYSTEM TO MITIGATE THE EFFECTS OF PREFERENTIAL ATTENUATION IN IMAGING SEA ICE

Abstract

Preferential alignment in the physical structure of the sea ice crystal matrix results in anisotropy in the electrical properties of the bulk sea ice. Analysis of a 1D reflectivity model and field data demonstrates that sea ice electrical anisotropy can impede ice profiling using ground penetrating radar (GPR) reflection methodology via preferential attenuation due to polarization effects. Depending on polarization, preferential attenuation due to anisotropy effects can reduce or eliminate ice bottom reflections. To facilitate reliable ice profiling, we describe a dual-polarization configuration of a commercial GPR system for ice monitoring. The dual-polarization system reliably images the sea ice/water interface even in the presence of well-developed conductivity anisotropy. Additionally, by combining data from both polarizations, our system provides information about the horizontal direction of the ice matrix alignment, which may indicate the direction of dominant current flow.

Introduction

Sea ice is well-known to be anisotropic both with respect to its mechanical, physical, and electrical properties (Campbell and Orange, 1974; Kovacs and Morey, 1979; Timco and Weeks, 2010). Even first-year sea ice is an “anisotropic, stratified,

strongly absorbing, inhomogeneous dielectric" with electrical and physical properties dependent on temperature, salinity, age, and crystal structure (Kovacs and Morey, 1978). Both the permittivity and conductivity structures of sea ice are anisotropic. In particular, the anisotropy in the conductivity structure of sea ice has ramifications for effective implementation of ground penetrating radar (GPR) to image the sea ice bottom.

The driving mechanism for sea ice conductivity is the salinity (Nakawo, 1981). As ice forms from sea water, growing ice crystals extrude salt. This salt may be expelled from the bottom of the growing ice sheet. Some extruded salt becomes trapped within the ice sheet and subsequently concentrated in brine pockets and channels. In general, these brine pockets are probably ellipsoidal or cylindrical (Figure 5.1) (Jones et al., 2010; Kovacs and Morey, 1986; Morey et al., 1984). Nevertheless, the volume fraction, size, shape, and connectivity of the brine inclusions vary over several orders of magnitude depending on environmental factors (Buchanan et al., 2011; Jones et al., 2010). The concentration of the brine within the inclusions depends largely on the rate of ice growth for early- or mid-season ice. Ice growth rates, in turn, depend on temperature and on the age of the ice (Jones et al., 2010).

The bulk effective conductivity of the ice sheet is a factor of the brine concentration and of the orientation of the brine inclusions. This orientation depends on the microstructure of the ice, which is generally either granular or columnar (Timco and Weeks, 2010). Granular ice has no preferential orientation and is usually isotropic. The conductivity of columnar ice, on the other hand, can be strongly anisotropic due to the preferential shape and orientation of the ice columns.

In the case of anisotropic columnar sea ice, elongated vertical columnar crystals extend throughout the ice sheet. The columns enclose brine pockets oriented perpendicularly to the c-axes of the crystals (Figure 5.1) (Kovacs et al., 1987). This vertically-oriented matrix of crystals and brine inclusions can additionally align in the horizontal direction in response to dominant ocean currents (Figure 5.1) (Campbell and Orange, 1974; Golden and Ackley, 1981; Kovacs and Morey, 1986; Tucker, 1984). The net result is that the conductivity (σ_{si}) and permittivity (ε_{si}) of the sea ice varies with azimuth. The magnitude of the azimuthal variation is a factor of ice temperature, volume of brine, the brine temperature and salinity, the properties of the ice crystals, and the shape of the brine inclusions.

In order to understand the implications of this anisotropy for imaging sea ice using radar in the GPR frequency range (10 MHz to 1 GHz), we begin by examining the relevant electrical properties of sea ice with respect to polarization. Then we discuss a data example that highlights the polarization-dependent response. Finally, we present a commercial radar system set-up that mitigates the effects of the sea ice anisotropy and allows us to reliably detect the ice bottom even when the ice is strongly anisotropic. Data collected at two field sites demonstrate the system's ability to reliably image the sea ice/water interface regardless of the preferential direction of the anisotropy.

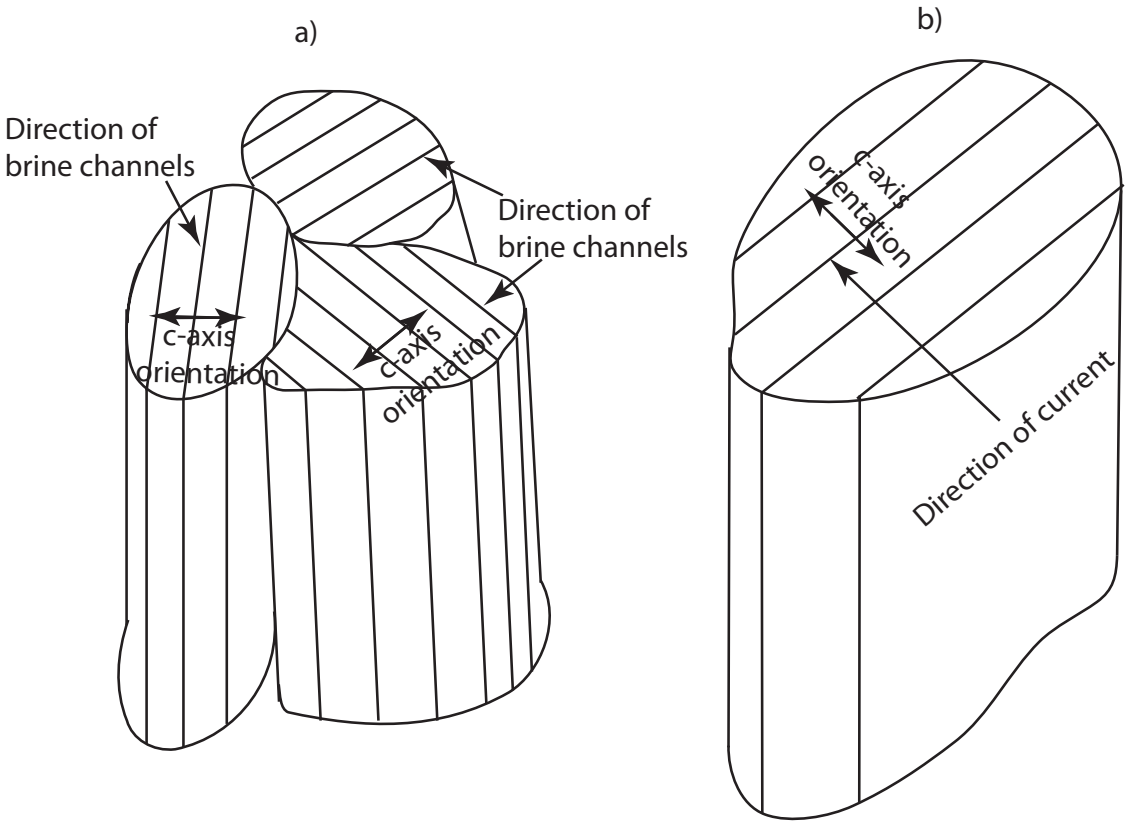

Figure 5.1: Sea ice crystals in columnar ice having a) oriented brine pockets with varying shape and size within randomly-oriented columnar ice crystal matrix and b) possible orientation of the columnar ice matrix in response to dominant currents (following Kovacs et al., 1987).

Sea Ice Electrical Anisotropy

Radar wave propagation in sea ice depends on both ε_{si} and σ_{si}. Since sea ice is strongly anisotropic, we treat the problem as two separate cases corresponding to the electromagnetic (EM) plane wave, **E**, polarized in the parallel ($\mathbf{E}_{\parallel}$) or perpendicular ($\mathbf{E}_{\perp}$) direction with respect to the dominant orientation of brine inclusions. Many commercial radar antennas are approximately horizontal dipoles and emit a linearly polarized **E** field. By choosing the appropriate coordinate system, we can write the two cases with respect to that orientation as follows (Morey et al., 1984):

$$\nabla^2 \mathbf{E}_{\parallel} - \mu_0 \sigma_{si\parallel} \frac{\partial \mathbf{E}_{\parallel}}{\partial t} - \mu_0 \varepsilon_{si\parallel} \frac{\partial^2 \mathbf{E}_{\parallel}}{\partial t^2} = \mathbf{J}_{\parallel} \quad (5.1)$$

$$\nabla^2 \mathbf{E}_{\perp} - \mu_0 \sigma_{si\perp} \frac{\partial \mathbf{E}_{\perp}}{\partial t} - \mu_0 \varepsilon_{si\perp} \frac{\partial^2 \mathbf{E}_{\perp}}{\partial t^2} = \mathbf{J}_{\perp} \quad (5.2)$$

where **J** is the source of **E** due to radar excitation, and ε_{si} and σ_{si} are polarization-dependent. (Since sea ice is nonmagnetic, we take μ to be constant and equal to the magnetic permeability of free space, μ_0.) Any case of **E** polarized at an intermediate orientation with respect to the dominant direction of the anisotropy may be decomposed into these two cases.

Taylor's (1965) mixing formulas provide the effective permittivity of the sea ice if the brine pockets are parallel to the introduced field ($\varepsilon^*_{si\parallel}$) or if they are perpendicular ($\varepsilon^*_{si\perp}$), given the complex permittivities of the brine and the pure ice crystals (ε^*_b and ε^*_i, respectively) and the volume fraction of the brine (v_b). These formulas require some additional assumptions about the shape and size of the brine pockets, namely that the long axes of the ellipsoidal pockets are small relative to the wavelength of the signal in the sea ice and that $v_b << 1$. These conditions are likely satisfied in cold sea ice (Jones et al., 2010). With these assumptions, we can calculate the complex-valued permittivities for the two-component system as follows (Morey et al., 1984):

$$\varepsilon^*_{si\parallel} = \varepsilon^*_i + \upsilon_b(\varepsilon^*_b - \varepsilon^*_i) \quad (5.3)$$

and

$$\varepsilon^*_{si\perp} = \frac{\varepsilon^*_i \varepsilon^*_b}{\varepsilon^*_b + \upsilon_b(\varepsilon^*_i - \varepsilon^*_b)} \quad (5.4)$$

Inspection of these two equations reveals the need to calculate the complex-valued ε_b^*, ε_i^*, and υ_b. The Debye (1929) formula provides the basis for computing complex-valued ε_b^* (Stogryn, 1971) and ε_i^* (Buchanan et al., 2011) as follows:

$$\varepsilon_i^* = \varepsilon_{i\infty} + \frac{\varepsilon_{i0} - \varepsilon_{i\infty}}{1 + i\omega\tau_i} \tag{5.5}$$

$$\varepsilon_b^* = \varepsilon_{b\infty} + \frac{\varepsilon_{b0} - \varepsilon_{b\infty}}{1 + i\omega\tau_b} + i\frac{\sigma_b}{\omega\varepsilon_c} \tag{5.6}$$

using the dominant relaxation time of the specific material (τ); the low frequency (ε_0) and high frequency (ε_∞) permittivity limits of the given material; the conductivity of the brine (σ_b); the permittivity of free space (ε_c); and $i = \sqrt{-1}$.

At radar frequencies, ε_i^* is essentially frequency- and temperature-independent ($\varepsilon_i^* \cong (3.14 + 0.002i)\varepsilon_c$) (Golden, 1995; Kovacs and Morey, 1986). On the other hand, ε_b^* depends strongly both on temperature and on frequency (Golden, 1995). Stogryn (1971) provides equations to calculate τ, ε_∞, and ε_0 for brine as a function of temperature (T). Brine conductivity (σ_b) also depends on T. Morey et al. (1984) discuss calculations of σ_b and the concurrent assumptions in detail.

Finally, estimating $\varepsilon_{si\parallel}^*$ and $\varepsilon_{si\perp}^*$ also requires calculating υ_b and ε_m^*. We follow the formulas provided by Frankenstein and Garner (1967) to compute υ_b as a function of temperature (T, °C) and the bulk salinity of the ice (S_{si}). At radar frequencies, the effective permittivity (ε_{ef}) is approximately equal to the real part of ε^* (Bradford, 2007; Knight and Endres, 2005). The differences between ε_{ef} in the parallel and perpendicular polarizations ($\varepsilon_{ef\parallel}$ and $\varepsilon_{ef\perp}$, respectively) is less than 17% for cold sea ice. The imaginary components of $\varepsilon_{si\parallel}^*$ and $\varepsilon_{si\perp}^*$ ($\varepsilon_{si\parallel}''$ and $\varepsilon_{si\perp}''$, respectively) contribute to the

cumulative effective conductivity of the sea ice in the parallel ($\sigma_{ef\parallel}$) or perpendicular ($\sigma_{ef\perp}$) polarization (Knight and Endres, 2005):

$$\sigma_{ef\parallel} = \sigma_{dc} + \omega\varepsilon''_{si\parallel} \tag{5.7}$$

$$\sigma_{ef\perp} = \sigma_{dc} + \omega\varepsilon''_{si\perp} \tag{5.8}$$

Following a modified Archie's law (Morey et al., 1984), σ_{dc} is a function of v_b and σ_b(Kovacs and Morey, 1986):

$$\sigma_{dc} = \sigma_b \upsilon_b^m \tag{5.9}$$

where *m* depends on polarization. Combining equations 5.3 through 5.9, we proceed as follows:

$$\sigma_{ef\parallel} = (0.5 + .02T)\sigma_{b,25}\upsilon_b^{1.55} + \omega\mathrm{Im}(\varepsilon_i^* + \upsilon_b(\varepsilon_b^* - \varepsilon_i^*)) \tag{5.10}$$

$$\sigma_{ef\perp} = (0.5 + 0.02T)\sigma_{b,25}\upsilon_b^{1.75} + \omega\mathrm{Im}(\varepsilon_i^* + 2\upsilon_b\left(\frac{\varepsilon_m^*(\varepsilon_b^* - \varepsilon_i^*)}{\varepsilon_m^* + \varepsilon_b^*}\right)) \tag{5.11}$$

The final result is that the net effective conductivity of the ice parallel to the preferential horizontal direction of the brine channels can be up to 2.5 times higher than the effective conductivity perpendicular to the channels, depending on temperature (Figure 5.2).

Both ε_{ef} and σ_{ef} contribute to the attenuation, α_{si}, of the radar wave in sea ice:

$$\alpha_{si} = \omega\sqrt{\frac{\mu\varepsilon_{ef}}{2}\left(\sqrt{1 + \left(\frac{\sigma_{ef}}{\varepsilon_{ef}\omega}\right)^2} - 1\right)}\,. \tag{5.12}$$

We substitute the appropriate variables corresponding to each polarization to calculate $\alpha_{si\perp}$ and $\alpha_{si\parallel}$ (Figure 5.2). The attenuation exponent increases with increasing σ_{ef}, and so $\alpha_{si\parallel}$ is greater than $\alpha_{si\perp}$. Thus the radar wave experiences preferential attenuation when aligned with the brine structure of the ice. The differences between $\alpha_{si\perp}$ and $\alpha_{si\parallel}$ are large at all temperatures ranging from -22°C ($\alpha_{si\parallel} \cong 10\alpha_{si\perp}$) to -2°C ($\alpha_{si\parallel} \cong 28\alpha_{si\perp}$) (Figure 5.2).

Finally, we use a 1D reflectivity model to model the polarization-dependent reflection of the radar wave from the sea ice/water interface (Bradford et al., 2010). The model results show that preferential polarization of the EM signal can reduce and even eradicate the ice bottom reflection event (Figure 5.2). Multiple published results corroborate the model predictions. For example, Kovacs and Morey(1978) experienced a complete absence of any measurable reflected signal from the ice bottom and attributed it to preferential attenuation. Similarly, Campbell and Orange (1974) monitored preferentially-extinguished ice bottom reflection events with changing azimuth. Nyland (2004) observed preferential attenuation of radar reflection amplitudes on sea ice in Alaska and warned that errors in ice velocity may result from difference between ε_{ef} in the two polarizations.

Data Example: Testing at CRREL

Materials and Methods

Site

We collected an example data set over a saline ice sheet grown in a control facility at the U. S. Army Cold Regions Research and Engineering Lab (CRREL) in New

Hampshire in 2011. The testing at CRREL was part of an ongoing campaign to verify the radar's ability to detect spilled oil in and under sea ice. For all CRREL testing, CRREL personnel grew a saline ice sheet in an outdoor concrete basin 18.25 m long by 6.7 m wide by 2 m deep. A refrigeration unit above the tank maintained the air temperature over the ice sheet at -15 °C during ice growth. We adjusted initial water salinity such that the final water salinity after ice growth would mimic sea water, approximately 32-34 parts per thousand (ppt). Surface ice temperatures during testing were -10 to -15° C. We collected data before and after a simulated oil spill event during the training exercise.

Acquisition

We collected data using Sensors and Software PulseEkko Pro 1 GHz shielded antennas. We processed and analyzed the data without foreknowledge of anisotropy structure, ice depth, or oil location. Basic processing steps included a dewow filter, time-zero correction, amplitude spreading corrections (t^1), background subtraction, and muting the first arrivals. Where applicable, we converted from time to depth using an approximate sea ice velocity of 0.15 m/ns.

Results

These data show a marked decrease in reflection amplitude from the sea ice bottom depending on polarization. The most likely cause of the missing reflection from the data in the cross-tank direction (Figure 5.2) is exponential decay due to attenuation of the radar energy polarized in alignment with the conductivity structure of the sea ice. This result shows that unintentional survey alignment with the preferential axis of the conductivity structure of sea ice can obscure or eliminate reflection response from the ice

bottom. In such cases, data analysis would not reliably reveal the ice/water interface. With that in mind, we present a system to reliably image the ice bottom even in the presence of strong anisotropy and regardless of the anisotropy direction.

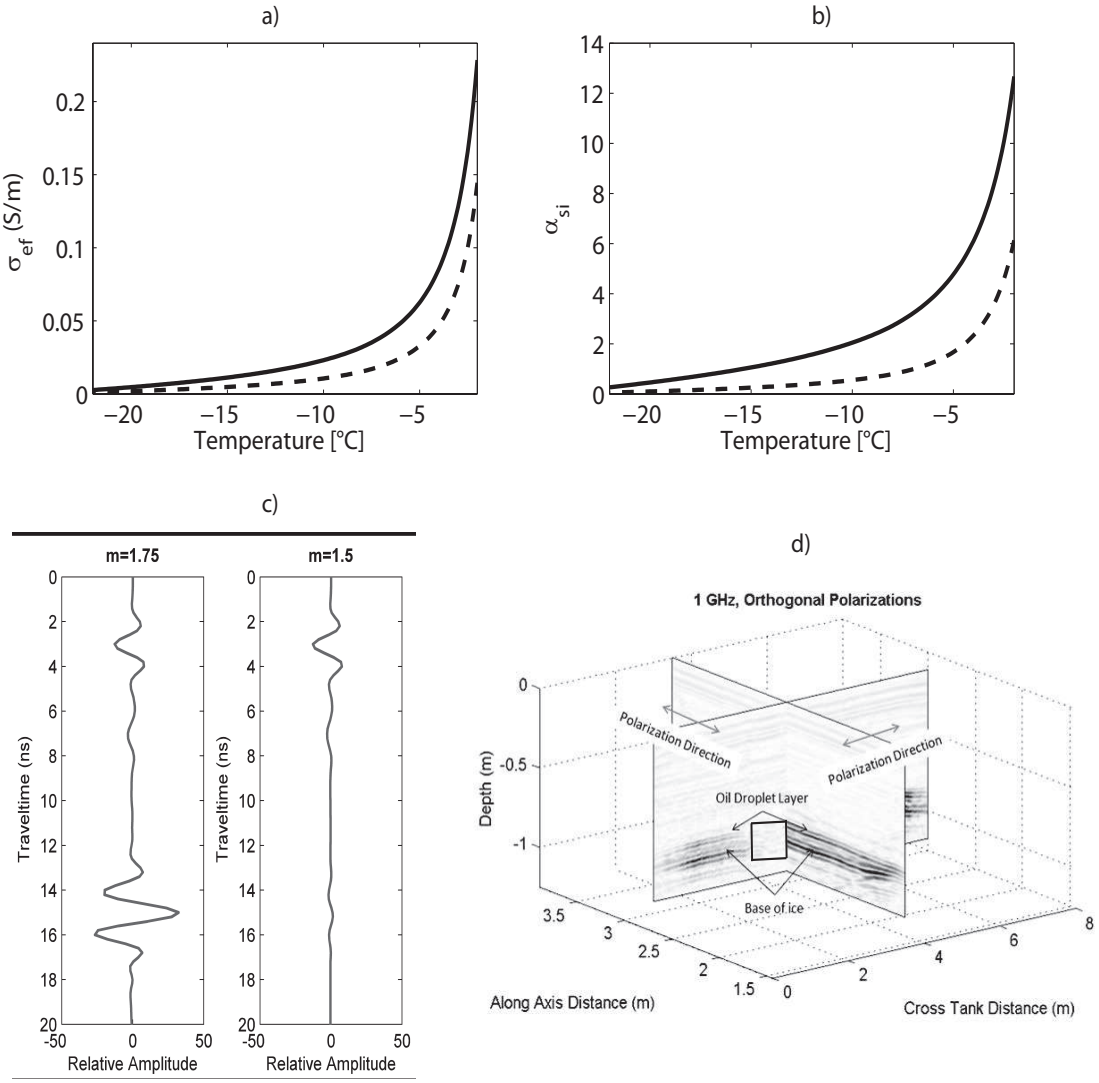

Figure 5.2: Demonstration of the modeled and real effects of sea ice anisotropy on radar data using 500 MHz central frequency, *n*=0.07, and parallel (solid) or perpendicular (dashed) polarizations: a) effective conductivity versus temperature; $\sigma_{si\parallel}$ is more than 2 times $\sigma_{si\perp}$ at all ice temperatures above -17 °C. b) calculated attenuation exponent α for each polarization; for sea ice at -2° C, $\alpha_{si\parallel}$is more than 2 times greater than $\alpha_{si\perp}$. c) 1D reflectivity model of ice bottom reflection with ice thickness 0.85 m (reflection at 12 ns). The left plot uses Archie's law exponent m=1.75 for antenna polarization perpendicular to primary crystal orientation; plot

on right uses m=1.5 for parallel polarization; in this case reflection strength from ice/oil/water interface is reduced by a factor of 85. d) 1 GHz pulsed radar data collected at CRREL in both polarizations. The almost-complete disappearance of the ice/oil interface and the ice-water interface in the cross-tank direction (rectangle) is likely a result of attenuation due to conductivity anisotropy.

Field System for Anisotropy Mitigation

Dual-Polarization Confirmation

We implement a new dual-polarization GPR system using 4 500-MHz Sensors and Software PulseEkko Pro shielded antennas. For this system, we orient one source-receiver pair in-line (parallel) with the survey direction and the other perpendicular (cross-line) to the survey direction. The system collects data alternately from the orthogonally-polarized antenna pairs across the length of the survey with spatial positioning controlled via odometer wheel (Figure 5.3). Data sets are collected simultaneously by the system, so the only difference between the parallel and perpendicular data sets is polarization direction. Since the antennas are orthogonally polarized, regardless of the preferential direction of the anisotropy structure at least one of the antenna-receiver pair should experience minimal attenuation and successfully image the sea ice bottom.

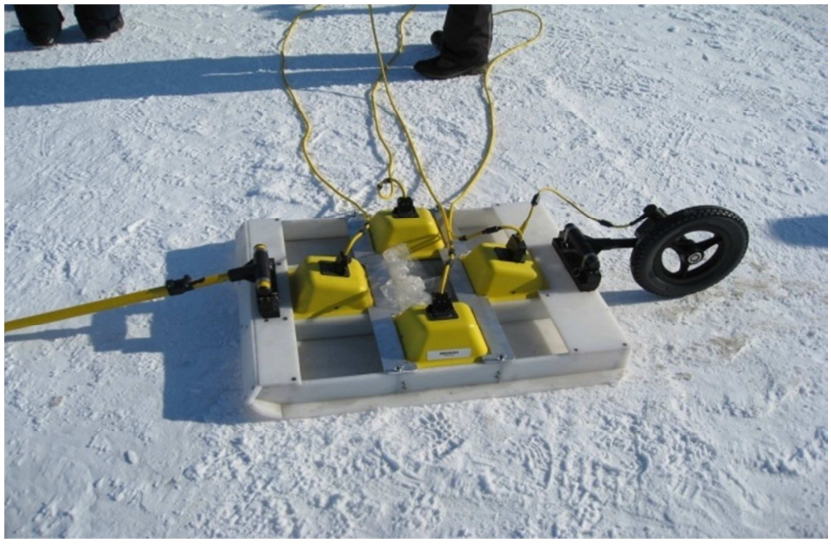

Figure 5.3: Dual-polarization system: 500 MHz antenna-receiver pairs oriented parallel and perpendicular to survey direction, as shown by orientation of odometer wheel travel.

We acquired data using the dual-polarization system at Prudhoe Bay, Alaska over natural sea ice in 2008. During the Prudhoe Bay testing, the clean mid-winter sea ice was approximately 1.5 m thick. Data for temperature and salinity of the ice at Prudhoe are limited, and no boreholes were drilled during the data collection to verify ice depth. In 2012, we tested the 500 MHz dual-polarization system in conjunction with training conducted by Alaska Clean Seas at CRREL for oil spill responders and relevant environmental agencies. The staff at CREEL grew the ice sheet as described in the previous section. Ice thickness was approximately 0.4 m, and we collected data after the simulated oil spill event during the training exercise.

For all tests using the dual-polarization system, we did not preplan survey direction with respect to any anticipated anisotropic response in the ice. We processed and analyzed the data without foreknowledge of ice depth or oil location, using the same processing steps as above. Additionally, using the dual-polarization data, we combined

the orthogonally-polarized data sets into one complete profile by vector sum. In using the vector sum to combine the data, we assume that the differences in travel time due to polarization are insignificant. We also assume that the reflection amplitude from the parallell-polarized phase ($R_{\parallel}$) is negligible. Contrary to Nyland's (2004) observation, in our data we see less than 0.1 ns differences in arrival times between the two polarizations and using the vector sum to combine the data proves reasonable. The small difference in arrival times validates our assumptions about $R_{\parallel}$.

Another advantage of the dual-polarization approach is the ability to determine the dominant direction and the relative strength of the anisotropy. After basic processing steps, we evaluate the maximum reflection strength of ice/water reflection event for both polarizations ($R_{\perp}$ and $R_{\parallel}$) averaged in 1 m increments across the length of the survey. Then, we compute the angle in degrees (θ) between two vectors with respect to the direction of travel, assuming $R_{\parallel} = 0$:

$$\theta = \tan^{-1} \frac{\max(R_{\perp})}{\max(R_{\parallel})} \tag{5.13}$$

Finally, we calculate the relative strength of the anisotropy as $\max(R_{\perp})/\max(R_{\parallel})$. This technique gives the anisotropy vectors with respect to direction of travel and with respect to the maximum reflection strength in a given survey.

Results

In the Prudhoe Bay data, the radar antenna pair polarized perpendicular to the survey direction clearly profiles the ice/water interface located at about 1.5 m, but the ice/water interface is almost completely absent from data collected with polarization in-line with direction of travel. We interpret this directionally-dependent attentuation as a

result of preferential alignment with the anisotropic ice structure. However, using our system, the vector sum provides the most complete profile of the bottom of the ice (Figure 5.4).

The data collected at CRREL in 2012 also demonstrate differences in reflection strength between the two orthogonal antenna polarizations (Figure 5.5). In this case, both data sets profile the reflection associated with the ice bottom at approximately 0.40 m, including topographic highs at 4 and 10 m. However, the in-line polarization reflection strength is weaker at almost all locations. The most likely cause is preferential attenuation due to anisotropy. In these data, the effects of the preferential attenuation on the ice bottom reflection event are evident both in the clean and oil-contaminated areas.

Finally, we plot an example showing relative direction and strength of the anisotropy for the Prudhoe Bay data (Figure 5.4d). Since previous work correlates the direction of dominant crystal alignment with current, knowing the direction of anisotropy has important implications for application such as oil spill response in Arctic conditions. For example, the dominant current direction can indicate in which direction spilled oil is likely to migrate underneath an ice sheet. In a spill response effort, this additional knowledge can aid spill responders in efforts to track and monitor the spilled oil.

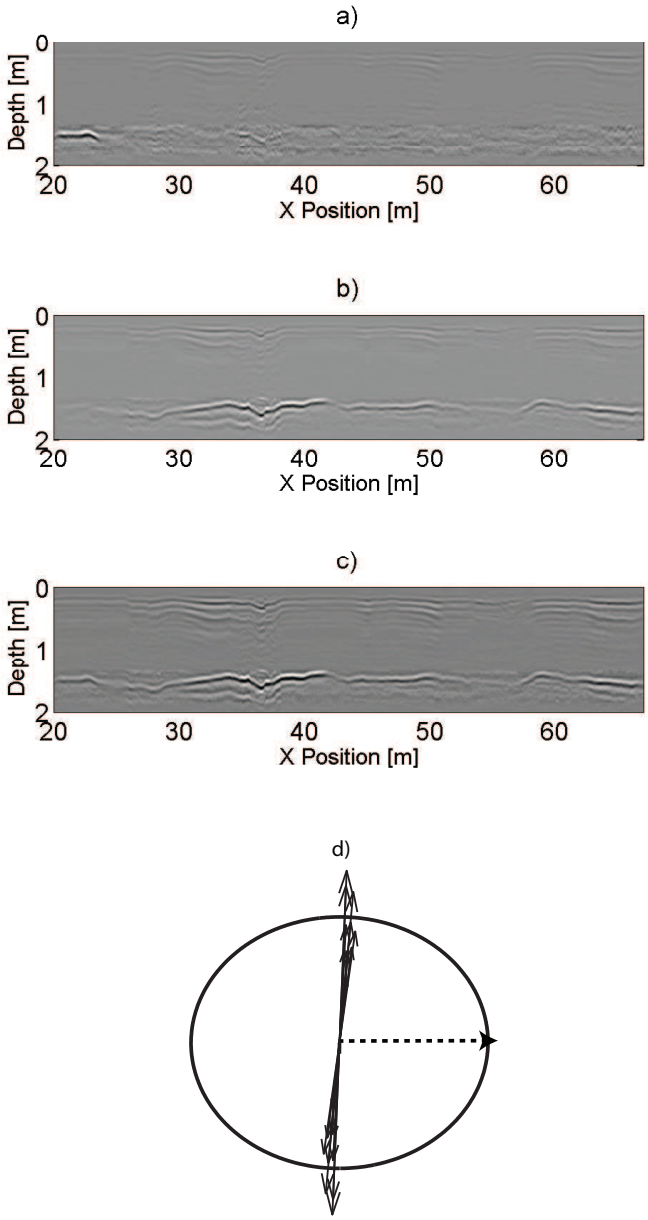

Figure 5.4: Data collected over sea ice at Prudhoe Bay, Alaska using the dual-polarization system: a) in line with survey direction, b) perpendicular to survey direction, and c) vector sum of a) and b). The combined information from both polarizations provides the most complete image of the sea ice/ water interface. d) Solid arrows denote relative direction and relative strength of anisotropy with respect to the survey direction (dashed arrow) and relative to the unit circle. Two equally valid solutions exist (±180°).

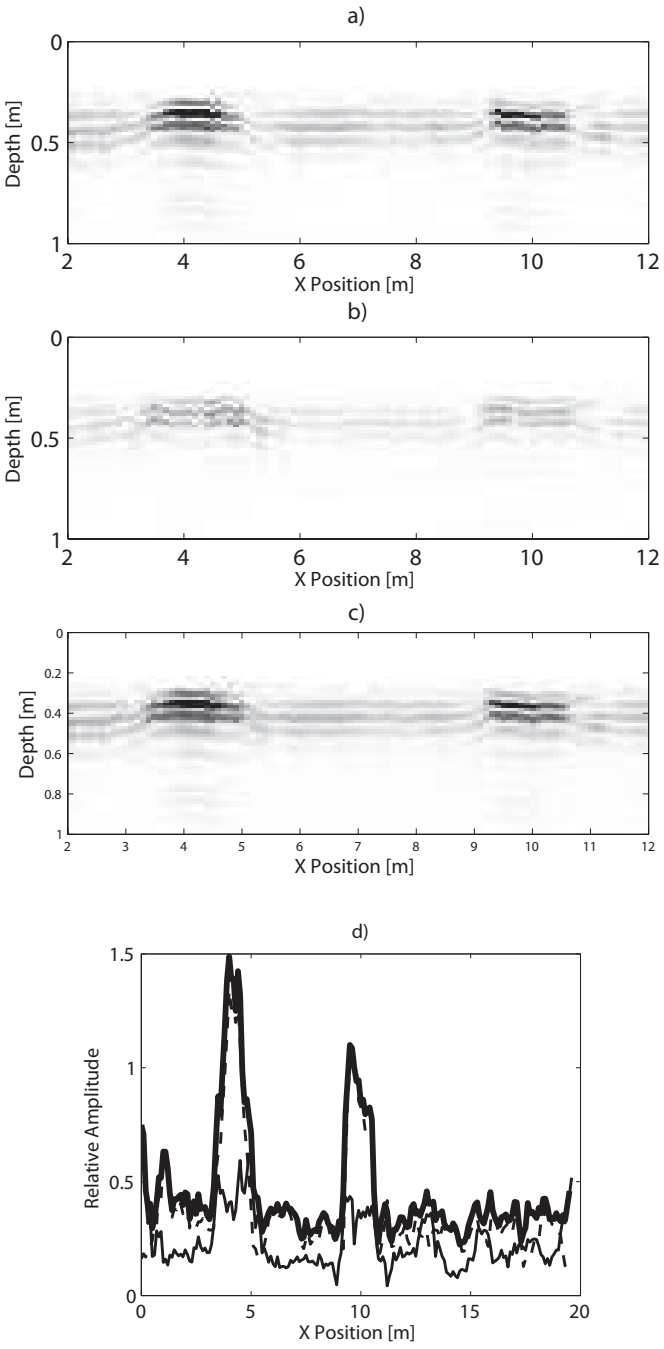

Figure 5.5: Radar data collect over a saline ice sheet at CRREL at 0.1 m increments a) in line with survey direction, b) perpendicular to survey direction, and c) vector sum of a) and b); d) shows relative reflection strength across corresponding to a (dashed line), b (solid line), and c (bold line) with very high amplitudes corresponding to oil locations under the ice at about 4-5 m (traces 40-50) and 9-11 m (trace 90-110).

Conclusions

Preferential alignment of the sea ice physical structure during ice growth results in anisotropy in the physical and electrical properties of sea ice. We decompose EM wave propagation in sea ice into two cases: 1) the EM wave polarized parallel to the conductivity structure of the ice ($\mathbf{E}_{\parallel}$), and 2) the EM wave polarized perpendicular to the conductivity structure ($\mathbf{E}_{\perp}$). Higher σ_{ef} in the parallel direction can attenuate the radar wave travel to the extent that the ice bottom reflection is completely extinguished. A data example demonstrates the need for a GPR system capable of robustly imaging the ice/water interface regardless of anisotropy direction.

We configured a commercial radar system to provide simultaneous acquisition with antenna pairs polarized in line with and perpendicular to survey direction. Our approach allows for proper treatment of conductivity anisotropy and minimizes problems with interpretation of the sea ice/water interface. Data processing and interpretation show that this system is effective for imaging the ice/water interface regardless of dominant crystal alignment. Our system has applications for monitoring sea ice thickness; detecting contaminants such as oil in and under sea ice; and monitoring the movement of contaminants under an ice sheet. Collecting data using the dual-polarization system has proven rapid and reliable at two field sites, and interpretations of ice depth have corresponded well with field data where available. With minimal training, personnel could use the system to monitor ice thickness under Arctic conditions, and thereby reduce hazard exposure to personnel as compared to traditional methods of ice monitoring such as core drilling.

CONCLUSIONS

The targeted full-waveform inversion algorithm was able to recover layer properties to within 10% for both the seismic and radar reflection models with the exception of conductivity for the radar case and seismic quality factor in the seismic case. In the radar laboratory and field examples, inverted thin-layer properties were within 15% of measured or estimated values. In addition, for two of the radar examples the inversion algorithm performed robustly even when solving for properties of two separate layers. In the seismic case, it is impossible to quantitatively assess the accuracy of the inversion results using the field data since seismic properties for the basal ice layer underneath Bench Glacier are unknown. Furthermore, seismic properties of frozen earth materials have a broad range in values depending on porosity, water saturation, sorting, overburden, and other factors (see Chapter 4 for examples). Nevertheless, I demonstrated that the inversion results are within reported literature ranges for basal ice layers.

It is interesting to note that in both the seismic and radar cases, the inversion algorithm does not appear to be particularly sensitive to thin-layer attenuation parameters. For example, in Chapter 3, I showed that inversion solutions for σ deviated up to 5 orders of magnitude from the true model values. In Chapter 5, testing revealed that the inversion solution for modeled thin-layer Q was up to 200% greater than the input model value. For the radar case, if the low-loss criteria holds, changes in permittivity dominate

reflectivity responses. For seismic data, if *Q* is large the second term in equation 4.3 goes towards zero and the effect of *Q* on the reflection coefficient is small. For example, if Q is greater than 100, the resulting contribution to the reflection coefficient may be less than 1% depending of course on frequency. Then, the primary contribution of *Q* or σ is to attenuate the traveling wave by $e^{-\alpha x}$ where *x* is the distance traveled in the layer. For radar-wave travel $\alpha = \alpha_t$ (equation 1.43), and $\alpha = \frac{\omega}{2vQ}$ in the seismic case (equation 4.6). Obviously, as the layer thickness decreases, the attenuation also decreases, in this case exponentially. Then in the thin- and ultra-thin layer cases I tested, the inversion may not be sensitive to layer σ or *Q* since it contributes little either to the attenuation or to the reflectivity response. An exception would be in the case either of high σ or low *Q*: if the low-loss criteria is invalid or the layer thickness approaches the skin depth, then attenuation due to *Q* or σ may become significant even in the thin-layer case. Then the inversion algorithm may provide more reliable estimations for the two parameters if layer thickness were increased or at higher values of σ and *Q*. Future testing of the inversion algorithm should include model testing to retrieve layer σ and *Q* at higher, rather than lower, layer thicknesses, and subsequent testing on field data.

Finally, the user must recognize that the inversion algorithm depends on many assumptions and simplifications and any of these can easily be violated with subsequent detrimental consequences on inversion performance. For example, one assumption inherent within the 1D reflectivity model is that the subsurface can be represented by a stack of homogeneous, isotropic, layered materials. The subsurface is neither homogeneous nor isotropic. Violations of these assumptions lead to problems and inaccuracies not just within the inversion algorithm accuracy but even within the data

itself. For example, in Chapter 5, I demonstrated that in the face of strong anisotropy within the conductivity structure of a subsurface material, standard radar reflection methods may fail to provide reliable subsurface imaging. Thus, the presence of anisotropy not only violates the assumptions of the reflectivity model but also can invalidate data collection methods. In either of those cases, it is obvious that the inversion will fail to generate reliable results. Thus, I demonstrated the efficacy of a dual-polarization radar system for robust collection of radar data even in the case of pronounced subsurface anisotropy. By using this system to collect data over sea ice in the event of a contamination event such as an oil spill, subsequent use of those data within the inversion algorithm would be much more likely to succeed at retrieving oil locations and thicknesses reliably.

This targeted full-waveform inversion and the dual-polarization radar system have potential widespread use for environmental monitoring and environmental remediation. The dual-polarization system provides a reliable method to image the water-ice interface rapidly and over long distances. Potential applications include sea-ice surveys to provide ground-truth data for satellite sea ice measurements. With the increase of remote sensing and modeling based on remote measurements, researchers and practitioners alike sorely need such reliable ground verification of satellite data. In addition, personnel who monitor sea ice depth for hazard mitigation assessment in remote operating areas could use this system to do it more quickly, safely, and reliably than current borehole methods. In the event of a spill, as mentioned previously, remediation workers could use the dual-polarization system in conjunction with the inversion algorithm to best delineate priority response areas.

As I demonstrated, practitioners can also implement my inversion algorithm on glacier seismic data in order to define basal conditions. Such applications will enhance environmental monitoring and modeling efforts. Specifically, glacier dynamics are tied to glacier movement and even to global climate change, and glacier dynamics depend in part on basal conditions (Chapter 4). Thus using the inversion algorithm to quantitatively define basal conditions is another innovative application of my research. However, as demonstrated in Chapters 2 and 3, I feel the real strength of the inversion algorithm lies in retrieving thin-layer properties where those layers are the result of environmental contamination. The inversion has demonstrated remarkable reliability (< 15% error) in retrieving contaminant permittivity and thickness using both model and field data for two different types of contaminants: LNAPLs and DNAPLs.

Additional model testing in Chapter 2 indicated that the inversion may perform well even at layer thicknesses as low as 0.4%λ, although in the presence of noise this limit is likely to be higher. Thus, future work should include application of this inversion algorithm on additional field data sets. Careful choice of data sets should allow for inversion testing on both thicker and thinner contaminant layers as well as additional types of contaminant. Testing the algorithm on a contaminant with relatively high conductivity (> 0.05 S m^{-1}, see Figure 2.3) would be particularly beneficial in the ongoing effort to carefully and quantitatively define the inversion strength and weaknesses.

Furthermore, additional work on the algorithm itself should attempt to automate the windowing of the reflection event. Currently, this process involves manually picking the target window trace by trace. The need for manual picking limits the number of traces

the inversion can process in any given time. Automating the event windowing would allow more rapid processing of large data sets at contaminated sites. One such large data set is the Wurtsmith AFB contaminated site, which I discussed in Chapter 3. Future work should include testing an automated version of my algorithm on those data or another similar data set with lower levels of noise.

In conclusion, this body of work provides a new targeted full-waveform inversion for quantifying thin-layer parameters as well as a new method of collecting reliable radar data where the subsurface may be highly anisotropic. Here I demonstrated the inversion robustness on both radar and seismic data. Eventual field implementation could provide rapid and robust subsurface characterization of thin-layers over larger areas than point source measurements. Thus it may be particularly beneficial to environmental monitoring and remediation efforts.

REFERENCES

Alley, R.B., D.D. Blankenship, C.R. Bentley, and S.T. Rooney, 1987, Till beneath ice stream 3. Till deformation: Evidence and implications: *Journal of Geophysical Research*, **92**, 8921- 8929.

Aki, K., and P.G. Richards, 2002, Quantitative seismology: Theory and Methods: W.H. Freeman and Co.

Anandakrishnan S., 2003, Dilatant till layer near the onset of streaming flow of Ice Stream C, West Antarctica, determined by AVO (amplitude vs offset) analysis: *Annals of Glaciology*, **36**, 283-286.

Anderson, R.S., S.P. Anderson, K.R. MacGregor, E.D. Waddington, S. O'Neel, C.A. Riihimaki, and M.G. Loso, 2004, Strong feedbacks between hydrology and sliding of a small alpine Glacier: *Journal of Geophysical Research*, **109**, F03005.

Annan, A.P., 2005, Ground-penetrating radar, *in* D.K. Butler, ed., Near-surface geophysics: Society of Exploration Geophysicists, 357-438.

Archie, G. E., 1942, The electrical resistivity log as an aid in determining some reservoir characteristics: *Transactions of the American Institute of Mining and Metallurgical Engineers*, **146**, 54-61.

Aster, R.C., B. Borchers, and C.H. Thurber, 2005, Parameter Estimation and Inverse Problems: Elsevier Academic Press.

Babcock, E.L. and J.H. Bradford, 2014a, Targeted full-waveform inversion of ground-penetrating radar reflection data for thin and ultra-thin layers of non-aqueous phase liquid contaminants Part I: Algorithm and synthetic testing: *Geophysics, submitted*.

Babcock, E.L. and J.H. Bradford, 2014b, Targeted full-waveform inversion of ground-penetrating radar reflection data for thin and ultra-thin layers of non-aqueous phase liquid contaminants Part 2: Data testing: *Geophysics*, submitted.

Babcock, E.L. and J.H. Bradford, 2014c, Electrical anisotropy in sea ice and a dual-polarization radar system to mitigate the effects of preferential attenuation in imaging sea ice: *Cold Regions Research and Engineering*, submitted.

Babcock, E.L. and J. H. Bradford, 2013, Detecting subsurface contamination using ground penetrating radar and amplitude variation with offset analysis: *IEEE*

*Proceedings: 7th International Workshop on Advanced Ground Penetrating Radar***,** doi:10.1109/IWAGPR.2013.6601546.

Baker, G. S., 1998, Applying AVO analysis to GPR data: *Geophysical Research Letters*, **25**, 397-400.

Baker, G.S., J.C. Strasser, E.B. Evenson, D.E. Lawson, K. Pyke, and R.A. Bigl, 2003, Near-surface seismic reflection profiling of the Matanuska Glacier: Alaska: *Geophys*ics, **68**, 147–156.

Bermejo, J.L., W.A. Sauck, and E.A. Atekwana, 1997, Geophysical discovery of a new LNAPL plume at the former Wurtsmith AFB, Oscoda, Michigan: *Groundwater Monitoring and Remediation*, **17**, 131-137.

Blankenship, D.D., C.R. Bentley, S.T. Rooney, and R.B. Alley, 1986, Seismic measurements reveal a saturated porous layer beneath an active Antarctic ice stream: *Nature*, **322**, 54-57.

Booth, A.D., R.A. Clark, B. Kulessa, T. Murray, J. Carter, S. Doyle, and A. Hubbard, 2013, Thin-layer effects in glaciological seismic amplitude-versus-angle (AVA) analysis: implications for characterizing a subglacial till unit, Russell Glacier, West Greenland: *The Cryosphere*, **6**, 909-922.

Bradford, J.H., 2002, Depth characterization of shallow aquifers with seismic reflections, Part I – The failure of NMO velocity analysis and quantitative error prediction: *Geophysics*, **67**, 89 – 97.

Bradford, J.H., 2006, Applying reflection tomography in the postmigration domain to multifold ground-penetrating radar data: *Geophysics*, **71**, K1-K8.

Bradford, J.H., 2007, Frequency-dependent attenuation analysis of ground-penetrating radar data: *Geophysics*, **72**, J7-J16.

Bradford, J.H., and E.B. Babcock, 2013, The need to adapt the exploration model from the oil patch to contaminated-site characterization: A case study from Hill AFB, Utah, USA: The Leading Edge, **32**, 750 – 756.

Bradford, J.H., and J.C. Deeds, 2006, Ground-penetrating radar theory and application of thin-bed offset-dependent reflectivity: *Geophysics*, **71**, K47-K57.

Bradford, J.H., and Y. Wu, 2007, Instantaneous spectral analysis: Time-frequency mapping via wavelet matching with application to contaminated site characterization by 3D GPR: *The Leading Edge*, **12**, 1018-1023.

Bradford, J.H., D.F. Dickins, and P.J. Brandvik, 2010, Assessing the potential to detect oil spills in and under snow using airborne ground-penetrating radar: *Geophysics* **75**, G1-G12.

Bradford, J.H., J. Nichols, J.T. Harper, and T. Meierbachtol, 2013, Compressional and EM wave velocity anisotropy in a temperate glacier due to basal crevasses and implications for water content estimation: *Annals of Glaciol*ogy, **54**, doi:10.3189/2013AoG64A206.

Bradford, J.H., J. Nichols, T.D. Mikesell, and J.T. Harper, 2009, Continuous profiles of electromagnetic wave velocity and water content in glaciers: an example from Bench Glacier, Alaska, USA: *Annals of Glaciol*ogy, **50**, 1-9.

Bradford, J.H., W.P. Clement, and W. Barrash, 2009, Estimating porosity with ground-penetrating radar reflection tomography: A controlled 3-D experiment at the Boise Hydrogeophysical Research Site: *Water Resources Research*, **45**, W00D26.

Brewster, M.L., and A.P. Annan, 1994, Ground-penetrating radar monitoring of a controlled DNAPL release: 200 MHz radar: *Geophysics*, **59**, 1211–1221.

Brown, J., J. Harper, and J. Bradford, 2009, A radar transparent layer in a temperate valley glacier: Bench Glacier, Alaska: *Earth Surface Processes and Landforms*, **34**: 1497-1506.

Brusseau, M.L., K.C. Carroll, T. Allen, J. Baker, W. DiGuiseppi, J. Hatton, C. Morrison, A. Russo, and J. Berkompas, 2011, Impact of in situ chemical oxidation on contaminant mass discharge: linking source-zone and plume-scale characterizations of remediation performance: *Environmental Science and Technology*, **45**, 5352-5358.

Brusseau, M.L., N.T. Nelson, Z. Zhang, J.E. Blue, J. Rohrer, and T. Allen, 2007, Source-zone characterization of a chlorinated-solvent contaminated Superfund site in Tucson, AZ: *Journal of Contaminant Hydrology*, **90**, 21-40.

Buchanan, S., M. Ingham, and G. Gouws, 2011, The low frequency electrical properties of sea ice: *Journal of Applied Physics*, **110**, 074908.

Burger, R.H., A.F. Sheehan, and C.H. Jones, 2006, Introduction to Applied Geophysics: Exploring the Shallow Subsurface: W.W. Norton and Company.

Burns, L.E., G.H. Pessel, T.A. Little, T.L. Pavlis, R.J. Newberry, G.R. Winkler, and J. Decker, 1991, Geology of the Northern Chugach Mountains, South Central Alaska: Alaska Department of Natural Resources Report 94.

Busch, S., J. van der Kruk, J. Bikowski, and H. Vereecken, 2012, Quantitative conductivity and permittivity estimation using full-waveform inversion of on-ground GPR data: *Geophysics*, **77**, H79-H91.

Campbell, K.J. and A.S. Orange, 1974, The electrical anisotropy of sea ice in the horizontal plane: *Journal of Geophysical Research*, **79**, 5059-5063.

Carcione, J.M., G. Seriani, and D. Gei, 2003, Acoustic and electromagnetic properties of soil saturated with salt water and NAPL: *Journal of Applied Geophysics*, **52**, 177-191.

Castagna, J.P., 1993, AVO Analysis – Tutorial and Review, *in* J.P. Castagna and M.M. Backus, eds., Offset Dependent Reflectivity –Theory and Practice of AVO Analysis, Society of Exploration Geophysicists, 3-36.

Chandler, D.M., R.I. Waller , and W.G. Adam, 2005, Basal ice motion and deformation at the ice-sheet margin, West Greenland: *Annals of Glacio*logy, **42**. 67 – 70.

Chapman, P.M., and M.J. Riddle, 2005, Toxic effects of contaminants in polar marine environments: *Environmental Science and Technology*, **39**, 200A-207A.

Clarke, G.K.C., 2005, Subglacial Processes: *Annual Review of Planetary Science*, **33**, 247-276.

Cohen, D., N.R. Iverson, T.S. Hooyer, U.H. Fischer, M. Jackson, and P.L. Moore, 2005, Debris-bed friction of hard-bedded glaciers: *Journal of Geophysical Research,* **110**, F02007.

Cole, K.S., and R.H. Cole, 1941, Dispersion and absorption in dieletrics I. Alternating current characteristics: *The Journal of Chemical Physics*, **9**, 341-351.

Debye, P.J.W., 1929, Polar molecules: Dover Press.

Deparis, J., and S. Garambois, 2009, On the use of dispersive APVO GPR curves for thin-bed properties estimation: Theory and application to fracture characterization: *Geophysics* **74**, J1-J12.

Dow, C.F., A. Hubbard, A.D. Booth, S.H. Doyle, A. Gusmeroli, and B. Kulessa, 2013, Seismic evidence of mechanically weak sediments underlying Russell Glacier, West Greenland: *Annals of Glaciology*, **54**, 135 – 141.

Evans, D.J.A., E.R. Phillips, J.F. Hiemstra, and C.A. Auton, 2006, Subglacial till: Formation, sedimentary characteristics and classification: *Earth Science* Reviews, **78**: 115 -176.

Fleisch, D., 2008, A Student's Guide to Maxwell's Equations: Cambridge University Press.

Fowler, C.M.R., 1990, The Solid Earth: An Introduction to Global Geophysics: Cambridge University Press.

Frankenstein, G. and R. Garner, 1967, Short note: Equations for determining the brine volume of sea ice: *Journal of Glaciology*, **6**, 943-944.

Fudge, T.J., N.F. Humphrey, J.T. Harper, and W.T. Pfeffer, 2008, Diurnal fluctuations in borehole water levels: configuration of the drainage system beneath Bench Glacier, Alaska, USA: *Journal of Glaciology*, **54**, 297 – 306.

Fudge, T.J., J.T. Harper, N.F. Humphrey, and W.T. Pfeffer, 2009, Rapid glacier sliding, reverse ice motion and subglacial water pressure during an autumn rainstorm: *Annals of Glaciology*, **50**, 101 – 108.

Gazdag, J. and P. Sguazzero, 1964, Migration of seismic data: *Proceedings of the IEEE*, **72**, 1302-1315.

Golden, K., 1995, Bounds on the complex permittivity of sea ice: *Journal of Geophysical Research*, **100**, 13699-13711.

Golden, K.M. and S.F. Ackley, 1981, Modeling of anisotropic electromagnetic reflection from sea ice: *Journal of Geophysical Research*, **86**, 8107-8116.

Goldman, M., 1983, The Demon in the Ether: The Story of James Clerk Maxwell, Edinburgh: Harris Press.

Griffiths, D.J., 1999, Introduction to Electrodynamics: Prentice Hall.

Guha, S., S.E. Kruse, E.E. Wright, and U.E. Kruse, 2005, Spectral analysis of ground penetrating radar response to thin sedimentary layers: *Geophysical Research Letters*, **32**, L23304.

Gusmeroli, A., R.A. Clark, T. Murray, A.D. Booth, B. Kulessa, and B.E. Barrett, 2010, Seismic wave attenuation in the uppermost glacier ice of Storglaciaren, Sweden: *Journal of Glaciology*, **56**, 249 – 256.

Harper, J.T., J.H. Bradford, N.F. Humphrey, and T.W. Meierbachtol, 2010, Vertical extension of the subglacial drainage system into basal crevasses: *Nature*, **567**, 579-582.

Hart, J.K., 1995, An investigation of the deforming layer/debris-rich basal-ice continuum, illustrated from three Alaskan glaciers: *Journal of Glacio*logy, **41**: 619 – 634.

Hart, J.K., and R.I. Waller, 1999, An investigation of the debris-rich basal ice from Worthington Glacier, Alaska, U.S.A: *Journal of Glacio*logy, **45**: 54 – 62.

Hart, J.K., K.C. Rose, and K. Martinez, 2011, Subglacial till behavior derived from in situ wireless multi-sensor subglacial probes: Rheology, hydro-mechanical interactions and till formation: *Quaternary Science Reviews*, **30**, 234-247.

Hauck, C., M. Bootcher, and H. Maurer, 2011, A new model for estimating subsurface ice content based on combined electrical and seismic data sets: *Cryosphere*, **5**: 453 – 468.

Hinz, E.A., 2012, Utilizing electrical conductivity for characterizing hydrogeological properties: Ph.D. dissertation, Boise State University.

Hohmann, G.W., 1988, Numerical Modeling for Electromagnetic Methods of Geophysics, volume 1, Society of Exploratory Geophysicists, 313 – 364.

Howat, I.M., S. Tulaczyk, E. Waddington, and H. Bjornsson, 2008, Dynamic controls on glacier basal motion inferred from surface ice motion: *Journal of Geophysical Research*, **113**, F03015.

Hwang, Y.K., A.L. Endres, S.D. Piggott, and B.L. Parker, 2008, Long-term ground penetrating radar monitoring of a small volume DNAPL release in a natural groundwater flow field: *Journal of Contaminant Hydrology*, **97**, 1-12.

Illangasekare, T.H., J.L. Ramsey, K.H. Jensen, and M.B. Butts, 1995, Experimental study of movement and distribution of dense organic contaminants in heterogeneous aquifers: *Journal of Contaminant Hydrology*, **20**, 1-25.

Irving, J,. and R. Knight, 2006, Numerical modeling of ground-penetrating radar in 2-D using Matlab: *Computers and Geosciences*, 32, 1247 - 158.

Johansen, T.A., P. Digranes , M. van Schaak, and E. Lonne, 2003, Seismic mapping and modeling of near-surface sediments in polar areas: *Geophysics*, **68**(2): 566 -573.

Jones, K.A., M. Ingham, D.J. Pringle, and H. Eicken, 2010, Temporal variations in sea ice resistivity: Resolving anisotropic microstructure through cross-borehole DC resistivity tomography: *Journal of Geophysical Research*, **115**, C11023.

Kalogeropoulos, A., J. van der Kruk, J. Hugenschmidt, J. Bikowski, and E. Bruhwiler, 2013, Full-waveform GPR inversion to assess chloride gradients in concrete: *NDT&E International*, **57**, 74-84.

Klotzsche, A., J. van der Kruk, G.A. Meles, J. Doetsch, H. Maurer, and N. Linde, 2010, Full-waveform inversion of cross-hole ground-penetrating radar data to characterize a gravel aquifer close to the Thur River, Switzerland: *Near Surface Geophysics*, **8**, 635-649.

Kim, K.Y., J. Lee, M.H. Hong, J.K. Hong, Y.K. Jin, and H. Shon, 2010, Seismic and radar investigations of Fourcade Glacier on King George Island, Antarctica. *Polar Research*, **29**, 298-310.

King, E.C., J. Woodward, and A.M. Smith, 2004 Seismic evidence for a water-filled canal in deforming till beneath Rutford Ice Stream, West Antarctica: *Geophysical Research Letters*, **31**, L20401.

Knight, P.G., 1997, The basal ice layer of glaciers and ice sheets: *Quaternary Science Reviews*, **16**: 975 – 993.

Knight, R.J., and A.L. Endres, 2005, An introduction to rock physics principles for near-surface geophysics, *in* D.K. Butler, ed., Near-surface geophysics: Society of Exploration Geophysicists, 31-70.

Kovacs, A., and R.M. Morey, 1978, Radar anisotropy of sea ice due to preferred azimuthal orientation of the horizontal c axes of ice crystals: *Journal of Geophysical Research***, 83**, 6037–6046.

Kovacs, A., and R. M. Morey, 1979, Anisotropic Properties of Sea Ice in the 50- to 150-MHz Range: *Journal of Geophysical Research***, 84**, 5749–5759.

Kovacs, A., and R.M. Morey, 1986, Electromagnetic measurements of multi-year sea ice using impulse radar: *Cold Regions Science and Technology*, **12**, 67-93.

Kovacs, A., R.M. Morey, and G.F.N. Cox, 1987, Modeling the electromagnetic property trends in sea ice, Part 1: *Cold Regions Science and Technology*, **14**, 207-235.

Lagarias, J.C., J.A. Reeds, M.H. Wright, and P.E. Wright, 1998, Convergence properties of the Nelder-Mead simplex method in low dimensions: *SIAM Journal of Optimization*, **9**, 112-147.

Lambot, S., M. Antoine, I. van den Bosch, E.C. Slob, and M. Vanclooster, 2004, Electromagnetic inversion of GPR signals and subsequent hydrodynamic inversion to estimate effective vadose zone hydraulic properties: *Vadose Zone Journal*, **3**, 1072-1081.

Luciano, A., P. Viotti, and M.P. Papini, 2010, Laboratory investigation of DNAPL migration in porous media: *Journal of Hazardous Materials*, **176**, 1006-1017.

MacGregor, K.R., C.A. Riihimaki, and R.S. Anderson, 2005, Spatial and temporal evolution of rapid basal sliding on Bench Glacier, Alaska, USA: *Journal of Glaciol*ogy, **51**, 49-63.

Magnusson, E., H. Bjornsson, H. Rott, and F. Palsson, 2010, Reduced glacier sliding caused by persistent drainage from a subglacial lake: *The Cryosphere*, **4**, 13-20.

McGinnis, L.D., K. Nakao, and C.C. Clark, 1973, Geophysical Identification of Frozen and Unfrozen Ground, Antarctica *in* Permafrost: North American Contribution to the Second International Conference, 136 – 146.

Meier, M.F., 2007, Glaciers Dominate Eustatic Sea-Level Rise in the 21st Century: *Science*, **317**, 1064-1067.

Menke, W., 1984, Geophysical Data Analysis: Discrete Inverse Theory: Academic Press, Inc.

Mikesell, T.D., K. van Wijk, M.M. Haney, J.H. Bradford, H.P. Marshall, and J.T. Harper, 2013, Monitoring glacier surface seismicity in time and space using Rayleigh waves: *Journal of Geophysical Research*, **117**, F02020.

Morey, R.M., A. Kovacs, and G.F.N. Cox, 1984, Electromagnetic properties of sea ice: *Cold Regions Science and Technology*, **9**, 53-75.

Morlet, J., G. Arens, E. Fourgeau, and D. Giard, 1982, Wave-propagation and sampling theory 1. Complex signal and scattering in multilayered media: *Geophysics*, **47**, 203-221.

Muller, G., 1985, The reflectivity method: a tutorial: *Journal of Geophysics*, **58**, 153-174.

Nakawo, M., 1981, Growth-rate and salinity profile of 1st year sea ice in the high Arctic: *Journal of Glaciology*, **96**, 315-330.

Nellis, S.R., H. Yoon, C.J. Werth, M. Oostrom, and A.J. Valocchi, 2009, Surface and interfacial properties of nonaqueous-phase liquid mixtures released to the subsurface at the Hanford site: *Vadose Zone Journal*, **8**, 343-351.

Nyland, D., 2004, Profiles of floating ice in Arctic regions using GPR, *The Leading Edge*, **23**, 6665-668.

Nolan, M. and K. Echelmeyer, 1999, Seismic detection of transient changes beneath Black Rapids Glacier, Alaska, U.S.A: II. Basal morphology and processes: *Journal of Glaciology*, **45**, 132-146.

Operto, S., Y. Gholan, V. Prieux, and A. Ribodetti, 2012, A guided tour of multiparameter full-waveform inversion with mulitcomponnent data: From theory to practice: *The Leading Edge*, **32**, 1040-1054.

Orlando, L., 2002, Detection and analysis of LNAPL using the instantaneous amplitude and frequency of ground-penetrating radar data: *Geophysical Prospecting*, **50**, 27-41.

Pankow, J.F., and J.A. Cherry, 1996, Dense chlorinated solvents and other DNAPLs in groundwater: Waterloo Press.

Pelton, J.R., 2005, Near-Surface Seismology: Wave Propagation, *in* D.K. Butler, ed., Near-surface geophysics: Society of Exploration Geophysicists, 177- 217.

Pentrenko, V.F. and R.W. Whitworth, 1999, Physics of Ice: Oxford University Press, Oxford.

Plessix, R.E., G. Baeten, J.W. de Maag, F. ten Kroode, and R.J. Zhang, 2012, Full waveform inversion and distance separated simultaneous sweeping: a study with a land seismic data set: *Geophysical Prospecting*, **60**, 733-747.

Porter, P.R., and T. Murray, 2001, Mechanical and hydraulic properties of till beneath Bakaninbreen, Svalbard: *Journal of Glaciology*, **47**, 167 -175.

Press, F., 1966 Seismic velocities, *in* S.P.Clark Jr., ed., Handbook of Physical Constants, The Geological Society of America Memoir, New York.

Riihimaki, C.A., K.R. MacGregor, R.S. Anderson, S.P. Anderson, and M.G. Loso, 2005, Sediment evacuation and glacial erosion rates at a small alpine glacier: *Journal of Geophysical Research*, **110**, F03003.

Sauck, W.A., E.A. Estella, and M.S. Nash, 1998, High conductivities associated with an LNAPL plume imaged by integrated geophysical techniques: *Journal of Environmental and Engineering Geophysics*, **2**, 203-212.

Smith, A.M., 2007, Subglacial Bed Properties from Normal-Incidence Seismic Reflection Data: *JEEG*, **12**, 3-13.

Smith, A.M., T.A. Jordan, F. Ferraccioli, and R.G. Bingham, 2013, Influence of subglacial conditions on ice stream dynamics: Seismic and potential field data from Pine Island Glacier, West Antarctica: *Journal of Geophysical Research*, **118**, 1471 – 1482.

Stanovoy, V.W., T.R. Eremina, A.V. Isaev, I.A. Neelow, R.E. Vankevich, and V.A. Ryabchenko, 2012, Modeling of oil spills in ice conditions in the Gulf of Finland on the basis of an operative forecasting system: *Marine Physics*, **52**, 754-759.

Stogryn, A., 1971, Equations for calculating the dielectric constant of saline water: *IEEE Transactions on Microwave Theory and Techniques*, **MT19**, 633-736.

Sydnes, L.K., T.H. Hemmingsen, S. Skare, S.H. Hansen, I.B. Falkpetersen, S. Lonning, and K. Ostgaard, 1985, Seasonal variations in weathering and toxicity of crude oil on seawater under Arctic conditions: *Environmental Science and Technology*, **19**, 1076-1081.

Taner, M.T., F. Koehler, and R.E. Sheriff, 1979, Complex seismic trace analysis: *Geophysics*, **44**, 1041-1063.

Taylor, L.S., 1965, Dielectric properties of mixtures: *IEEE Transactions on Antennae and Propagation*, **13**, 943-947.

Timco, G.W. and W.F. Weeks, 2010, A review of the engineering properties of sea ice: *Cold Regions Science and Technology*, **60**, 107-129.

Tran, A.P., M.R. M. Ardekani, and S. Lambot, 2012, Coupling of dielectric mixing models with full-wave ground-penetrating radar signal inversion for sandy-soil-moisture estimation: *Geophysics*, **77**, H33-H44.

Tsoflias, G.P. and M.W. Becker, 2008, Ground-penetrating radar response to fracture-fluid salinity: Why lower frequencies are favorable for resolving salinity changes: *Geophysics*, **73**, J25-J30.

Tucker, W.B., 1984, On small-scale horizontal variations of salinity in first-year sea ice: *Journal of Geophysical Research*, **89**, 6505-6514.

United States Environmental Protection Agency (USEPA), 2007, Field Analytical and Site Characterization Technologies: Summary of Applications: Washington, DC: EPA-542-R-97-011.

Waller, R.I., J.K. Hart, and P.G. Knight, 2000, The influence of tectonic deformation on facies variability in stratified debris-rich basal ice: *Quaternary Science Reviews*, **19**, 775 – 786.

Widess, M.B, 1973, How thin is a thin bed?: *Geophysics*, **38**, 1176-1180.

Winkler, G.R., M.L. Silberman, A. Grantz, R.J. Miller, and M.M. MacKevett, Jr., 1980, Geologic map and summary geochronology of the Valdez Quadrangle, southern Alaska: U.S. Geological Survey Open-File Report 80-892-A.

Yapa, P.D. and S.A. Weerasuriya, 1997, Spreading of oil spilled under floating broken ice: *Journal of Hydraulic Engineering*, **25**, 676-683.

Yee, K.S., 1966, Numerical Solution of Initial Boundary Value Problems Involving Maxwell's Equations in Isotropic Media: *IEEE Transactions of Antennas and Propagation*, **14**, 802-807.

Yilmaz, O., 2002, Seismic Data Analysis: Society of Exploration Geophysicists.

Zeng, X.X., G.A. McMechan, and T. Xu, 2000, Synthesis of amplitude-versus-offset variations in ground-penetrating radar data: *Geophysics*, **65**, 113-125.

APPENDIX A

Linking Science to Public Policy for Land and Resource Management:

A University Case Study

Abstract

Scientific information offers unique contributions to public policy decisions for land management and resource use. Unfortunately, various barriers hinder transfer of science to decision makers. Boundary organizations play a prominent role among constructs designed to bridge these gaps between science and policy. Here we examine the role of boundary organizations and segregate boundary organization theory into boundary organizations, boundary objects, and boundary-spanning individuals. A case study conducted within a university setting provides additional information about these constructs and the processes and barriers operating between scientists and decision makers. We conclude that the classification of "boundary objects" may include non-traditional boundary objects such as buildings.

Problem Statement

Science strives to produce unique, verifiable, accurate information about the natural world and its systems. Thus science can be a vital component of the decision making process for most public policymaking relevant to public lands use and sustainable management of natural resources. However, what or who defines "science" is itself a contentious issue. Decision makers must address this definition in an effort to promote stakeholder confidence and to promote minimally-biased and repeatable scientific conclusions.

Properly understood, science is often able to provide unique information about current resource status and expected future outcomes (Lackey, 2007). For example, scientists can use various methodologies to test a hypothesis and make conclusions about

reactive changes in populations within a forest ecosystem due to mining activities. Decision makers could consider such information within the context of a public policy decision concerning mining permits. Similar examples abound within almost all decisions that impact natural resources, the foundation for sustaining human life on this planet.

Admittedly, there exist a plethora of factors besides science that decision makers weigh when determining public policy. Decision making for resource management involves balancing competing interests and stakeholder demands. Economics, social norms, public values, ecological repercussions, and related externalities are but a few examples. These systems are legally and morally imperative in the decision making process. These non-scientific factors often drive national and global resource management decisions and may take precedence over the pertinent science. Both legal concerns and public demands may override scientific inputs given the importance of our legal and political system.

Ultimately, however, science necessarily holds a preeminent place within resource decision making, as follows. The fundamental basis underlying decisions for public land allocation and natural resource management is the natural system. Within the current natural resource planning and management structure within the United States, science often serves as the preeminent source of knowledge about these natural systems. Thus science is intricately connected to such decisions, and decision makers involved in this arena often make concerted efforts to incorporate scientific results. Additionally, today's environmental regulations require inputs from scientific information. What bias,

or priority, decision makers should give to information in resource allocation decisions depends on the plethora of other factors that drive our planet and our lives.

Realizing this relationship, if society commits to including science within the decision making process (through, for example, legislation) for management of public lands and resources, science and decision makers must be connected to facilitate knowledge transfer in both direction. Linking science to decision making presents a challenge to all participants. This paper examines two specific processes in forging these links. First, we must explicitly define science so stakeholders recognize it as relevant and essential to public policy decisions. Then, we must facilitate transfer of useable, useful knowledge from the realm of science to the realm of policy via organizations, useful objects, or personal relationships. How decision makers incorporate this knowledge within the decision making process is outside the scope of this paper.

Mediation of the transfers between realms of science and public policy is the subject of a wide body of literature. After discussing definitions of science, we examine a subset of that literature on mediation related to boundary organization theory and its role in the decision making process (i.e., Cash et al., 2002; Parker and Crona, 2012; Carr and Wilkinson, 2005; others). As part of this research, we conducted a case study among scientists and related policy personnel within a university setting. We use this example and others to discuss potential changes to current boundary organizational theory and subsequent implementation within decision frameworks for public land and resource management.

The first step: what's in a name?

What is science? The catch-all use of the word has become increasingly common in the public domain. However, to promote science as an integral part of the decision making process, citizens, scientists, and policy makers must share a common, narrow, and valid definition of science. Scientists rely on this definition to defend the validity of their results. Decision makers use it to separate and evaluate the scientific component of a problem from other factors. The definition also boosts perceptions of legitimacy among citizens and other stakeholders (Cash et al., 2002; Lackey, 2007).

Strictly defining science can legitimize its role in decision making while still upholding the validity of other factors. Strictly defining science distinguishes science from other inputs to the decision-making process and allows decision makers to evaluate sources of uncertainty. Both of these factors aid in maintaining public confidence in the decision making process and in the validity of science. However, even outside the public domain, philosophical and scientific literature presents an incredibly wide array of definitions of science. These definitions tend to fall into one of four categories: hypothesis-driven; inductive; procedural; and constructed. Below, we sift through these definitions and present a well-rounded, utilitarian definition for use within public policy and by scientists alike.

What's in a name: the classical scientific method

Hypothesis-driven science is that which we first learn about as children, memorizing the steps of the scientific method from theory to hypothesis to experimentation to observation and conclusion (Nature Methods, 2009). With this definition, hypothesis-driven science is a specific, well-defined process as opposed to a

collection of truths which decision makers could use as trump cards (Freemuth, 2011). The foundations for this definition go back hundreds of years to great philosophers such as Descartes in the 17th century. The classical scientific method incorporates deductive reasoning, leading "from Ideas to Data" via controlled experimentation (Benjamin, 1949; Kell and Oliver, 2004). Experimental results then confirm or reject the original hypothesis.

In this strict definition, science exclusively begins with hypothesis formulation and continues with hypothesis testing (Nature Methods, 2009). Thus the hypothesis-driven definition of science excludes many categories of inquiry into the natural world. For example, it excludes "pseudoscience," data pattern recognition, or scientific claims which are not testable, falsifiable, or reproducible (Wong and Hodson, 2010). Note that excluding these other inputs from the definition of science does not necessarily exclude them from the decision making process.

This exclusive definition promotes long-term public trust as hypothesis-driven research reduces bias and promotes falsifiability and verifiability of scientific results, an important trait of scientific inquiry. First, a formally-stated hypothesis is open to falsifiability by another researcher following the scientific method. Second, verifiability follows from the rigorous nature of the experimental phase of hypothesis-driven science: the same experimental steps should produce with the same results thereby verifying the conclusions (Wong and Hodson, 2010). However, researchers and decision makers must recognize that hypothesis testing cannot eliminate the "invisible hand," that is, an unseen preference for a particular choice (Lackey, 2007). Hypotheses-driven research is still susceptible to biases introduced by normative (pre-chosen) hypotheses (Boumil and

Berman, 2010; Lackey, 2007). Normative hypotheses inherently contain bias as they reflect preference instead of fact, by including connotative language such as “alter,” “degrade,” or “healthy” (Lackey, 2007). Reducing the use of normative hypotheses can aid the overall reliability of the hypothesis-driven scientific method.

Classical physical, chemical, and biological experimental science follows the scientific method and lends itself well towards applications in resource or land management. In a decision about open-water oil field locations and lease sales, policy makers might incorporate scientific results delineating expected environmental repercussions of potential oil spills. For example, hypothesis-driven research has shown that exposing fish embryos to crude oil can cause genetic damage and mortality (Carls et al., 1999). Such research might influence decision makers when considering oil drilling and exploration within known spawning grounds. As another example, Coates (2005) used the scientific method to show that crops can grow in waste water from mine tailings, providing a use for mine waste and a potential for mine remediation. Scientifically-validated remediation techniques for mine tailings may allow land use planners more leeway for mining permits.

The inductive approach

The direction of the classical scientific method is from Ideas to Data, that is, deductive reasoning. On the other hand, Kell and Oliver (2004) define inductive science as movement “from Data to Ideas.” This definition is data driven. “Data mining,” statistical inference, generalization from specific cases, mapping (e.g. epidemiological studies), and other similar observations derived from data (such as field observations) subsequently provide conclusions via detailed analysis. Thus, the inductive definition of

science is broader than hypothesis testing, and includes reasoning from example. Deductive science and inductive science are not always mutually exclusive but may continuously support and inform one another, ideally via iterative cycling – Data to Ideas to Hypothesis and back to Data via experimental testing and verification (Kell and Oliver, 2004). It is important to recognize that this cycle does not always proceed in that order, but rather the emphasis is on iterative cycling between deductive and inductive reasoning.

Although not as explicitly-stated or formalized, the roots grounding this definition of science may run nearly as deep as those of the scientific method. The most famous example of data providing an idea for investigation is the famous, unverified story about Newton and the apple fall (Krull and Kulikov, 2006). James Clerk Maxwell, another one of the greatest physicists in human history, made key advances in optics which resulted from his observations about color mixing from spinning tops. As far as we know, Maxwell wasn't hypothesis testing or designing an experiment when he made these breakthroughs; he was curiously observing and exploring the wealth of data in the world around him (Goldman, 1983).

Inductively-driven science has increasingly prospered in the last century as powerful computers and instrumentation progress allow scientists to exploit previously-untapped sources of data, such as large-scale ocean temperature monitoring. Monumental increases in the speed of data examination and processing allow rapid, through examinations for pattern and ideas. Therefore, using this somewhat broader definition for science may aid decision makers as inductive results are often more plentiful than hypothesis-driven research.

Unfortunately, using a broader definition also has disadvantages. For one, inductive scientific results may have higher rates of incorrect correlations than hypothesis-driven science, since correlations are more readily found in data inductively, e.g. via data mining, than they are to prove via hypothesis testing (Nature Methods, 2009). Inductive science does not always allow for falsifiability or repeatability. If the scientific result is inductive only, without experimentation, then there is no way to repeat results. A scientist could simply examine the same data but cannot truly test the conclusion without a hypothesis. Surveys of scientists show that they recognize these problems with inductive science, and most uphold the standard of experimental methods over non-experimental ones (Wong and Hodson, 2010). In general then, inductive science coupled with hypothesis-driven research is a stronger foundation for scientific conclusions than inductive methods alone.

Epidemiological studies, famous in scientific circles since John Snow and his London map of cholera (which disclosed that local beer drinkers were mysteriously immune), are an example of data-drive science (Goldstein, 2012). The basis of epidemiology is data collection for mapping, tracking, categorizing, and analyzing human or animal diseases. In fact, the hypothesis-driven science may begin at the end of the epidemiological study, with the formulation of a hypothesis about the cause of the specific disease. This iteration exemplifies the link between deductive and inductive reasoning.

Climate science is inductive reasoning applied to observations about the earth's temperature, weather patterns, and circulations (IPCC, 2007; Lucarini, 2002). Although founded on massive amounts of global data but is not provable via "application of the

usual scientific validation criteria" (Lucarini, 2002). Climate data show a relationship between atmospheric temperature and atmospheric concentrations of certain gases, the "greenhouse gases." This link provides a good example of some weaknesses of inductive science. To rigorously verify the correlation on a global scale is simply impossible. Climate science, then, is not falsifiable in the traditional sense. Nor is there anything repeatable about the data set of global temperatures and climatic conditions.

Decision makers are increasingly attuned to the economic and social consequences of climate change. Nonetheless, other stakeholders continually question the underlying science due to its inductive rather than deductive nature, the uncertainties involved, and its lack of verifiability or falsifiability. Decision makers might bolster long-term public confidence by publicly addressing these uncertainties and differentiating between the inductive and deductive definitions of science when discussing climate science, and, indeed, any inductive scientific results. Of course, public acceptance of policy solutions to climate change may prove to be even more difficult that public acceptance of the science behind the decision making.

Although inductive science does have inherent flaws, we cannot discount it. Brilliant minds have produced a wealth of knowledge using inductive methods. Thus in moving from a strict hypothesis-driven approach to inductive science, decision makers have more breadth of results upon which to draw. Additionally, since many informed citizens probably view our examples and inductive science as "real" science, legitimacy of the decision-making process is upheld when using this definition.

Science as a process

A third group of definitions group interrelated scientific and institutional processes together (van Dijk, 2011; Kell and Oliver, 2004). The American Physical Society defined science as a "disciplined quest to understand nature in all its aspects" (Macilwain, 1998). Carr and Wilkinson (2005) define sciences as a "special learning process." These definitions broaden science beyond inductive or hypothesis-driven methodologies. Some examples of scientific processes include journal publication, public presentations, collaborations, and peer review. These scientific processes are not always directly tied to the deductive or inductive methods of investigation but have gained acceptance both within and outside the scientific realm as being "science" (van Dijk, 2011; Wong and Hodson, 2010).

Including these example by defining science as a process poses several problems for decision makers. Whereas the hypothesis and inductive definitions provided a tool to easily distinguish scientific from non-scientific pursuits, defining science as a "quest" or a "special process" blurs that line. That blurring causes increased uncertainty and increased susceptibility to error. Also, the vagueness of the process definition precludes falsifiability. Decision makers suffer as a result when "science" loses credibility and legitimacy in the public eye and incorporating science into resource management becomes increasingly difficult (Cash et al., 2002). Furthermore, defining science as simply being special process does not innately distinguish it from any other realm of human investigation, and leaves the door open for normative science (Lackey, 2007).

As an example, consider scientific modeling. Modeling is a specific scientific process, yet it is not necessarily restricted by the scientific method or by data-driven

inductive reasoning. Modeling fits more clearly with the "quest" or "process" definition since creating models to portray natural phenomenon is obviously a "disciplined quest to understand nature." Modeling efforts do not usually meet the criteria of science being verifiable and reproducible. Known scientific laws or equations may govern model algorithms, but algorithms are generally predictive in nature and therefore not falsifiable in the present time. Nor is modeling reproducible – successive tests of a modeling algorithm with slightly different inputs can produce enormous variations in response, e.g. the well-known "Butterfly Effect" (Palmer, 2008). Decision makers often include models in the "scientific" component of their decision but by doing may sacrifice legitimacy.

Science as "truth"

The broadest definition of science is science as a "social and cultural construction" (van Dijk, 2011), whereby "science…is whatever scientists do" (Nature Methods, 2009). Gottfried and Wilson (1997) describe science as "a communal belief system." This definition approaches the idea of "science as truth" instead of science as a rigorous process (Freemuth, 2011). Such social or cultural definitions inherently include normative science, and accept that "social, cultural, economic, political, and ethical forces determine the priorities" for science (Wong and Hodson, 2010). Scientists may personally and professionally embrace this definition of science and the idea of science as truth.

The negative connotations of this definition imply that popular opinion on a natural or environmental topic can substitute for hypothesis-driven science, or that science can be a "trump" card in the policy arena by superseding other decision-making

factors (Freemuth, 2011). An additional negative result may be that scientists confuse their personal values with science and the introduction of bias and normative hypotheses into scientific inquiry (Lackey, 2007).

Allowing culturally-based science equal footing within the decision making framework may also escalate uncertainty beyond acceptable bounds for decision makers. For one thing, culturally-defined science is neither falsifiable nor verifiable, and thus also problematic for estimating associated uncertainties. Science based on social or cultural beliefs may also be non-relevant to decision makers or incorrect so often as to be useless for them, given the goal of sustainable management of public lands and natural resources.

Unproven scientific ideas can become social or cultural norms even though they are simply theoretical in nature. Examples include the Standard Model of Particle Physics, quantum chromodynamics, and, dare we say, climate change (Gottfried and Wilson, 1997). Many such theories are not inherently relevant to decision making processes for sustainable land and resource use; on the other hand, climate science has significant implications for these decisions. Since global climate change as a scientific concept has become a social and cultural norm rather than a scientific result, the public associates climate science with social upheaval and erroneous results. These problems have limited the successful application of climate science for decision makers in resource management.

On the positive side, a cultural definition of science affords local or indigenous knowledge equal footing with more traditionally-accepted scientific approaches. In fact, local knowledge, where available, is imperative for land management decisions, as indigenous groups often recognize natural phenomena that formal researchers may

overlook (Affolderbach et al., 2012). To alleviate confusion, decision makers should recognize indigenous knowledge as a relevant and necessary factor but take care to distinguish it from the scientific factor. This tactic would uphold a more-narrow definition of science (with the commensurate advantages) whilst still preserving local knowledge or science within the decision-making framework.

Given this continuum of definitions, which provides the most efficacy for public policy decisions related to resource management and land use planning? A hypothesis-driven definition is the most classical, "pure" definition of science, but the classical scientific method may be too exclusive and eliminate too many relevant scientific results. Defining science as a social construct or as institutional processes is too inclusive and fallible for many stakeholders to accept.

Using the middle ground, an inductive or iterative-inductive definition of science, bridges the gap between these two definitions. Inductive methodology provides reasonably firm footing for decision makers and is likely to promote credibility and legitimacy among stakeholders. Inductive scientific results that are subsequently tested using the hypothesis-driven approach provide the strongest foundation for decision makers. Such science would meet the criteria of verifiability and falsifiability, minimize uncertainty and normative science, and promote public trust. Thus we define science either as conclusions obtained and verified through conscientious, bias-minimizing application of the scientific method or as information obtained or recognized from data and then verified via the scientific method. With this idea in mind, the rest of this paper considers "science" or scientific "knowledge" as information about the natural world obtained through some combination of inductive reasoning and hypothesis testing.

Building Bridges Between Science and Policy

Having explicitly defined science, and accepting that science has a valid, necessary contribute to decision making for land and resource management, we face another problem: how to facilitate the ready transfer of knowledge from science to decision makers. A wide body of literature analyzes numerous methods for this transfer. Boundary organization theory is one such method. This concept was developed at the end of the twentieth century through the work of Gieryn (1995), Guston (1999, 2001), and others and has since been broadly applied to decision making theory (e.g. Carlile, 2002; Jacobs et al., 2005; Sapsed and Salter, 2004).

Boundary organization theory promotes the idea that the boundary between scientists and decision makers can be overcome through organizational constructs. Properly constructed organizations can bridge this boundary and thereby facilitate the use of scientific knowledge within the policy regime (Cash et al., 2002; Cutts et al., 2011; Guston, 2001; Franks, 2010; Michaels, 2009; Miller, 2001). The "boundary" between science and decision makers may be comprehensional, perceptual, social, cultural, conceptual, or organizational (Carr and Wilkinson, 2005; Cash et al., 2002; Michaels, 2009).

Boundary organization scholars embrace the fluidity of the boundaries between science and policy. The lines between science, policy, and other interests such as industry often blur , and multiple diverse stakeholders groups often become vested in boundary organizations (Parker and Crona, 2012; Affolderbach et al., 2012; Safford and Norman, 2011). Although capturing the resulting complexity within a comprehensive framework

may be impossible, continued efforts to mediate between science and policy aid difficult science-based decisions for environmental resource management.

In the broadest sense, a boundary organization connects "knowledge to action" (Cash et al., 2002). Carr and Wilkinson (2005) define a boundary organization as a "forum" where multiple participants intermingle and multiple knowledge systems interact. Miller (2001) refers to social constructs that "mediate between the institutions of science and the institutions of policy." Guston (2001) says "boundary organizations are formal organizations designed to exist at the interface of research and policy organizations and facilitate communication and collaboration between them." In general, then, boundary organizations convey scientific knowledge to decision makers as part of a dynamic, iterative, interactive process among invested participants.

Boundary organizations translate and transfer knowledge from scientist to decision makers iteratively, build and maintain long-term relationships among participants, and mediate between scientists and decisions makers (Cash et al., 2002; Franks, 2010; Miller, 2001; O'Mahony and Bechky, 2008; Pietri et al., 2011). Successful boundary organizations maintain salience, relevance, and legitimacy of information flows across the boundary (Cash et al., 2002; Cutts et al., 2011; Pietri et al., 2011). Note that the relationship building process is crucial to boundary organization function, and indeed may exist outside a formal organization (Smith and Kelly, 2003; Franks, 2010). Without functional and interactive personal relationships between participants, trust and credibility will suffer, and resulting decisions will be shunned by the collaborating groups (Cash et al., 2002). Finally, boundary organizations serve to mediate between conflicting values throughout the decision making process.

While building relationships, mediating collaborative work, and moving knowledge across the boundary, boundary organizations also simultaneously operate to *maintain* boundaries (Cash, 2001; Franks, 2010; Guston, 1999). Maintaining boundaries allows participants to retain credibility with their own stakeholders. Scientists must maintain status and credibility within their discipline to foster credibility outside it. Decision makers need to maintain credibility with their constituents in order to promote positive public opinion, especially in the heated realm of public land debates (Cash, 2001; O'Mahony and Bechky, 2008). These separate credibilities contribute to the efficacy of decisions based on the credibility of the boundary organization as a whole (Pietri et al., 2011).

Boundary Organization Examples

The Decision Center for a Desert City (DCDC) is a classic example of a boundary organization in resource management. The National Science Foundation (NSF) explicitly created the DCDC via a grant to a public university with the purpose of bridging the gap between science and policy for water resource management in the desert Southwest (Parker and Crona, 2012; White et al., 2008). Stakeholders in the DCDC included the university, scientists, decision makers, and the NSF (Cash et al., 2002; Parker and Crona, 2012). Similarly, and also funded by the NSF, Sustainability of semi-Arid Hydrology and Riparian Areas (SAHRA) is a boundary organization that produces "science to help communities manage their water resources in a sustainable manner" (SAHRA, 2001).

Agriculture Extension (AgEx) –type constructs are another boundary organization example, where farmers hold the role of decision makers responsible for their land management. AgEx offices mediate between scientists and farmers, disseminate scientific

information to the general public, and interact with other decision makers (Carr and Wilkinson, 2005; Cash, 2001; Franks, 2010). The scope of AgEx organizations emphasizes the multi-dimensional aspect of boundary organization theory (Cash, 2001). Resulting changes in farmer practices due to AgEx efforts have improved resource management, for example by reducing superfluous fertilizer use or enhancing water management strategies (Babcock and Silvertooth, 2012; Cash, 2001).

Although these boundary organizations meet with some success, they are often unable to attain credibility, salience, and relevance and therefore often fail as a construct for knowledge transfers and implementation (Cash et al., 2002). For example, in spite of being expressly created to fill the role of a boundary organization, the DCDC suffered from constraints imposed by its funding organization and its institutional framework (Parker and Crona, 2012). These constraints limited flexibility and resulted in a perceived gap in legitimacy and salience (Parker and Crona, 2012). As a result it lost credibility with its stakeholders. SAHRA suffered similar setbacks due to communication problems, scientific ambiguity, and organizational structure (Eden, 2011).

AgEx organizations also struggle to maintain credibility, legitimacy, and salience as boundary organizations (Cash, 2001). Problems with maintaining legitimacy frequently arise when scientists presume that laboratory results are transparently transferable to field. Salience may suffer as farmers often remain convinced that scientists do not understand the difficulties of making a livelihood off the land. Credibility is impaired due the divide between the farmer's field and the laboratory: "16 hours in a laboratory differs from…16 hours on a horse" (Carr and Wilkinson, 2005).

Common use of scientific jargon by scientists only exacerbates the problems (Pietri et al., 2011).

These examples reveal some of the difficulties boundary organizations face in their struggle for effectiveness. Other examples abound (Affolderbach et al., 2012; Agrawala et al., 2001; Cutts et al., 2011; Franks, 2010; White et al., 2008; others). Nonetheless, regardless of the difficulties resource and public lands managers need timely, productive, and relevant science (Lackey, 2007; Pietri et al., 2011; Smith and Kelly, 2003). The boundary-spanning individual provides another mechanism that may defray these problems and encourage these knowledge transfers.

Boundary-Spanning Individuals

The boundary-spanning individual stands in the gap between the two realms of science and policy. He must maintain credibility in both worlds in order to accomplish the objectives of a boundary construct. This individual fulfills the relationship role of the boundary organization, and subsequently he can use these relationship bridges to mediate between the groups while transferring and translating knowledge.

In fact, previous work indicates that boundary organizations offer the most value in the decision making process when a specific individual acts to fill the role of mediator and knowledge broker (Cutts et al., 2011; Parker and Crona, 2012; Michaels, 2009). For example, Parker and Crona (2012) noted that the DCDC enjoyed success only after employment of a specific person who personally maintained credibility with researchers and policy makers. The relationships between farmers and scientists in AgEx organizations are another example. AgEx offices may fail completely at effecting knowledge implementation unless one scientist shoulders the role of mediator or takes

personal responsibility for making his research salient, legitimate, and credible to farmers (Cash et al., 2002).

The role of boundary-spanning requires a unique and dedicated individual, sometimes at personal expense. Time spent with the boundary organization detracts from availability to one's primary group and therefore from promotions or similar benefits, i.e., incentives are misaligned (Brownson et al., 2006). As a scientist, straddling the divide between science and policy may compromise objectivity, real or perceived (Brownson et al., 2006). Credibility may suffer if decision makers or social groups view a passionate boundary-spanning scientist as biased. These problems are exacerbated in issues about public lands and resource management due to the inherent uncertainty of the applicable science and the contentious nature of these issues. However, the realm of public policy for land use and resource management is desperately in need of independently-motivated individuals with the knowledge and skills to mediate the boundary. Both groups stand to gain by minimizing these difficulties or providing incentives to collaboration.

Although we leave further analysis of the role and efficacy of boundary spanning individuals and of principal agent theory to the reader, it is important to note that boundary-spanning individuals can act outside formal boundary organizations. A scientist or decision maker may choose to build personal relationships across the boundary, regardless of the existence of a boundary construct. However, often a boundary-spanning individuals lack the impetus to resolve large-scale resource management issues while acting independently from a boundary organization. Thus often a boundary organization must act as a forum to promote the efficacy of boundary-spanning individuals.

Boundary Objects

Boundary organizations may act as forums to promote specific objects conducive to the roles of scientists and decision makers. Such boundary objects can mediate the transfer of science to decision makers (Cutts et al., 2011; Star and Griesemer, 1989; Zeiss and Greonewegen, 1989). Star and Griesemer (1989) provide the consummate definition: "scientific objects which inhabit several worlds (…) *and* satisfy the informational requirements of each of them." Henderson (1991) notes that these objects can mean "one thing to some group members who use them and something else to other members." The value of these objects lies in their flexibility for different stakeholders to use them in different ways as needed.

Boundary objects have the potential to enhance the functioning of a boundary organization. Effective boundary objects promote boundary organization goals by establishing "a shared syntax or language, … a concrete means for individuals to specific and learn about their differences and dependencies" (Carlile, 2002). If credible with stakeholders, these objects can translate and transfer knowledge while maintaining credibility, legitimacy, and salience on both sides of the boundary (Cash et al., 2002; Star and Griesemer, 1989). As with the boundary organization itself, achieving credibility for a boundary object often requires negotiation amongst participants. Boundary objects minimize bias and maximize credibility by allowing stakeholders to trade information and negotiate while maintaining their status within their respective groups (Sapsed and Salter, 2004).

Boundary objects can be literal objects, e.g. maps, Geographic Information Systems (GIS), brochures, or buildings; or symbolic objects, e.g. the internet or climate

models (Zeiss and Groenewegen, 1989; Carlile, 2002). A scientific journal can act as a boundary object by allowing decision makers to access research results applicable to a specific land use or resource question. Scientists and decision makers can use internet GIS platforms to input or interpret relevant information (Carlile, 2002; Sapsed and Salter, 2004). In either case, boundary organization stakeholders have to accept the boundary object as legitimate and be willing to participate in its development. Without these actions, a boundary object's utility will suffer or fail. Thus boundary objects tend to be more effective when concurrent user interaction facilitates comprehension and relationship-building (Zeiss and Groenewegen, 1989). For example, internet sites may provide a "repository" boundary object where scientists and decision makers can access knowledge while using forums to interact and build relationship, comprehension, and salience (Cutts et al., 2011).

With such interactions around a boundary object, decision makers can prompt scientists to produce science that relevant to specific questions surrounding a land use decision. These interactions also promote scientific results which themselves meet the objectives of salience and legitimacy (Cash et al., 2002; Cutts et al., 2011). In this scenario, the boundary object sustains the organizational goals of knowledge transfer and translation, relationship building, and mediation. The boundary object fulfills these objectives between personal actors while importing additional benefits, such as neutrality, into the science-decision making loop. Thus boundary object may be a bridge for personal relationship building while facilitating boundary maintenance.

A Case Study: The Environmental Research Building at Boise State University

With the goal of understanding barriers and bridges between science and policy participants within the context of boundary organization theory, we surveyed faculty and students from several different departments in one specifically designed building at a research university. The case study aims to interrogate three main topics, as follows: 1) how relevant scientist and academics view the relationships between science and public land resource management in the United States; 2) the public research university's efficacy as a boundary organization; 2) boundary object utility. Finally, we extrapolate these answers to a broader forum including other universities and non-university affiliated decision makers.

Previous literature has examined the public university's role as a boundary organization or as an agency to house boundary organizations, both as concerns boundaries between departments within the university and boundaries between university agencies and the larger community (e.g. Parker and Crona, 2012; Tuunainen, 2005; White et al., 2008). The university can theoretically fulfill the boundary organizational role in either scenario. On the one hand, the university acts as an umbrella whereby participants from differing disciplines, i.e. academic departments, can explore cross-disciplinary issues for knowledge translation and transfer while building relationships. "Can" is the operative word in this sentence, and this case study investigates the efficacy of that role and reasons for its fulfillment or lack thereof. On the other hand, a university may act as a passive construct, housing different disciplines without attempting to pollinate cross-disciplinary interactions. We suspect that the decision of a public university to shoulder the role of a boundary organization is an

institutional corollary to a scientist's personal decision to become involved with public policy, and the same for the inverse. (It is important to recognize that these personal (for a scientist) or institutional (for a university) decisions are impacted to no small extent by a growing movement to promote inter-disciplinary work. For example, the NSF often solicits inter-disciplinary grants, and the commensurate funding is powerful incentive.)

This university houses the Department of Geosciences and the Departments of Political Science, Public Administration and Public Policy, Community and Regional Planning, and Civil Engineering within the Environmental Research Building (ERB) on campus (see Figure A.1). (This paper refers to "policy" faculty or personnel as members of any of the latter three departments.) The policy faculty at Boise State have notable expertise in public lands use, environmental planning, and resource management, among other topics. The Department of Geosciences has experts in environmental science, contaminant transport and remediation, fire management research, hydrology, space-based remote sensing, and additional subjects. These areas of expertise are complementary, and one can envision a regional land use planner consulting similar scientists and reviewing similar scientific results when faces with land management decisions. In addition, faculty within the political, administration, and planning departments are integral to informing decision makers in the state of Idaho and throughout the West.

Completed in 2011, the university goals for the ERB are to "encourage and support interdisciplinary collaboration," "forge synergies," and to "enhance research aimed at the pressing issues of the West, including the environment, energy, transportation, water, land use, and community planning." Supporting interdisciplinary

collaborations requires fostering participation between stakeholders across departmental lines and necessarily requires transferring information between the academics in them. Without this information transfer, and additional relationship building and mediation between departments, interdisciplinary collaboration would fail and the germane research topics would flounder. Thus these explicit goals voluntarily enshrined the institution with the boundary organization role as pertains to the science and policy departments within the ERB.

Figure A.1: The Environmental Research Building at Boise State University, Boise, Idaho

Considering the university's goals for interdisciplinary collaboration and its assumed role as a boundary organization commensurate with those goals, we now add

another category of literal object to those that may be considered boundary objects (Sec 3.2). We hypothesize that the ERB was created, in part, to act as a boundary object.

We now examine this potential role of the ERB in conjunction with the discussion and definitions presented in Section 3.2. Considering the Star and Griesemer (1989) definition, the ERB houses both the science and policy departments and does satisfy "the needs of both," in that all departments separately use the building for their own needs, e.g. for classroom instruction, for research, for faculty meetings, and for office space. Yet the building is not a "scientific object which inhabits several worlds" but instead several worlds inhabit this object. In this sense, it is perhaps counterintuitive to consider a building as a boundary object when most of the literature about such roles encompasses (generally small) objects used by different worlds, where here we consider a large object that the worlds themselves inhabit. Nevertheless, the ERB is maintained by a boundary organization with goals commensurate with the role of a boundary object and we consider its potential role as such.

Boundary objects also act to transfer knowledge across the boundary (Cash et al., 2002; Star and Griesemer, 1989). We hypothesize that the ERB acts to transfer knowledge across the boundary between the science and policy departments. For example, both groups have posters, flyers, brochures, and monitors displaying information specific to their own discipline distributed throughout the building. We hypothesize that these exhibits, which are part of the ERB, transfer knowledge between the two groups we have delineated, which is a function common to all boundary constructs. We liken this role of the ERB to a boundary organization journal containing multiple articles – each poster and brochure within the ERB acts to translate and transfer

knowledge in a corollary to individual articles or diagrams within a brochure or publication. Yet, the role of the ERB within the boundary organization (the university) creates the ERB's potential role as a boundary object, housing these departments and exhibits in such a manner as to foster collaboration between the disciplines.

The building also "provides a basis for negotiation" (Sapsed and Salter, 2004) in common forums and meeting spaces where parties can trade information and act across interdepartmental boundaries. Carlile (2002) promotes that boundary objects allow stakeholders to learn about their similarities, differences, and interdependencies, while promoting organizational goals. The ERB is promoting an organizational goal of cross-disciplinary collaboration by its existence. The case study results provide a basis for assessment of the building's success in that promotion and for addressing the preceding, principal part of Carlile's definition.

Methods

We conducted an email survey of 141 student and faculty members of the Departments of the Department of Geosciences and the Departments of Political Science, Public Administration and Public Policy, and Community and Regional Planning. We did not survey the Civil Engineering (CE) personnel in order to focus on the scientists and policy members in the building, although we recognize that CE does inform policy decisions for resource management.

The primary objectives of the survey were twofold: 1) to investigate interdisciplinary boundaries or bridges as evidenced by personal opinions on the definition of science and on the role of science and scientists in decision making for

public lands and resource management; and 2) to assess the role of the university and the ERB as boundary constructs.

The survey included 19 questions that asked for numerical answers, for opinions, or for definitions. Survey protocols ensured anonymity in accordance with ethical codes of conduct for research on human subjects. Respondents had the option to email responses or to submit anonymous hard copies to the administrative staff. We collected surveys over a period four weeks.

We received 48 completed surveys and 7 responses declining the survey directly. Response rates were highest in the Department of Geosciences, with 42% of students and 55% of faculty responding. Thirty-three percent of policy faculty responded, and only 16% of policy-associated graduate students. The significantly higher response rates from the geosciences participants are likely a consequence of the survey being conducted by a member of the Department of Geosciences. Future surveys could avoid this bias by conducting the survey anonymously.

Since the case study necessarily involves non-probability sampling problem, extrapolation of results to the general population is problematic. However, our approach is suitable given that a primary goal is to understand the social interactions and cultural constraints which may impinge upon cross-boundary research and synergies (Rosner, 2011). The survey protocol minimized response bias by choosing non-normative language and allowing responders to submit any answers instead of using list-based responses.

Results and Analysis

The survey asked a series of questions calling for opinion-type responses on the definition of science and the role of science in decision making. It also asked for a list of items that decision makers should consider "in a public policy decision about land use management…or resource management." We designed these questions around our first goal of assessing barriers or commonalities between the thought processes and value ideals of the two groups (the science and policy departments) as evidenced by personal opinions on the definition of science and on the role of science and scientists in decision making for public lands and resource management.

We grouped the definitions of science corresponding to the 4 formal definitions they most nearly represented: hypothesis-driven, inductive-iterative, institutional processes, or cultural construct. Commensurate with our efforts to avoid response bias, we did not mention any of these terms or definitions in the questions but simply asked the responders to define science in any way they choose fit. Nevertheless, most responses actually did incorporate keywords from our definitions, such as "scientific method" and "inductive reasoning." We analyzed responses that did not include keywords to interpret the general sense of the definition. We assessed ambiguous responses in an independent iterative manner, classifying each response, recording the classification, and then after each classification shuffling response orders and reassessing, to avoid interpreter bias contamination.

Final grouping of responses on the definition of science encompassed all four definitions: 45% percent of definitions were hypothesis-driven, 30% were inductive, and

20% were procedural. Only one answer was deemed suitably broad as to fall into the social and cultural definition of science:

> "the study of science and technology studies also overlaps with the arts and humanities and philosophy. So, in my world view science is pretty much all encompassing. Setting artificial and narrow disciplinary boundaries around what science is (and does) only serves to limit our capacity for collaboration."

The responses highlight one particular difference between the two groups. One might reasonably expect scientists to endorse a more rigorous definition of science than policy members. Indeed, the scientist group was responsible for 80% of the definitions grouped as hypothesis-driven. Overall, the distribution of definitions also highlights the lack of a single, accepted, common definition among all participants, both scientists and decision makers. This deficiency is a critical problem that both scientist and policy makers should strive to remedy. A standardized definition of science common to all stakeholders will foster credibility and should be a priority, but it will be difficult to achieve we are sure.

The survey queried respondents about factors for land and resource management decisions, and again sought to avoid response bias by minimizing normative language and allowing for written answers. Thirty-three percent of students and faculty members emphasized that decision making involves a "weighting" of factors and trade-off analysis. Both scientist and policy constituents cited the uncertainty inherent scientific results as a complicating factor for decision makers (see

Table A.1). Sixty percent of responses from both groups stated that relevant scientific results should be included “where possible” and “as appropriate.” Responses underscored a need to balance the scientific component with other factors involved in the decisions. Here we see a bridge between groups and not a gap – both embrace the need for balance and demonstrate knowledge of the multiplicity of entwined factors that decision makers face.

It is interesting to note that approximately 25% of responses both from the science and the policy groups expressed deference to the role of public opinion as a factor in the decision making process, delineating the primacy of the public opinion factor as essential to upholding our democratic system of government. In stark contrast, one answer explicitly stated “though public opinion and public values are often taken into account in policymaking, I generally do not think they should be.”

When asked to list specific factors which decision makers should incorporate, respondents overall listed between 0 and 10 items (see Table A.2). Policy faculty tended to list more factors than scientists as demonstrated in the statistic shown in Table A.2. One policy faculty listed ten factors in his response, the largest number of responses of anyone in the survey. These statistics again highlight differences between the groups. The partition in number of responses embodies the expected expertise of each group: the policy faculty contains members with expertise in decision making as related to public land use and resource management while the geosciences department specialty is, obviously, science.

Table A.1: Selection of responses concerning incorporation of science into decision making which address the uncertainty in the decision making process

Respondent	Response
Geosciences faculty	One should never consider a single factor as being supreme. All factors should be considered in concert. No factor should trump all others.
Policy Faculty	There is no one most important factor and trying to identify one is futile and frustrating.
Policy Faculty	There are always uncertainties, trade-offs, and unanticipated side effects in these kinds of decisions.
Geosciences faculty	This is an impossible question to answer.
Geosciences Student	It is impossible to keep everybody happy.
Policy Student	Trying to find a middle ground or decision that brings as many people together as possible is the most important factor in public policy decisions.
Geosciences faculty	When policy decisions fall in the context of science, scientific results should be considered. However…absolute truths are not deliverable under the scientific method.

Nevertheless, the cohesion within both groups concerning the need for science in decision making was underscored throughout these responses. That observation combined with the plethora of responses to this question demonstrates the complexity of the issues surrounding management and use of natural resources and public lands, as well as the complexity of thought processes with which both scientists and decision makers consider such important scientific and regulatory questions. Many values compete for dominance, all of which contain some uncertainties. Decision makers face a daunting task to balance the factors involved while upholding our democratic system of government.

Table A.2: Number of items mentioned per person for "other sources of information that decision makers should consider," rounded to nearest whole number; note the policy faculty median and standard deviation (*S*).

Group	**Scientist**		**Policy**	
Subset	**Faculty**	**Student**	**Faculty**	**Student**
Median	3	3	5	3
S	1	2	2	2

Two subsequent questions investigated opinions concerning the role of individual scientists within public policy. Opinions were mixed and, again, often reverted to the default "it depends," as exemplified in this response:

> "It is really up to each individual scientist to judge for herself or himself if it's appropriate for them to be involved, and whether or not they feel comfortable in the public arena. Nothing should compel a scientist to be involved in policymaking."

Over 50% of responses indicated that if scientists choose *not* to contribute via specific research programs or dedicated boundary crossing, they should still participate as citizens. Citizen responsibility is especially vital given that over 25% of survey participants listed public opinion among the most important factors in a decision. Participation by citizen scientists can augment the intelligence and core competency contained within the body of public opinion. Intelligent and knowledgeable citizen opinion will allow decision makers to publicly rely on well-defined scientific conclusions. Such reliance can produce land management plans and resource use plans which are sustainable in the long-term. Since over 30% of respondents listed

sustainability as an essential goal for public policy decisions on resource issues, having scientists participate in their scientist role or the citizen role is equally important.

We observe that whether in a citizen or scientist role, individuals may act to translate and transfer results in the role of boundary-spanning individual. These functions can occur both between scientists and policy participants in the ERB and between scientists or policy members and the general public. These survey results reveal differences between the groups and a possible opportunity for science and policy participants to choose to become a boundary-spanning individual within the boundary object (ERB) and the larger boundary organization (the university). This position could be realized in a plethora of different ways, such as a university-defined and funded construct or a personal decision to dedicate time to inter-disciplinary work.

The previous questions disclose thought pattern convergences and divergences between groups. The results also indicate the need for collaboration, but the literature demonstrates that many factors erode collaborative efforts. Here we analyze the components of the boundary itself within this university setting, as demonstrated by survey responses to a question about “barriers to interactions between the Geosciences and Public Policy departments.”

Table A.3 shows responses listed by specific barrier, number of times mentioned, and group of the responder who listed it.

Table A.3: Barriers listed by faculty in the ERB to interactions; note that respondents could list any number of items.

Barrier	Frequency	Group Listing It
Time	5	gf,pf*
Culture	5	gf,pf
Poor understanding of applications	5	gf
Location in building	2	gf,pf
Well-articulated problems	2	gf,pf
Incentive	2	pf
No common overlap	2	pf
No group seminars	1	gf
No group social activities	1	gf
Poor understanding of decision methods	1	gf
Narrow research focus	1	gf
None	1	gf
Tenure requirements	1	pf

*gf=geosciences faculty; pf= policy faculty

Time, culture, and a poor understanding of applications across the departments were among the most common responses. Time constraints are universal and obviously act as a barrier to the effective action of boundary constructs both internally and externally to the university setting. In fact, time constraints on real-world decision makers are more stringent than those on university personnel. These limits prevent a deeper investigation of the pertinent science and hinder the development of personal relationships (Parker and Crona, 2012). Similar arguments apply to the cultural divide between the groups. While the cultural divide in a university setting is moderated by the commonality of the university experience, such a cultural bridge does not normally exist for decision makers and scientists. In this case, even the action of the university and the subsequent use of the ERB seem to have left significant barriers in place between the groups, as evidenced by the survey responses (Table A.3).

The response of "poor understanding of applications" perhaps uniquely captures why boundary organization theory has traction for science and decision maker interactions outside the university setting. Decision makers struggle to find access to relevant scientific research, while scientists may not recognize the applicability of their research or area of expertise to policy makers (Cash et al., 2002). Crossing those gaps means forming bridges, whether by boundary organizations, boundary objects, or boundary-spanning individuals. Educating scientists about the needs of decision makers is an important first step. Simultaneously, decision makers need to gain understanding about scientific methodology, available research tools, and potential sources of knowledge.

Geographical location within the building was listed twice as a problem hindering interactions between departments. Once again, this problem is likely more problematic to real-world decision makers than to ERB personnel. In the case of the ERB, personnel from the scientist and policy departments are scattered across several floors. In a real-world scenario, scientists and decision makers are likely scattered across a city or even across the country. On the other hand, respondents noted in-building location as an obstacle to intradepartmental interactions, citing barriers to departmental coherency as problematic for research development. This situation presents a conundrum for both the ERB's effectiveness and for real-world organizations. Policy-scientist interactions may be enhanced by co-located offices, but this arrangement may hinder colleague and peer relationship building, especially for early-career decision makers. The conundrum reveals the need for an individual who can move freely between the two groups to enhance cross-boundary transfer while maintaining individual group cohesiveness. It is interesting to

note that this two-fold role also mirrors the role of a boundary organization to bridge *and* maintain boundaries.

In order to more fully understand the role of the ERB as a boundary object, the final questions solicited information about changes in interactions across departments before and after the move to the ERB. If the ERB is effective as a boundary object, after a year and a half housed together in the building interdepartmental interactions and collaborations should have increased. However, less than 10% of responses showed changes in the number or patterns of interactions occurring either among students or faculty, and the survey revealed no significant change in patterns of collaboration. And perhaps this stasis is not startling. In the words of one responder:

> "Quite frankly, the idea that you could put people from very different research areas together in a single building and expect intense, sustained collaboration to magically occur is folly."

Where personnel interactions have changed, the change is largely a function of convenience, e.g. chats in the elevator or greetings in the break-room. Regardless if the building plan is promoting increases in formal collaborations, theses casual encounters are worthwhile in their own right. Casual encounters can be the seeds of a relationship and a future boundary-spanning individual.

Conclusions and Recommendations

Specific comments in the survey, as discussed in the preceding section, reveal the ERB is indeed acting as a small scale example of a boundary object to transfer knowledge through the availability of brochures, literature, and posters. Through these devices, the ERB acts to promote awareness of activities and research occurring in the

building. Once again, we use the analogy of articles within a journal published by a boundary organization: the ERB is the analog to the journal and the specific objects within the ERB are analogous to the enclosed journal articles.

The ERB shines as an example of a boundary object providing a "basis for negotiation," as discussed by Sapsed and Salter (2004). The ERB provides a physical, literal basis for negotiation in the form of common space, common meeting rooms, and, for some, commonly-shared thought patterns, ideals, and values among its inhabitants. The boundary organization, the university, further promotes the boundary object role for the building through the organizational statements, posters, and exhibits throughout the building. Thus the organization is using the building to bridge boundaries between the departments that inhabit it, fulfilling the organizational goal of promoting the research structure and proliferation of the university. Such action and reaction within the ERB and the university fulfills the objective of the boundary object in promoting "organizational goals" (Carlile, 2002). Survey comments indicate that the ERB is having some success as mediating between the two groups and raising awareness of the possibilities for productive interdisciplinary research. Thus, these results demonstrate that the ERB is helping its inhabitants learn about their "similarities, differences, and interdependencies" (Carlile, 2002).

Nevertheless, there is still evidence of the boundaries between groups and the failure of the ERB to be a total success as a boundary object. This failure is evident in survey responses which indicated that many scientists don't know much about the policy group: "I don't know who they are or what they do. It isn't obvious how they can really benefit any of my projects, but I have to confess that this is largely ignorance. " Policy

faculty said “I see the activity in the labs but don’t understand what they are doing.” Thus the ERB may be transferring knowledge but failing to translate it.

We fully recognize that our sample size is extremely limited, as this survey represents a small percentage of university scientists and public policy personnel. Nevertheless, the prevalence of responses commenting on the role of public opinion, democratic processes, and citizen scientists allows us to draw some conclusions and suggestions relevant on a broader scale.

First, public opinion is an essential input for land use decisions in our democratic system. If public opinion is to have a major or even overriding influence on decisions about management of natural resourced and public lands, then public education is essential. As one respondent noted, public policies for land use and resource use should be founded on “knowledgeable input from our citizens, though we must somehow figure out the complexity of what knowledgeable means.” Some people within Boise State University and many other universities do help the university act as boundary organizations for this particular barrier and adopt the responsibility to educate the public and to foster “knowledgeable” citizens

Universities also directly educate future scientists and future decision makers as well as the public. At least 5 different responses in this case study indicated the importance of having citizens who are concurrently educated. For example, one response stated that people are needed “in decision making and public policy that have a scientific background” and that “development of interdisciplinary programs across science and policy would be very beneficial.” Scientists and decision makers thusly educated would understand the processes, the cultures, and the roles that lie on both sides of the

boundary. They would be able to interpret and convey knowledge across the boundary in either direction and act as boundary-spanners. In any case, before such a person can choose to rise up and stand in the gap, he must have the knowledge base that affords him the opportunity to do so.

The public university, acting as a boundary organization, can build those foundations within the student body by fostering interactions between them. These efforts to promote student education and interactions are likely to have more impact than similar attempts among faculty, for several reasons. In general, students are at a more social time in their lives. They experience fewer time constraints from family and other outside commitments. Academically, they are more flexible and more likely to attempt new thought processes or explore new points of views. Students are not yet set on a career path are more likely to act outside the cultural boundaries of their discipline. Thus it is likely that boundary organization efforts to promote collaborations among student may give rise to a boundary-spanning individual or at the least may provide a solid basis for relationships between scientists and decision makers.

This study allows universities who strive to act as boundary organization and promote inter-disciplinary cross-pollination the opportunity to understand some of the constraints and difficulties of their roles and of the roles of their boundary objects. In this case study, the ERB acted as a boundary object within the university setting to transfer knowledge and mediate personal interactions. These interactions are the foundation for future relationships and the formation of boundary-spanning individuals. Thus we can see the critical ties and feedback between boundary organizations, boundary objects, and boundary-spanning individuals.

The choice for scientists to develop themselves as a boundary-spanning individual is a personal one. On the other hand, by their very nature decisions for public lands and resource management require an understanding of science, scientific processes, and assessments of uncertainty. With that in mind, we recommend that public universities, in their role as boundary organizations, set up a Certificate in Science for Management program targeted towards decision makers and especially towards those who are active in public lands and resource management. Although some managers do have scientific backgrounds, this certificate would provide a foundation for those who do not. Young career decision makers involved in public lands or resource management could complete this certificate as part of their professional development. Recommended course work would include natural sciences, a course in statistics, and a course in scientific ethics. Such a program would enhance boundary-spanning outside the university setting by give young decision makers a solid foundation for the science involved in their decisions.

Final Remarks

This paper began with defining science. Our definition of science is narrow enough to maintain the rigor of scientific results but broad enough to include data analysis techniques made possible by today's technology. This science also embraces and delineates uncertainty in results. Such a definition promotes public credibility and legitimacy in the scientific component of policy decisions for lands management and resource use. This credibility and legitimacy encourages decision makers to consider the science slice of the decision-making pie. Thus decision makers can promote scientifically-based decisions for sustainable management of resource and lands.

In regards to boundary organization theory, this case study presents a potential example of a boundary object that outside the realm of traditional boundary objects by proposing that a building can act effectively as a boundary object. We recognize that the study is limited in scope, but hope that the results provide a basis for growth of the theory underlying boundary organizations and boundary objects as well as continued discussion on the role of the public university as a boundary organization. Furthermore, these results have some extension outside the university setting – real-world scientists and decision makers face some of the same barriers as the personnel who participated in this study, including time and geography. With that in mind, future work will investigate potential non-traditional boundary objects outside the university setting.

APPENDIX REFERENCES

Affolderbach. J., R.A. Clapp, and R. Hayter, 2012, Environmental Bargaining and Boundary Organizations: Remapping British Columbia's Great Bear Rainforest: *Annals of the Association of American Geographers*, **102**, 1391-1408.

Agrawla, S., K. Broad, and D.H. Guston, 2001, Integrating Climate Forecasts and Societal Decision Making: Challenges to an Emergent Boundary Organization: *Science, Technology, & Human Values,* **26**, 545-477.

Babcock, E.L. and J. Silvertooth, 2012, Soil Testing and Plant Analysis Relationships for Irrigated Chile Production: *Communications in Soil Science and Plant Analysis* **43**, 2651-2668.

Benjamin, A.C., 1949, On Defining "Science": *The Scientific Monthly*, **68**, 192-198.

Boumil, M.M., and H. Berman, 2010, Transparency in research and its effect on the perception of research integrity: *JONA's Healthcare Law, Ethics, and Regulation,* **12**, 64-68.

Brownson, R.S., C. Royer, R.E. Ewing, and T.D. McBride, 2006, Researchers and Policymakers: Travelers in Parallel Universes: *American Journal of Preventative Medicine*, **30**, 164-172.

Carlile, P.R., 2002 A Pragmatic View of Knowledge and Boundaries: Boundary Object in New Product Development: *Organization Science,* **13**, 442-455.

Carls, M.G., S.D. Rise, and J.E. Hose, 1999 Sensitivity of fish embryos to weather crude oil: Part I. Low-level exposure during incubation causes malformations, genetic damage, and mortality in larval pacific herring (*Slupea Pallasi*): *Environmental Toxicology and Chemistry,* **18**, 481-493.

Carr, A. and R. Wilkinson, 2005, Beyond Participation: Boundary Organizations as a New Space for Farmers and Scientists to Interact: *Society and Natural Resources,* **18**, 255-265.

Cash, D.W., 2001, In order to Aid in Diffusing Useful and Practical Information: Agricultural Extension and Boundary Organizations: *Science, Technology, & Human Values*, **26**, 431-453.

Cash, D., W. Clark, W. Alcock, N. Dickso, W. Eckley, and J. Jäger, 2002, Salience, Credibility, Legitimacy and Boundaries: Linking Research, Assessment and

Decision Making: John F. Kennedy School of Government Faculty Research Working Papers.

Coates, W., 2005, Tree species selection for a mine tailing bioremediation project in Peru: *Biomass and Bioenergy,* **28**, 418-423.

Cutts, B.B., D.D. White, and A.P. Kinzig, 2011, Participatory geographic information systems for the co-production of science and policy in an emerging boundary organization: *Environmental Science & Policy,* **14**, 977-985.

Eden, S., 2011, Lessons on the generation of usable science from an assessment of support practices: *Environmental Science & Policy*, **14**, 11-19.

Franks, J., 2010, Boundary organizations for sustainable land management: The example of Dutch Environmental Co-operatives: *Ecological Economics*, **70**, 283-295.

Freemuth, J., 2011, Thoughts on the role of science in making public policy, *in* S.T. Knick and J.W. Connelly, eds., Ecology and Conservation of a Landscape Species and Its Habitats, University of California Press for Cooper Ornithological Society, 2-13.

Gieryn, T.F., 1995, Boundaries of science, *in* S. Jasanoff, G.E. Markle, J.C. Petersen, and T. Pinch, eds., Handbook of science and technology studies, Thousand Oaks, CA: Sage, 393–443.

Goldman, M., 1983, The Demon in the Ether: The Story of James Clerk Maxwell, Edinburgh: Harris Press.

Goldstein, B.D., 2012, John Snow, the Broad Street pump and the precautionary principle: *Environmental Development*, **1**, 3-9.

Gottfried, K. and K.G. Wilson, 1997, Science as a cultural construct: *Nature*, **386**, 545-547.

Guston, D.H., 1999, Stabilizing the boundary between US politics and science: The role of the Office of Technology Transfer as a boundary organization: *Social Studies of Science*, **29**, 87–112.

Guston, D.H., 2001, Boundary organizations in environmental policy and science: An Introduction: *Science Technology, & Human Values*, **26**, 299–408.

Henderson, K., 1991, Flexible Sketches and Inflexible Data Bases: Visual Communication, Conscription Devices, and Boundary Object in Design Engineering: *Science, Technology, & Human Values*, **12**, 448-473.

Intergovernment Panel on Climate Change (IPCC), 2007, Climate change 2007-mitigation of climate change: Contribution of Working Group III to the Fourth

Assessment Report of the IPAA. Online at http://www.ipcc.ch/pgf/assessent-report/ar4/syr/ar4_syr.pdf.

Jacobs, K., G. Garfin, and M. Lenart, 2005, More than just Talk: Connecting Science and Decision Making: *Environment: Science and Policy for Sustainable Development,* **49**, 6-21.

Kell, D.B., and S.G. Oliver, 2004, Here is the evidence, now what is the hypothesis? The complementary roles of inductive and hypothesis-driven science in the post-genomic era: *Bioessays,* **26**, 99-105.

Krull, K., and B. Kulikov, 2006, Isaac Newton: New York: Viking Press.

Lackey, R.T., 2007, Science, Scientists, and Policy Advocacy: *Conservation Biology,* **21**, 12-17.

Lucarini, V., 2002, Towards a definition of climate science: *International Journal of Environment and Pollution*, **18**, 413-422.

Michaels, S., 2009, Matching knowledge brokering strategies to environmental policy problems and settings: *Environmental Science & Policy*, **12**, 994-1011.

Miller, C., 2001, Hybrid Management: Boundary Organizations, Science Policy, and Environmental Governance in the Climate Regime: *Science, Technology, & Human Values*, **26**, 478-500.

Nature Methods, editorial, 2009, Defining the scientific method: *Nature Methods,* **6**, 237.

O'Mahoney, S. and B.A. Bechky, 2008, Boundary Organizations: Enabling Collaboration among Unexpected Allies: *Administrative Science Quarterly*, **53**, 422-459.

Palmer, T., 2008, Edward Norton Lorenz: *Physics Today*, **61**, 81-82.

Parker, J. and B. Crona, 2012, On being all things to all people: Boundary organizations and the role of the contemporary research university: *Social Studies of Science*, **42**, 262-287.

Pietri, D., S. McAfee, A. Mace, E. Knight, L. Roger, and E. Chornesky, 2011, Using Science to Inform Controversial Issues: A Case Study from the California Ocean Science Trust: *Coastal Management,* **39**, 296-316.

Rosner, B, 2011, Fundamentals of Biostatistics, 7th Ed: Harvard University Press.

Safford, T.G. and K.C. Norman, 2011, Water water everywhere, but not enough for salmon? Organizing Integrated water and fisheries management in Puget Sound: *Journal of Environmental Management*, **92**, 838-847.

Sapsed, J. and S.A. Salter, 2004, Postcards from the Edge: Local Communities, Global Programs and Boundary Objects: *Organization Studies*, **25**, 1515-1534.

SAHRA, 2001, Annual report: On-line at http://www.sahra.arizona.edu/publications.

Smith, W. and S. Kelly, 2003, Science, technical expertise, and the human environment: *Progress in Planning*, **60**, 321-394.

Star, S.L. and J.R. Griesemer, 1989, Translations and Boundary Objects: Amateurs and Professional in Berkeley's Museum of Vertebrate Zoology: *Institutional Ecology*, **19**, 387-420.

Tuunainen, J., 2005, When Disciplinary Worlds Collide: The Organizational Ecology of Disciplines in a University Department: *Symbolic Interaction*, **28**, 205-228.

van Dijk, E.M., 2011, Portraying Real Science in Science Communication: *Science Education*, **95**, 1086-1100.

White, D.D., E.A. Corley, and M.S. White, 2008, Water Managers' Perceptions of the Science-Policy Interface in Phoenix, Arizona: Implications for an Emerging Boundary Organization: *Society & Natural Resources: An International Journal*, **21**, 230-243.

Wong, S.L. and D. Hodson, 2010, More from the Horses's Mouth: What scientists say about science as a social practice: *International Journal of Science Education.* **32**, 1431-1462.

Zneiss, R. and P. Groenewegen, 2009, Engaging Boundary Object in OMS and STS? Exploring the Subtleties of Layered Engagement: *Organization*, **16**, 81-100.